Fermi surface properties of binary and ternary superconductors

Swetarekha Ram

A Thesis Submitted to
Indian Institute of Technology Hyderabad
In Partial Fulfillment of the Requirements for
The Degree of Ph.D

भारतीय प्रौद्योगिकी संस्थान हैदराबाद
Indian Institute of Technology Hyderabad

Department of Physics

February 2014

Declaration

I declare that this written submission represents my ideas in my own words, and where ideas or words of others have been included, I have adequately cited and referenced the original sources. I also declare that I have adhered to all principles of academic honesty and integrity and have not misrepresented or fabricated or falsified any idea/data/fact/source in my submission. I understand that any violation of the above will be a cause for disciplinary action by the Institute and can also evoke penal action from the sources that have thus not been properly cited, or from whom proper permission has not been taken when needed.

SRa 3/2/2014

(Signature)

(Swetarekha Ram)
Ph10p003
(Roll No.)

Certificate

I hereby certify that the matter embodied in this thesis entitled "**Fermi surface properties of binary and ternary superconductors**" has been carried out by **Swetarekha Ram** at the Department of Physics, Indian Institute of Technology Hyderabad, India under my supervision and that it has not been submitted elsewhere for the award of any degree or diploma.

SRay 3/2/2014

(Signature)

(Swetarekha Ram)
Ph10p003
(Roll No.)

3/02/2014

(Signature)

(Dr. V. Kanchana)
Adviser

DR. V. KANCHANA
Assistant Professor
Department of Physics
IIT HYDERABAD-502205

Approval Sheet

This Thesis entitled "Fermi surface properties of binary and ternary superconductors" by Swetarekha Ram is approved for the degree of Ph.D from IIT Hyderabad

R. Ranganathan 5/5/14

Prof. R. Ranganathan
Saha Institute of Nuclear Physics
Examiner

Vandana Sharma 05/05/2014

Dr. Vandana Sharma
IIT Hyderabad
Examiner

5/5/2014

Dr. V. Kanchana
IIT Hyderabad
Adviser

Bsmallik 05/05/2014

Dr. Bhabani Shankar Mallik
IIT Hyderabad
Chairman

Acknowledgements

Completion of this doctoral dissertation was possible with the support of several people. First, I give thanks to God for protection and granting me the wisdom, ability to do work and enabling me to its completion. I would like to thank all those people who made this thesis possible. At the end of my thesis, it is a pleasant task to express my thanks to all those who contributed in many ways to the success of this study and made it an unforgettable experience for me.

I owe my deepest gratitude to my advisor, **Dr. V. Kanchana**, for her guidance, continuous support, motivation, enthusiasm, caring, patience, and providing me with an excellent atmosphere for doing research. This work would not have been possible without her guidance, support and encouragement. This thesis has been kept on track and been seen through to completion with the support and encouragement. Her guidance helped me in all the time of research and writing of this thesis. This feat was possible only because of the unconditional support provided by her. Madam has always made herself available to clarify my doubts despite her work and I consider it as a great opportunity to do my doctoral programme under her guidance and to learn from her research expertise. And during the most difficult times when writing this thesis, she gave me the moral support. I can only say a proper thanks to her through my future work.

Besides my advisor, I would like to express my thanks to **Dr. G. Vaitheeswaran**, ACRHEM, University of Hyderabad, for his valuable advice, constructive criticism and his extensive discussions around my work at all the time. I would like to thank him, who let me experience the research in the practical issues beyond the textbooks. I have received consistent encouragement from him throughout the research work. It is my pleasure to acknowledge **Prof. M. C. Valsakumar**, SEST, University of Hyderabad for all his fruitful suggestion and discussions which I had with him for a part of my work.

My sincere thanks must also go to my doctoral committee members: **Dr. Saket Asthana** (Department of Physics, IIT Hyderabad) and **Dr. Pinaki Prasad Bhattacharjee** (Department of Materials Science and Engineering, IIT Hyderabad) for their encouragement, insightful comments.

I take this opportunity to sincerely acknowledge **Dr. Anjan Kumar Giri**, Head, Department of Physics, for providing necessary infrastructure and resources to accomplish my research work. I gratefully acknowledge all the faculty members of the Department of Physics. My sincere acknowledge goes to **Prof. U. B. Desai**, the Director of Indian Institute of Technology Hyderabad

for providing best environment for doing research. I am also thankful to **Prof. F. A. Khan** for providing all academic needs.

I would like to thank the Ministry of Human Resource and Development, Government of India, New Delhi, through Indian institute of Technology Hyderabad for providing financial assistance in the form of Research Fellowship which supported me to perform my work comfortably.

I would also like to extend huge, warm thanks to my groupmates, **Vijay Kumar Gudelli**, **Gummula Shwetha** and **P. V. Sreenivasa Reddy** for their continuous support and discussion during the time of my research need. This is my pleasure to acknowledge **K. Ramesh Babu**, **S. Appalakondaiah** and **N. Yedu Kondalu** for their timely help in my research work. I would also like to thank the research scholars of the Department of Physics. I am indebted to some of my friends **N. Vandana**, **Anupama Bhol**, and others who made my stay in the hostel very pleasant. I would like to extend my thanks to the Physics lab staff, academic, administration, high performance computational staffs and library staffs for their constant support in my academic and non-academic works.

I am grateful to my school and college teachers, **Prof. Basudeb Sahu, Dr. Susmita Kar, Dr. B. Rath, Dr. Indrajit Naik** and **Dr. Pravanjan Mallick** who laid seeds of enthusiasm and passion in my pursuit of knowledge.

I would like to thank my family, especially my mother and father for always believing in me, for their continuous love and their support in my decisions, without whom I could not have made it here. I can't imagine my current position without the love and support from my family. I thank my parents, **Mr. Pramod Kumar Ram** and **Mrs. Kiran Devi**, for striving hard to provide a good education for me. I always fall short of words and felt impossible to describe their support in words. If I have to mention one thing about them, among many, then I would proudly mention that my parents are very simple and they taught me how to lead a simple life. Finally, I would like to thank my husband, **Rahul Kumar Ram**. He was always there cheering me up and stood by me during the last days of Ph. D. work.

Swetarekha Ram

DEDICATION

To

MY BELOVED PARENTS

And

Supervisor Dr. V. KANCHANA

Abstract

Density functional theory (DFT) has been widely used in condensed matter physics to explore different material properties and is the most successful theory in electronic structure calculations. In the present thesis, DFT has been used to compute the Fermi surface (FS) topology under compression in lanthanum and yttrium based binary and ternary Cu_3Au-type superconducting compounds and some lanthanum based filled skutterudites. In addition, we try to correlate the variation of the density of states at the Fermi level, $N(E_F)$, elastic softening, variation of superconducting transition temperature, T_c, under compression with the FS topology change.

In the present work the electronic structure, Fermi surface topology, mechanical and superconducting properties of AX_3 (A = La, Y; X = Sn, Pb, In, Tl), A_3X (A= La; X=In, Tl, Sn), La_3InZ (Z = N, O) and $LaRu_4X_{12}$ (X = P, As, Sb) compounds are studied under compression. In AX_3 series, the Fermi surface topology change is observed within the complex sheet under compression except in YSn_3 and YPb_3. The reason for the isoelectronic and isostructural $LaSn_3$ and YSn_3 to behave differently is deliberated in terms of the spin-orbit effect and the La '$4f$' hybridization due to which we find an extra hole pocket within the complicated FS sheet in $LaSn_3$ which is absent in YSn_3. In addition, an extra electron pocket exist in YSn_3 at ambient and the same is seen to appear under pressure in $LaSn_3$. On the other hand the C_{44} softening under pressure in $LaPb_3$ differentiate the same from YPb_3 though the electronic structure at the vicinity of the Fermi level is found to be similar with the inclusion of the spin-orbit coupling, at ambient conditions.

A comparative study of LaX_3 with La_3X revealed the different La 'd' orbital splitting and is attributed to the local tetragonal and octahedral site symmetry of La in La_3X and LaX_3, respectively in the above two cases. In addition to this, a FS topology change is observed in all FS sheets of La_3X series in contrast to LaX_3 series where we noticed the FS topology to change only in complicated sheet. More interestingly the positive and negative pressure dependence of T_c in La_3X and LaX_3, respectively is analyzed in detail along with the phonon dispersion relation.

Further the electronic, Fermi surface, mechanical and superconducting properties are explored for La_3InZ-type compounds, which is formed by adding Z (Z = N, O) atom in the body center of La_3In without changing the crystal structure of the host compound. We find the suppression of T_c with the inclusion of Z atom in La_3In. More interestingly initial decrease of T_c under pressure followed by an increase with the increase in pressure in the case of La_3InO is seen, which is quite different

from the T_c trend observed in La_3In and is attributed to the appearance of the new hole surface and an extra electron sheet under compression (pressure $= 15\ GPa$) in La_3InO.

From the above findings, it is imperative that FS topology change under pressure induce a non-monotonic variation of T_c, and we have further extended our study to analyze La based filled skutterudites and find a FS topology change in As and Sb containing compounds which might further lead to the same anomaly in T_c, as explained in the above mentioned compounds.

Overall the present thesis gives an overview of the trend in the variation of T_c which can be related with the Fermi surface topology change and it has been clearly verified for quite a few compounds. It further provokes us to state that one can look for a non-monotonic T_c variation under pressure in superconductors, where the FS topology change is observed.

Contents

Nomenclature

List of symbols (units)

T_c	Superconducting transition Temperature (K)
k_B	Boltzman's constant (J K^{-1})
h	Planck's constant (J. s)
$\hbar$	Reduced Planck's constant (J. s)
V_{eff}	Interaction between the electrons mediated by the electron-phonon coupling
$\mathrm{F}(\omega)$	Phonon density of states
$\langle I^2 \rangle$	Square of the electron-ion interaction
M	Atomic mass
$N(E_F)$	Density of states at Fermi level (states/eV/f.u.)
E_F	Fermi level
V_{ext}	External nuclear potential
$\hat{H}$	Hamiltonian
m_i	Electronic mass
Z_I	Nuclear charges
M_I	Nuclear mass
T_e	Kinetic energy of the electron
V_{ee}	Potential energy of the electron
T_n	Kinetic energy of the nucleus
V_{en}	Potential energy of the electron and nucleus
V_{nn}	Potential energy of the nucleus
E_0	Ground state energy
E_{xc}	Exchange-correlation energy
V_{ks}	Kohn-Sham potential
j_l	Spherical Bessel functions
$n(r)$	Electronic density as a function of position
R_{MT}	Muffin-tin radius
K_{Max}	Plane wave cut-off
T_N	Antiferromagnetic temperature

G_{max}	Charge-density Fourier expansion (a.u.$^{-1}$)
C_{11}, C_{12} and C_{44}	Elastic constants (GPa)
G_H	Hill's shear modulus (GPa)
G_R	Reuss shear modulus (GPa)
G_v	Voigt shear modulus (GPa)
E	Young's modulus (GPa)
B	Bulk modulus (GPa)
C_p	Cauchy pressure (GPa)
A	Anisotropy factor
v_l	Longitudinal sound velocity (km/s)
v_t	Transverse sound velocity (km/s)
v_m	Mean sound velocity (km/s)
Θ_D	Debye temperature (K)
N_A	Avogadro's number

Greek Letters

ω	Phonon frequency
ω_c	Cutoff phonon frequency
λ_{ep}	Electron-phonon coupling constant
ω_{ln}	Logarithmically averaged phonon frequency
μ^*	Coulomb pseudo potential
η	Hopfield parameter
$\alpha(\omega)$	strength of an average electron-phonon interaction
$\langle\omega^2\rangle$	average of the square of the phonon frequency
ψ	wave function
σ	Poisson's ratio
ρ	Mass density

Subscripts

i, j	Number of electron index
I, J	Number of nucleus index
e	Electron
n	Nucleus
0	Ambient condition

Abbreviations

FS	Fermi surface
CDW	Charge-density-wave
SDW	Spin-density wave
SQUID	Superconducting quantum interference device
MRI	Magnetic resonance imaging
DFT	Density-functional theory
LDA	Local density approximation
GGA	Genelarized gradient approximation
LAPW	Linearized augmented planewave
FP-LAPW	Full-potential linearized augmented planewave
SOC	Spin-orbit coupling
BZ	Brillouin zone
DOS	Density of states
HF	Hartree-Fock
AE	All electron
ps	Pseudo function
dHvA	de Haas van Alphen

Chapter 1

Introduction

One of the most important characteristics of a metal is its Fermi surface (FS), the surface of constant energy in k-space. During 1950's it was realised first that, special efforts are needed to reveal anything directly from the geometry of the energy surface. I. M. Lifshitz and Onsagar [1, 2] first described the connection between the magnetic oscillation and the Fermi surface on the basis of the electron dynamics and the quantum mechanical concepts. The knowledge about the FS of a metal is an important tool to understand various properties of a metallic material such as structural transition, elastic, magnetic properties etc. First principles band structure calculations serve as a good source to analyze these above properties which are related to the FS topology. The geometrical characteristics of Fermi surface, such as the shape, curvature, and cross-sectional area, are related to the physical properties of metals. For example, the velocity of electron on the Fermi surface can be estimated from the knowledge of the effective mass, which is calculated from the cyclotron resonance frequency.

Importance of FS topology in different class of material: The Fermi surface nesting can help to determine the charge-density-wave (CDW) and spin-density-wave (SDW) instabilities. A Fermi surface instability which is associated with the spin-density wave has been reported in the case of superconducting material UPt_3 [3]. Fermi surface topology change is observed under pressure in certain cobalt based Heusler alloys Co_2XY (X = Cr, Mn, Fe; Y = Al, Ga), where a transition from half-metallic to metallic or vice versa [4, 5] is present. Apart from this the most interesting property is the co-existence of anti-ferromagnetism and the superconductivity in certain materials such as $LuNi_2B_2C$ [6] and $HoNi_2B_2C$ [7], which lead to the Fermi surface nesting. A drastic FS topology change is observed due to the change in '$4f$' electron character of Ce (from localized to itinerant) in $CeRhIn_5$ at a pressure around 2.35 GPa, where the superconducting transition temperature was also noticed to be maximum [8]. A Fermi surface topology change occurs in the case of UGe_2 [9, 10] when the weakly polarized phase is changed into strongly polarized phase with increasing magnetic field. More interestingly, the lattice collapse was observed in hexagonal metallic compound YCo_5 under hydrostatic pressure of 19 GPa, driven by magnetic interactions where the Fermi surface topology also changes and can be characterized as a first-order Lifshitz transition [11]. The anomaly in superconducting transition temperature (T_c) under pressure was also observed in $HgBa_2CaCu_2O_{6+\delta}$ and was suspected to be driven by the FS topology change [12]. The dramatic change in topology of the FS of $CaFe_2P_2$ suggests, a state with reduced (c/a) ratio, and the Fermi surface sheets are unlikely to be nested [13]. Similarly the phase transition in some iron pnictide superconductors was attributed to the nesting feature rather than spin frustration [14]. The anomaly in resistivity at pressure around 1 GPa for $Ba_{1-x}K_xFe_2As_2$ could be mainly due to the reconstruction of the Fermi surface [15]. Most of the superconducting elements show a monotonous decrease of T_c under pressure, but with the exception of thallium and rhenium, where people have observed more complex pressure dependence of T_c without any structural transition and suspected the same to be due to the modification of the electronic structure [16, 17, 18]. On further analysis of these elements it was proposed that the observed anomaly is due to the FS topology change [19, 20]. In addition to this, alloying rhenium with other metals like Os, W, Mo also has an effect on the pressure dependence of T_c and this anomaly again is linked to the FS topology change [18, 21]. The anomaly in T_c under pressure was reported in the case of Nb, where the authors suspected the same to be due to the electronic topological transition [22]. The increase of T_c under pressure in V was explained by Vaitheeswaran et. al [23], where the authors attributed the positive pressure dependence of T_c to $s \rightarrow d$ electron transfer and later some other group reported the mechanical instability and C_{44} softening in vanadium and niobium to be respectively due to the nesting feature of FS [24]. Recently the FS topology change under pressure in iron chalcogenides and pnictides is correlated with T_c, where the authors find FS nesting under pressure and suspected the T_c to increase under pressure [25]. In this present work, we have also shown the importance of the FS topology in Cu_3Au type compounds and in some skutterudite superconducting materials and show the role of FS topology on electronic and the superconducting properties of these materials at ambient as well as under compression.

Experimentally many techniques have been developed to study the FS topology such as angle-resolved photoemision spectroscopy [26, 27, 28], the de-Haas van Alphen effect [29], the shubnikov-de Haas effect [30, 31], cyclotron resonance and periodic orbit resonance etc. Bismuth is the first metal for which FS was determined experimentally. In the case of low dimensional materials only surface sensitive technique, such as angle-resolved photo-emission, which is the most powerful technique to probe the Fermi surface of a solid can be used to analyze the Fermi surface. All the above facts lead us to study the Fermi surface of solids theoretically in this present work. The interplay between superconductivity and Fermi surface is a frequent theme in condensed matter physics.

1.1 History of superconductivity

At critical temperature (T_c), the total disappearance of the electrical resistivity leads to the transition of a normal metal to a superconducting state [32, 33] and the superconductors are the materials which allow the conduction of electricity with absolutely zero resistance. Soon after the discovery of superconductivity in mercury in 1911 [32], a broad and significant research efforts were aimed to identify superconducting materials. The microscopic theory of superconductivity was explained by John Bardeen, Leon Cooper and Robert Schrieffer in 1957 [34], the first widely-accepted theory for understanding superconductivity (BCS theory). According to the BCS theory the electrons form Cooper pairs due to the interaction with the crystal lattice at low temperature. Alternatively we can say that Cooper pair is nothing but an attraction between two electrons with opposite spin and momentum, mediated by the lattice which creates a 'bound' state of the two electrons and the ground state of a material is unstable with respect to this pairs of 'bound' electrons. The formation of Cooper pairs lead to the formation of the energy gap, indicating no single electron can occupy the state near the Fermi surface. Cooper pairs are produced at low temperature and this is the only interaction that exist in the superconductor resulting in an energy difference from the normal metal. In 1953, the zero resistance was identified for the first time in the multi-metal compound based on niobium [35]. The first 20 years were restricted in finding the superconducting materials with niobium like NbN, Nb_3Sn and Nb_3Ge [35, 36]. D. Josephson in 1962 predicted the flow of electric current between two superconducting materials, even when they are separated by a non-superconductor or insulator and is known as "Josephson effect", which has been used in electronic devices such as the SQUID (superconducting quantum interference device). Afterwards research further evolved with focus on the intermetallic compounds and at the beginning of the 21^{st} century the discovery of the superconductivity with multiple superconducting gap in MgB_2 lead to special interest in the intermetallic superconductors [37].

Figure 1.1: Periodic table for superconducting elements. The purple color in this periodic table is for the elements that are superconductors under normal atmospheric pressure conditions and orange color is for those that are superconductors when subjected to high pressure. Under normal pressure conditions, 29 elements are superconductors and under pressure 23 elements behave as a superconductor. This figure is adapted from the Ref. [42]

Finding new superconducting materials and understanding the origin of the superconductivity is still one of the most interesting and the challenging task in modern physics and chemistry. Alloys and intermetallic compounds are the most important man made materials and remain the subject of interest for physicist, chemists and material scientist [38, 39, 40]. For the past several years it was noticed that intermetallic compounds mostly have high strength, good magnetic nature and some are superconductors [41] (references found therein). Applications of superconductors have emerged in diverse areas of science and technology including transportation (a superconducting magnetic levitation (maglev) train), medical care (magnetic resonance imaging (MRI) equipment used in hospital), etc. Superconductors also find important applications in electronics, including resonators, magnetometers (SQUID), voltage storages, arithmetic circuits, and memory circuits. SQUID in particular is capable of detecting externally weak magnetic fields and, thus, is used for studying magnetic properties of materials and for observing weak magnetic fields emitted by hair or brain. At ambient pressure there are few known superconducting elements in the periodic table, and few elements behave as superconductors under pressure as shown in periodic table in Fig. 1.1.

1.2 Pressure effect on superconductivity

After the discovery of superconductivity by Kamerlingh Onnes [32], the same group carried out the first high pressure experiments on superconductor [33]. In 1969 the superconductivity of Li was proposed by Allen and Cohen [43], but no such superconductivity was evident at temperature below 4 mK [44]. However the superconductivity in Li was predicted by Christensen et. al [45] under high pressure with transition temperature of 80 K. The average phonon frequency and the electronic density of states at the Fermi level ($N(E_F)$) are the fundamental parameters to estimate the T_c of the material under pressure. So according to the BCS theory, T_c can be expressed as

$$k_B T_c = 1.13\hbar\omega_c exp(-1/\lambda_{ep}) \tag{1.1}$$

where k_B is the Boltzman's constant and $\hbar$ is the Planck's constant, ω_c is cutoff frequency, λ_{ep} = $N(E_F)\mathrm{V}_{eff}$, is the electron-phonon coupling constant and V_{eff} is the interaction between the electrons mediated by the electron-phonon coupling.

In the extension of the BCS theory, Eliashberg developed a theory in the limit of strong-coupling superconductivity [46]. McMillan [47] derived an equation by considering the Eliashberg theory to calculate the T_c of the material which was later modified slightly by Allen-Dynes [48] as following.

$$T_c = \frac{\omega_{ln}}{1.2} \exp\left(-\frac{1.04(1+\lambda_{ep})}{\lambda_{ep} - \mu^*(1+0.62\lambda_{ep})}\right) \tag{1.2}$$

Here ω_{ln} is the logarithmically averaged phonon frequency and dimensionless μ^* is the Coulomb pseudo potential. Calculations of μ^* is computationally demanding and are not yet under theoretical control.

The dimensionless electron-phonon coupling constant, λ_{ep} used in the theory of the superconductivity is given by [47]

$$\lambda_{ep} = 2\int \frac{d\omega\alpha^2(\omega)F(\omega)}{\omega} = \frac{N(E_F)\langle I^2\rangle}{M\langle\omega^2\rangle} \tag{1.3}$$

$\alpha(\omega)$ and $\mathrm{F}(\omega)$ are the strength of an average electron-phonon interaction and the phonon density of states, respectively. $\langle I^2\rangle$ is the mean of the square of the electron-ion interaction, M is the atomic mass and $\langle\omega^2\rangle$ is the average of the square of the phonon frequency. The above equation contains two parts, the numerator representing the electronic part and the denominator represents the phononic part. The numerator $N(E_F)$ $\langle I^2\rangle$ is the Hopfield parameter, η, an atomic property and can be calculated directly from band-structure theory. The calculations of λ_{ep} is generally required to compute the phonon frequencies.

From equation (1.2) and (1.3), it is quite clear that the pressure dependence of T_c is very complex and depends upon different parameters of the electronic and phononic part. Generally under pressure the phonon frequency is expected to harden which implies that T_c as per the equation (1.2) may increase, but at the same time from equation (1.3), it is evident that λ_{ep} would decrease under pressure as $\langle\omega^2\rangle$ increases and $N(E_F)$ decreases for most of the materials, ultimately leading to the decrease of T_c under pressure. The Allen-Dynes formula as in equation (1.2) is quite successful in determining the T_c of various superconducting materials.

It is very well known that intermetallic compounds possess wide range of properties and need to be explored from various directions. Our present interest focus especially on the Fermi surface topology of the superconducting materials and to predict the trend of T_c at ambient as well as under compression. In this thesis we present the electronic, FS topology, elastic, mechanical and superconducting properties of different series of compounds such as AX_3 (A = La, Y; X = In, Tl, Sn, Pb), La_3X (X = In, Tl, Sn), La_3InZ (Z = N, O) and $LaRu_4X_{12}$ (X = P, As, Sb).

1.3 Overview of the Cu_3Au-type and skutterudite compounds

The intermetallic compounds which crystallize in the Cu_3Au type structure are quite interesting because of their wide range of properties such as superconductivity [49], spin-fluctuation [50], antiferomagnetic phase transition [51], heavy fermion behaviour [52] etc. The lanthanum, yttrium and some of the scandium based intermetallic compounds have served as reference material which is helpful to study the various properties of the rare-earth compounds. For example, the de Haas van Alphen effect (dHvA) study showed the FS topology of magnetic $GaIn_3$ to be similar with non magnetic $LaIn_3$ and the effective mass was reported close to $LaSn_3$ [53]. Again the dHvA study on $PrIn_3$ show a branch which is inert to the applied magnetic field, to be the same as in $LaIn_3$ and is agreeable with the band structure calculation [54]. A comparative study of FS topology on $CeIn_3$ and $LaIn_3$ was performed by Betsuyaku et. al [55] and the pressure study on FS topology showed the existence of the similar branch in both of these compounds. More interestingly it was also noticed that the electric field gradient at In site is the same in both $CeIn_3$ and $LaIn_3$ with the consideration of Ce '$4f$' electron to be itinerant [55]. The antiferro-quadrupolar ordering was found to be collapsed in $PrPb_3$ with 2.5% dilution of Pr ion with non-magnetic La ion [56]. From the comparative study of $La_xPr_{1-x}Pb_3$ (x = 0.97) and $LaPb_3$ it was found that the anomaly seen in the specific heat of $La_xPr_{1-x}Pb_3$ (x = 0.97) below 1.5 K comes from the Pr moment and not from the superconductivity of $LaPb_3$ [57]. From the above discussions, it is quite clear that the comparative study of the different compounds can serve as a better way for understanding the various properties possessed by the individual material. To explore the properties of series of isostructural Cu_3Au type of compounds, such as AX_3 (A = La, Y; X = In, Tl, Sn, Pb), A_3X (A = La; X = In, Sn) and La_3InZ (Z = N, O), we have performed a detailed theoretical calculation on electronic, Fermi surface, elastic and superconducting properties and presented a comparative study among these above mentioned group of compounds in this work. Apart from this we have also investigated a series of skutterudite compounds $LaRu_4X_{12}$ (X = P, As, Sb) and calculated the Fermi surface topology at ambient as well as under compression and try to relate the superconducting properties with Fermi surface topology change. Next we present a brief introduction about the compounds which we have studied in this work.

Among all the Cu_3Au type compounds, AX_3 (A = La, Y; In, Tl, Sn, Pb) type of compounds are of special interest [58, 59, 60, 49]. The LaX_3 alloys show non-monotonic variation in their bulk properties such as superconductivity, magnetic susceptibility, density of states, thermopower as a function of their valence electron concentration [49, 61, 62] and this behaviour has been attributed to the Brillouin zone effect, which concluded that the Fermi surface close to the boundary of the Brillouin zone would be expected to produce more pronounced effect on the variation of above properties than the Fermi surface towards the center of the Brillouin zone. It is quite interesting to note that the superconducting properties of LaX_3 compounds are mainly derived from the X-atom instead of La and these compounds behave similar to transition metals [49].

Apart from AX_3, there exist few A_3X (A = La, X = In, Tl, Sn) type of compounds [63, 64] which also crystallize in Cu_3Au type structure and possess T_c comparatively larger than the AX_3 compounds for a particular X atom [63]. A_3X compounds also show anomaly in resistivity, thermopower etc [65]. Previous experimental studies have reported these In and Tl containing La_3X type compounds to be strong coupling superconductors with T_c around 9.54 K and 8.86 K for La_3In and La_3Tl, respectively [63]. More interestingly it was found that La_3In and La_3Tl are superconductors having large temperature dependent magnetic susceptibility, and was attributed to the presence of a peak in the density of state at Fermi level [66]. Apart from this, in the case of La_3In the positive dependence of T_c under pressure was reported experimentally by Smith et. al [67]. Now it is interesting to verify the variation of superconducting properties of La_3In and the isostructural La_3X (X = Tl, Sn) compounds theoretically at ambient as well as under compression. To know more about the behaviour of these compounds it is necessary to study in detail the electronic structure, Fermi surface, elastic and superconducting properties of A_3X (A = La, X = In, Tl, Sn) compounds.

Yet another class of compounds La_3InZ (Z = C, B, N, O), also crystallize in cubic Cu_3Au type structure. Experimentally the authors have studied the superconducting nature of La_3InZ for Z = C, B, N and O and found T_c to be nearly same as that of La_3In for Z = B, O and superconductivity was not found above 2 K for La_3InC and La_3InN [68]. Ravindran et. al [69] studied the structural stability, electronic properties and superconductivity of La_3X as well as La_3XC (X= Al, Ga, In, Tl) compounds. Kirchner et. al [70] have studied experimetally as well as theoretically some R_3InN (R = Rare earth elements) type compounds and compared the bonding nature of the La_3In with La_3InN. Apart from this there are no studies available regarding the FS and the origin of the superconductivity in La_3InZ (Z = N, O) compounds at ambient as well as under compression, which is the main interest in these compounds and we discuss the effect of Z atom on the electronic structure, FS, vibrational and superconducting properties.

Filled skutterudites of $LaRu_4X_{12}$ with X = P, As, Sb are another group of superconducting materials, crystallizing in cubic structure with space group $Im\bar{3}$ (no. 204). The T_c of these compounds are reported to be 7.2, 10.3 and 2.8 K respectively [71] for X = P, As, Sb. The La-based skutterudite compounds are having special interest because of their unusual properties such as FS nesting and multiple superconducting gap in $LaRu_4P_{12}$ [72] and $LaRu_4As_{12}$ [73], respectively. Many groups have investigated and reported the nesting feature of $LaRu_4P_{12}$ with nesting vector $\vec{q}$ = (100), which is the reference material for $PrRu_4P_{12}$. The Fermi surface studies have been performed for many filled skutterudites including $LaRu_4P_{12}$ [72, 74, 75, 76], however the resistivity and specific-heat measurements in $LaRu_4P_{12}$ show no metal-insulator transition above superconducting transition temperature (T_c) as observed in $PrRu_4P_{12}$ [77]. A comparative study on the FS topology of $CeRu_4Sb_{12}$ and $LaRu_4Sb_{12}$ has been performed where the authors find the topology to be different due to the presence of strong electron correlation in the former compound. Now it is interesting to think about the FS topology and the electronic properties of $LaRu_4X_{12}$ for X = P, As, Sb at ambient as well as under compression and try to understand the correspondence between the electronic properties and the origin of superconductivity.

Table 1.1: The superconducting transition temperature, (T_c) of AX_3 compounds with A = La, Y and X = In, Tl, Sn, Pb, calculated experimentally.

Compounds	T_c (K)
$LaIn_3$ [a]	0.70
YIn_3 [a]	0.78
$LaTl_3$ [a]	1.57
YTl_3 [a]	1.52
$LaSn_3$ [a]	6.45
YSn_3 [b]	7
$LaPb_3$ [a]	4.05
YPb_3 [a]	4.72

a: Ref. [61]; b: Ref.[80]

1.4 Motivation of the work

Cu_3Au type compounds had been investigated earlier and various studies on these compounds concluded that T_c is correlated to the valence electron concentration [78, 79]. Pressure effect on FS was performed for few Cu_3Au type compounds and are correlated with different properties such as superconductivity, magnetism etc. Most of the AX_3 compounds are superconducting in nature and the nuclear magnetic resonance study show the origin of superconductivity to be mainly derived from the X-site and also expect that they can be treated as transition metal compounds, which is of particular interest and need to be explored in detail. Experimentally T_c of LaX_3 compounds was reported to be nearly same with YX_3 compounds for a particular X (X = In, Tl, Sn, Pb) atom and the values are reported in Table-1.1. Now it is interesting to compare the properties of LaX_3 and YX_3 to explore the influence of similar valence electron configurations of Y and La on the electronic structure and superconductivity.

The next important point to study would be to predict the trend of T_c under pressure and try to correlate with the FS topology change. Experimentally Huang et. al [81] have proposed the superconductivity of $LaSn_3$ to be highest among LaX_3 series and found an anomaly in T_c under pressure which was attributed to the FS topology change. The main point here is to analyze theoretically the FS topology change in the case of $LaSn_3$ and correlate with the superconducting transition temperature under pressure. Secondly one can expect the same anomaly in the case of the isostructural YSn_3 as both La and Y have no 'f' electron, whereas in our present work we have shown and discussed the possible reason for $LaSn_3$ and YSn_3 to behave differently. In the previous study on superconducting transition temperature in the (La,Th)Sn_3 alloy system [82], authors have attributed the singular behaviour of the electronic density of states in the vicinity of the Fermi level of $LaSn_3$ to be the main reason for the observed oscillatory behaviour of T_c as a function of alloy composition. Again Huang et. al [81] have correlated the irregular behaviour of T_c in $LaSn_3$ under pressure with the Fermi surface topology change, where these authors reported an initial increase in T_c with a maximum at a pressure around 0.8 GPa, beyond which T_c gradually decreases. Within the BCS framework of superconductivity, the change in T_c observed could reflect a change in the density of states at the Fermi level. The above discussion and findings stimulate us to search for the Fermi surface topology change in $LaSn_3$ theoretically under compression, which can be related to the variation of superconducting transition temperature and the density of states at the Fermi level. To understand the physical properties of these compounds in detail, we have shown the behaviour of FS topology and superconductivity in the isoelectronic and isostructural YX_3 and LaX_3 series of compounds with X = In, Tl, Sn, Pb, at ambient as well as under compression. Again it was noticed that among all LaX_3 and La_3X compounds, T_c was reported to be highest in La rich La_3In (T_c = 10.4 K [63]) and lowest in the case of In rich $LaIn_3$ with T_c = 0.7 K [82, 83] at ambient pressure. So it is quite important and interesting to analyze the origin of superconductivity in both the series of compounds. Apart from this it was reported experimentally that T_c increases with pressure in the case of La_3In [84]. To track the pressure dependence of T_c in X rich LaX_3 compounds as well as in La rich La_3X compounds, which can be related to the Fermi surface topology, it is most necessary to present a comparative study on both the series of compounds LaX_3 and La_3X. On the other hand experimentally Jing-Tai Zhao et. al [68] have synthesized La_3InZ (Z = N, O) type compounds and reported the superconducting behaviour at nearly 10 K for La_3InO, which is of the same range as that of La_3In, whereas the authors have not found any superconducting nature in La_3InN above 2 K. The addition of the Z (Z = N, O) atom in the body center of La_3In result in La_3InZ type inverse perovskite structure. Alternatively we can say that La_3InZ compounds originate from the

Cu_3Au type parent compound La_3In, without loosing the space group of the host compound, and this enable us to analyze the role of the Z atom in La_3InZ compounds. Apart from this the variation of superconducting transition temperature in La_3InZ compounds can also be correlated with the Fermi surface topology change and density of states at the Fermi level under compression, which will be discussed in the present work.

Overall the presence of high T_c in YX_3 compounds in comparison with LaX_3 for a particular X atom, though both La and Y possess no f-electron is the most interesting part among the studied AX_3 series of compounds. Secondly T_c being reported to be higher in La_3X compounds than LaX_3 together with the positive dependence of T_c under pressure in La_3In and positive dependence initially up to 0.8 GPa and negative dependence at higher pressure in $LaSn_3$ which is attributed to the FS topology change is another striking point to analyze. Apart from this T_c was reported to be almost the same with the inclusion of O in La_3In, but found to be suppressed with the inclusion of N in the same La_3In, provoking us to study in detail the electronic, Fermi surface and superconductivity of these series of AX_3 type compounds such as $LaIn_3$, $LaTl_3$, $LaSn_3$, $LaPb_3$, YIn_3, YTl_3, YSn_3, YPb_3, A_3X type compounds, La_3In, La_3Tl, La_3 Sn along with La_3InN and La_3InO.

In addition, we have extended our study to explore the electronic and Fermi surface topology of $LaRu_4X_{12}$ (X = P, As, Sb), well known filled skutterudites. Recent experimental study described the multigap superconductivity in $LaRu_4As_{12}$ [73] and the Fermi surface nesting feature in $LaRu_4P_{12}$ [72]. Again it is to be noted that, though X (X = P, As, Sb) belong to the same group in the periodic table a large difference in the superconducting transition temperature was noticed from the experimental report (7.2, 10.3 and 2.8 K respectively [71] in $LaRu_4X_{12}$ with X = P, As, Sb). Apart from this, from the recent experimental study it was found that T_c decreases under pressure in the case of $LaRu_4P_{12}$ [85] and in our present calculation we try to correlate this decreasing behaviour of T_c under pressure from the electronic structure calculation and also try to find out the origin of the superconductivity from the electronic structure. From the available experimental reports as explained above, various properties possessed by $LaRu_4As_{12}$ and $LaRu_4P_{12}$ trigger us to scrutinize these La based skutterudites $LaRu_4X_{12}$ with X = P, As, Sb.

Overall, we have studied the Fermi surface topology of 16 different compounds at ambient pressure as well as under compression and try to correlate the same with the density of states at the Fermi level, elastic constant, variation of the superconducting transition temperature within a particular series of compounds as well as among different series of the studied compounds.

In the present thesis we have described in detail the importance of Fermi surface in the field of condensed matter physics along with the review of the studied Cu_3Au type and skutterudite compounds and this forms our first chapter. The rest of the thesis is divided in to three parts, the second part which is our chapter 2 include the details of the methodology which is used to investigate the different class of the studied compounds, in chapter 3-7 we have presented the results and discussion of the compounds studied and the last chapter which is the 8^{th} chapter contains the conclusions and future plan. Here we are systematically presenting the summary of the rest of the chapters of our thesis.

Chapter-2: The description of the interacting many-particle systems is too complicated and it was solved by using several approximations. To predict the behaviour of any electronic system, one should be able to solve the Schrödinger equation which is having the wave functions in the form of $\psi(\mathrm{r}_1, \mathrm{r}_2, ..., \mathrm{r}_N)$, a function of $3N$ variables, where N is the number of particles. But it is difficult to solve the quantum mechanical problem with too many degrees of freedom. Thereafter several approximate methods evolved to model the interacting many-particle systems such as Hatree-Fock method, augmented plane wave method, orthogonalized plane wave method etc. In 1960's accurate and improved calculations are done on electronic structure after the density functional theory (DFT) based on the Hohenberg-Kohn theorem came to existence. Since 1990, the electronic structure calculation based on the density functional theory has a great success in determining the ground state properties and became more popular in condensed mater physics, chemistry and material science. DFT now serves as an excellent tool to have a basic and quantitative understanding of solids in condensed matter at microscopic level since it is based on quantum theory. In this chapter we have described the details of DFT and the full-potential linearized augumented plane wave method and pseudopotential method as implemented in WIEN2*k* and PWSCF code and an overview of the exchange-correlation functional such as local-density approximation (LDA) and generalized gradient approximation (GGA) is also presented.

Chapter-3: In this chapter we have discussed the electronic, elastic and Fermi surface properties of the AX_3 (A = La, Y; X = In, Tl,Sn, Pb) type compounds at ambient as well as under compression. Fermi surface topology change is observed for all the iso-structural AX_3 compounds under compression except in YSn_3 and YPb_3. The reason for the different FS behaviour noticed among these compounds are analyzed and discussed.

Chapter-4: This chapter elaborates the electronic and Fermi surface properties of La_3X (X = In, Tl, Sn) together with the comparative study of La_3X with LaX_3. We observed a strong interaction between the atoms in La_3X compounds, which is more pronounced than the LaX_3 type compounds and the reason for the same is also reported here. More interestingly we find the mechanical properties of all La_3X and LaX_3 compounds to be similar, although their electronic structures and Fermi surface topologies are different.

Chapter-5: Superconductivity of AX_3 (A = La, Y; X = In, Tl, Sn, Pb) and A_3X (A = La; X = In, Tl, Sn) compounds are analyzed under compression and we discuss the reason for T_c to be higher in A_3X compounds in comparison with AX_3 compounds in this chapter. Apart from this the opposite response of T_c with pressure in AX_3 and A_3X series of compounds is presented and taken up elaborately, as our calculations report T_c to increase with pressure in A_3X compounds and decrease with pressure in the case of AX_3 compounds. In addition the calculated superconducting transition temperatures of these compounds show a non-monotonic variation under pressure, where we have observed the FS topology change.

Chapter-6: The electronic structure, Fermi surface (FS) topology and superconducting properties of La_3InZ (Z = N, O) compounds are explained in this chapter and are compared with La_3In which is of the same space group, thereby emphasizing the role of Z atom in La_3InZ compounds. More interestingly FS topology change is observed only in La_3InO, but not in the case of La_3InN and the possible reason for this difference is also presented.

Chapter-7: In this chapter we have discussed the ab-initio calculation of the band structure, density of states and Fermi surface (FS) properties of filled skuterudittes $LaRu_4P_{12}$, $LaRu_4As_{12}$ and $LaRu_4Sb_{12}$, at ambient as well as under compression. A Fermi surface nesting feature in $LaRu_4P_{12}$ and FS topology change in the case of $LaRu_4As_{12}$ and $LaRu_4Sb_{12}$ under compression is shown here.

Chapter-8: This chapter contains the summary and future plan of the whole thesis. A non-monotonic variation of T_c was noticed for the compounds where we find the topology of the FS to change. The correlation of the non-monotonic variation of T_c with the FS topology change is verified for different series of compounds AX_3 (A = La, Y; X = In, Sn, Pb), La_3X (X = In, Sn, Pb) and La_3InO. Apart from these Cu_3Au type compounds, we have also analyzed the Fermi surface topology of the La based skutterudite $LaRu_4X_{12}$ (X = P, As, Sb) at ambient as well as under compression. As mentioned and discussed above, skutterudites are quite interesting and have promising application. Though it would be computationally quite expensive, it would be worthy to analyze the complete phonon dispersion of these compounds at ambient and under pressure, which might give us a complete insight about the electron-phonon coupling and the T_c of these compounds under pressure which would be taken up as a future work.

Chapter 2

Density Functional theory

To completely describe the quantum-mechanical behaviour of a system of N interacting electrons it is necessary to calculate its many-electron wave-function, since a solid typically contains around 10^{23} atoms. It is difficult to solve the corresponding Schrödinger equation. In the 1960's, Hohenberg, Kohn and Sham provided a powerful tool to solve the quantum states of many-electron systems: Density Functional Theory (DFT). The idea mentioned there is, the total particle density is the primary quantity from which properties of the system can be calculated and is sufficient to describe the macroscopic properties of the solid in its ground state. This chapter is an introduction to the key concepts in the density functional theory. The DFT band structure codes (focusing on WIEN2k and Quantum Espresso) will be explained in this chapter.

2.1 Background

With the introduction of the time independent Schrödinger equation, different approaches have come out to solve the equation that govern the interaction between the electrons and nuclei of solids and have received substantial attention by physicist and chemists. To find out the total energy of the system, a series of approximations have been used. The Schrödinger equation depends upon $3(n+N)$ number of variables, where n is the number of electrons and N is number of nuclei in a solid and it practically impossible to solve. Next by considering the Born-Oppenheimer approximation which we would discuss shortly, $3(n+N)$ variables may reduce to $3n$ variables but still difficult to solve. So based on the total electron density as a fundamental variable, density functional theory has evolved as a powerful tool in condensed matter physics to calculate different properties of the materials [86, 87, 88]. The significance of this method (DFT or first principles theory or *ab initio* calculation) is that, the wave function depends on $3n$ variables, whereas the electron density is a function of only 3 spatial variables, thereby reducing the computational cost. DFT is based on the Kohn- Sham equations. Kohn-Sham potential, in density functional theory appear as functional derivatives of energy with respect to the density. DFT is most widely used theory for calculating and providing sufficient information regarding various properties such as electronic structure including Fermi surface, magnetic properties, superconducting properties, elastic, mechanical properties etc even for large system.

2.2 The Many-body problem

In quantum mechanics, a solid is described by the many-particle (electron and nuclei) wave function. The starting point will be the time independent Schrödinger equation, which is

$$\hat{H}\psi = E\psi \tag{2.1}$$

Here $\hat{H}$ is the Hamiltonian, ψ is the wave function of the system, and E is the energy.

The Hamiltonian of the system again can be written as

$$\begin{aligned} \hat{H} \quad = \quad & -\sum_{i=1}^{N}\frac{\hbar^2}{2m_i}\nabla_i^2 + \frac{e^2}{2}\sum_{i=1}^{N}\sum_{i\neq j}^{N}\frac{1}{|r_i - r_j|} - \sum_{I=1}^{P}\frac{\hbar^2}{2M_I}\nabla_I^2 + \\ & \frac{e^2}{2}\sum_{I=1}^{P}\sum_{i=1}^{N}\frac{Z_I}{|r_i - R_I|} + \frac{e^2}{2}\sum_{I=1}^{P}\sum_{J\neq I}^{P}\frac{Z_I Z_J}{|R_I - R_J|} \\ & = T_e + V_{ee} + T_n + V_{en} + V_{nn} \end{aligned} \tag{2.2}$$

where $R = \{R_I, I = 1, 2, ...P\}$ is a set of P nuclear coordinates, and $r = \{r_i, i = 1, 2, ...N\}$ is a set of N electronic coordinates. Z_I, Z_J and M_I are the nuclear charges and masses, respectively, e and m_i are the electronic charges and masses, respectively. The first term, T_e = kinetic energy of the electron, second term, V_{ee} = potential energy of the electron, third term, T_n = kinetic energy of the nucleus, forth term, V_{en} = potential energy of the electron and nucleus and last term, V_{nn} = potential energy of the nucleus.

Since the motion of each electron is coupled to that of the other electrons in the system, in practice the above equation is not solvable analytically and approximations are needed.

2.2.1 Born-Oppenheimer approximation

In the Born-Oppenheimer approximation the electronic state is taken to be independent of the motion of the nuclei and depends only on their positions. Since the mass of the nuclei are much heavier than the electrons, the motion of the nuclei can be ignored in comparison with the electron, and we can consider the electrons as moving in the field of fixed nuclei. This is the Born-Oppenheimer approximation. So in the above equation (2.2) the third term can be neglected and the last term is just a classical constant which will be denoted as E_{II}. This Hamiltonian can be written in simplified form as

$$\begin{aligned} \hat{H} &= -\sum_{i=1}^{N} \frac{1}{2}\nabla_i^2 + \frac{1}{2}\sum_{i=1}^{N}\sum_{i\neq j}^{N} \frac{1}{|r_i - r_j|} + \frac{e^2}{2}\sum_{I=1}^{P}\sum_{i=1}^{N} \frac{Z_I}{|r_i - R_I|} + E_{II} \\ &= T_e + V_{ee} + V_{ext} + E_{II} \end{aligned} \tag{2.3}$$

In this above equation $\hbar = e = m_e = 1$ has been considered according to the atomic units. V_{ext} is the Coulomb potential arising from the nuclei.

For a system of N electrons with nuclear potential V_{ext}, the variational principle defines a procedure to determine the ground-state wave function ψ_0, and the ground-state energy, E_0. In other words, the ground state energy is a functional of the number of electrons N and the nuclear potential V_{ext}, i.e $\mathrm{E}_0 = \mathrm{E}[\mathrm{N}, \mathrm{V}_{ext}]$

2.2.2 The Hartree-Fock approximation

The Hartree-Fock method is a variational, wavefunction-based approach. Each electron feels the presence of the other electrons indirectly through an effective potential. Thus each orbital is affected by the presence of electrons in other orbital. Before Hatree-Fock, Hatree approximation has come out, but it fails to explain about the antisymmetry principle, which states that a wavefunction describing fermions should be antisymmetric with respect to the interchange of position of the electron. In this Hatree-Fock, the antisymmetry principle has been taken care. The wave function of the two electrons in Hatree approximation is

$$\psi_H(x_1, x_2) = \phi_1(x_1)\phi_2(x_2) \tag{2.4}$$

But to satisfy the antisymmetry principle we can write the wavefunction as:

$$\psi_{HF}(x_1, x_2) = \frac{1}{\sqrt{2}}[\phi_1(x_1)\phi_2(x_2) - \phi_1(x_2)\phi_2(x_1)] \tag{2.5}$$

For N electron system, this above equation can be written in determinant form, which is nothing but the Slater determinant.

$$\Psi(x_1, x_2, ..., x_N) = \frac{1}{\sqrt{N!}} \begin{vmatrix} \phi_1(x_1) & \phi_2(x_1)... & \phi_N(x_1) \\ \phi_1(x_2) & \phi_2(x_2)... & \phi_N(x_2) \\ . & . & . \\ . & . & . \\ . & . & . \\ \phi_1(x_N) & \phi_2(x_N)... & \phi_N(x_N) \end{vmatrix} \tag{2.6}$$

So from this, it emerges that the electron can move independently except that it experience Coulomb repulsion due to the interchange of the position, which is nothing but the exchange interaction of the electron. Hence in the Hatree fock model the exchange interaction of the electron is taken care. So the Hatree-Fock energy can be written as

$$\begin{aligned} E_{HF} = & \int \phi_i^*(r) \left(-\frac{1}{2} \sum_i^N \nabla_i^2 + V_{ext} \right) \phi_i(r) dr \\ & + \frac{1}{2} \sum_{i,j}^N \int \frac{\phi_i^*(r_1)\phi_i(r_1)\phi_j^*(r_2)\phi_j(r_2)}{|r_i - r_j|} dr_1 dr_2 \\ & - \frac{1}{2} \sum_{i,j}^N \int \frac{\phi_i^*(r_1)\phi_j(r_1)\phi_i(r_2)\phi_j^*(r_2)}{|r_i - r_j|} dr_1 dr_2 \end{aligned} \tag{2.7}$$

The second term is simply the classical Coulomb energy written in terms of the orbitals, which is nothing but Hatree-energy and the third term is the exchange energy. So the Hatree-Fock equation becomes

$$\left[-\frac{1}{2}\nabla^2 + V_{ext}(r) + V_H\right]\phi_i(r) + \int v_x(r, r^{'})\phi_i(r^{'})dr^{'} = \epsilon_i\phi_i(r) \tag{2.8}$$

V_H, in the equation (2.8) is the Hatree potential. The non-local exchange potential, v_x, is such that:

$$\int v_x(r, r^{'})\phi_i(r^{'})dr^{'} = -\sum_j^N \int \frac{\phi_j(r)\phi_j^*(r\prime)}{|r - r^{'}|}\phi_i(r^{'})dr^{'} \tag{2.9}$$

In order to compute the total energy we need to know the $3N$ dimensional wavefunction, which is still difficult. So in condensed matter physics this is the main motivation which paved way for the development and use of density functional theory.

2.3 Density functional theory

Density-functional theory (DFT) differs from the wave function based methods by using the electron density $n(r)$ as the starting point. An important advantage of using the electron density over the wave function is the reduction in dimensionality, i. e $3(n + N)$ to 3. A comprehensive discussions of DFT can be found in excellent review articles[89, 90] and textbooks[88, 91, 92].

First, the electron density is defined as

$$n(r) = N \int ... \int |\psi(x_1, x_2, ...x_N)|^2 dx_2...dx_N \tag{2.10}$$

and the total number of electrons is given by

$$\int dr^3 n(r) = N \tag{2.11}$$

2.3.1 Thomas-Fermi model

Thomas and Fermi[93, 94] independently considered a model for the first time where the kinetic energy is expressed in terms of the particle density $n(r)$. So the average kinetic energy per particle as a function of the particle density n is

$$\epsilon_{kin}(n) = C_F n^{2/3}, C_F = \frac{3}{10}(3\pi^2)^{2/3} \tag{2.12}$$

The kinetic energy per unit volume, E_{kin}, of a noninteracting homogeneous electron gas in the case is nϵ_{kin} and can be written as

$$E_{kin} \approx \int d^3 r n(r) \epsilon_{kin}(r) = C_F \int d^3 r n^{5/3}(r) \tag{2.13}$$

Thomas-Fermi model illustrated that the energy can be determined purely using the electron density.

2.3.2 Hohenberg-Kohn Theorems

In 1964 Hohenberg and Kohn[86] proved two theorems.

Theorem I: The electron density determines the external potential and the density is the ground state particle density $n_0(r)$. So for a given ground state density $n_0(r)$, it is possible to calculate the ground-state wave function $\psi_0(r)$ and vice versa and contain exactly the same information.

Theorem II : An universal functional for the energy $E[n]$ can be defined in terms of the density. The exact ground state is the global minimum value of this functional.
So for a given ground state density $n_0(r)$,

$$E_0 = min_{\psi \to n_0} \langle \psi | T_e + V_{ext} + V_H | \psi \rangle \tag{2.14}$$

2.3.3 The Kohn-Sham equations

The Kohn-Sham equation is based on the following assumption (called Kohn-Sham ansatz): The exact ground-state density can be represented by the ground-state density of an auxiliary system of non- interacting particles.

From the Hohenberg-Kohn Theorems the total energy of the system can be written as

$$E[n(r)] = \int V_{ext}(r) dr + F[n(r)] \tag{2.15}$$

But Kohn-Sham separated $F[n(r)]$ into three parts

$$F[n(r)] = T_e[n(r)] + \frac{1}{2}\int drdr'\,\frac{n(r)n(r^{'})}{|r-r'|} + E_{xc}[n(r)] \tag{2.16}$$

where $T_e[n(r)]$ is the kinetic energy of a non-interacting electron gas of density $n(r)$, and the second term of equation (2.16) is the classical electrostatic (Hartree) energy. $E_{xc}[n(r)]$ is the exchange-correlation energy.

From equation (2.15) and (2.16) we get the Kohn-Sham potential as

$$V_{ks}^{\sigma}(r) = \int dr'\,\frac{n(r^{'})}{|r-r'|} + V_{xc}^{\sigma}(r) + V_{ext}(r) \tag{2.17}$$

where the exchange-correlation potential $V_{xc}^{\sigma}(r)$ is defined as

$$V_{xc}^{\sigma}(r) = \frac{\delta E_{xc}[n(r)]}{\delta n(r,\sigma)} \tag{2.18}$$

and σ is the spin variable, $N = \sum_{\sigma} N^{\sigma} = N^{\uparrow} + N^{\downarrow}$

So the Kohn-Sham equation becomes

$$\left\{-\frac{1}{2}\nabla^2 + V_{ks}^{\sigma}(r)\right\}\psi_i^{\sigma}(r) = \epsilon_i^{\sigma}\psi_i^{\sigma}(r) \tag{2.19}$$

Here ψ_i^{σ} is defined as the Kohn-Sham one-electron orbitals and the electron density is defined as,

$$n(r) = \sum_{i}^{N_{occ}} |\psi_i(r)|^2 \tag{2.20}$$

By solving these above equations we will get the total energy of the Kohn-Sham equation as

$$E = E_{ks} = \sum_{i=1}^{N_{occ}} \epsilon_i - \int dr\left\{\frac{1}{2}V_H(r) + V_{xc}(r)\right\} n(r) + E_{xc} + E_{II} \tag{2.21}$$

Where $\sum_{i=1}^{N_{occ}} \epsilon_i = 2\sum_{i=1}^{N/2} \epsilon_i$

where $N_{occ} = N$. $E_{II}(R)$ represents the interaction between ions.

The Kohn-Sham equation must be solved self-consistently. The general procedure begin with an initial guess of the electron density, construct the V_{ks}^{σ} from Eq. (2.17), and then get the Kohn-Sham orbitals. Based on these orbitals, a new density is obtained from Eq. (2.20) and the process is repeated until convergence is achieved. Finally, the total energy will be calculated from Eq. (2.21) with the final electron density and the flow chart depicting the method of solving Kohn-Sham equation is given in Fig. 2.1.

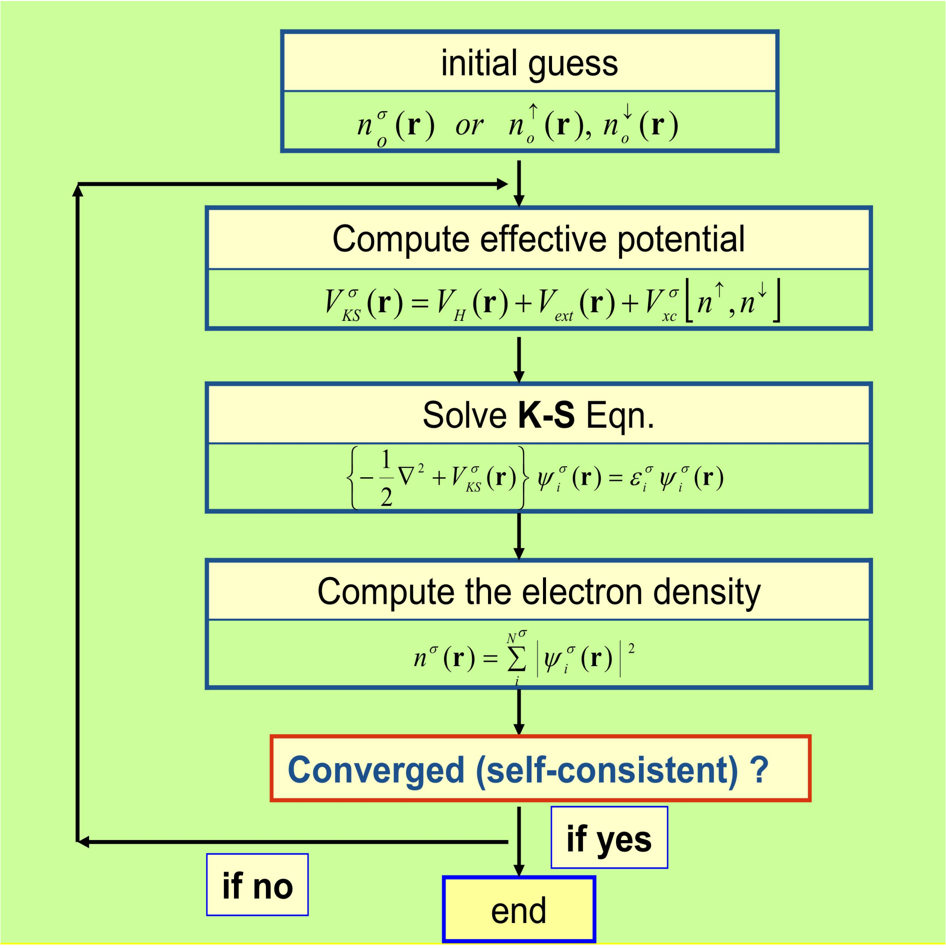

Figure 2.1: Flow chart of the Kohn-Sham equation, (figure is taken from online resource).

If each term in the Kohn-Sham energy functional was known, we would be able to obtain the exact ground state density and total energy. This expression of E_{ks} (or ϵ_i) would be exact if the exact functional $E_{xc}[n]$ is known. Unfortunately, there is one unknown term, the exchange-correlation (xc) functional ($E_{xc}[n]$). Since E_{xc} is not known exactly, it is necessary to approximate it, which is the focus of the next section.

2.3.4 Exchange-Correlation Functionals

Even since the people started using DFT, some approximation for E_{xc} have been used and local density approximation (LDA) and genelarized gradient approximation (GGA) are widely used.

Local Density Approximation (LDA)

The LDA uses the exchange-correlation energy of the homogeneous electron gas. Here, the electrons are exposed to a constant external potential, i.e., the nuclei are replaced by a homogeneous positive charge density. Thus, the total exchange-correlation energy of the system can be written as

$$E_{xc}^{LDA}[n] = \int n(r)\epsilon_{xc}^{hom}(n(r))dr \tag{2.22}$$

where ϵ_{xc}^{hom} is the exchange-correlation energy per particle of the interacting homogeneous electron gas of density $n(r)$. The LDA is valid for slowly varying densities such as the weakly perturbed electron gas. Indeed LDA works well, especially for metals. However, many studies have shown that LDA tends to overestimate cohesive energies, bulk modulus and underestimates lattice constants. The Perdew-Zunger (PZ)[95] and Perdew-Wang (PW)[96] functionals are common LDA functionals.

Genelarized Gradient Approximation (GGA)

In LDA one uses the knowledge of the density in a point r. In real systems the density varies in space. For the rapidly varying electron densities of many materials a reasonable approximation has to be considered and the gradient of the density ($\nabla n(r)$) needs to be included. In GGA, the densities of the surrounding infinitesimal volumes are considered, which means the gradient of the density plays a role. Numerically it is defined as

$$E_{xc}^{GGA}[n] = \int f^{GGA}(n(r), \nabla n(r))dr \tag{2.23}$$

GGA improves significantly on the LDA's description of the binding energy of molecules. A number of functionals within the GGA family[97, 98, 99, 100] have been developed.

2.4 Linearized Augmented Planewave (LAPW) Method

In our thesis, we have used the Linearized Augmented Plane wave (LAPW) method as implemented in WIEN2*k* to calculate the material properties. LAPW method is the most accurate methods for performing electronic structure calculations for crystals. To solve the Kohn-Sham equation, which further help us to calculate the ground state density, total energy, eigen values of a many-electron system, a basis set has to be introduced. In this method the unit cell is divided into two parts: spheres around each atom (muffin tin sphere), where wave functions are rapidly varying, i. e. atomic like and the interstitial region, where the wave functions are smoothly varying and satisfy the condition that the wave function and their derivatives are continuous at the boundary. In the WIEN2*k* [101] code the parameter energy cutoff, E_{cut} separate the core region which is confined in the muffin tin sphere from the valence state which is treated as the interstitial region as per above discussion. The muffin tin radius is controlled by the parameter R_{MT}. So the basis function is a plane wave in the interstitial region and inside the sphere it is atomic like function.

$$\phi_{k_n} = \begin{cases} \Omega^{-1/2} e^{ik_n r} & \text{outside sphere} \\ \sum_{lm} [A_{lm} u_l(r, E_l) + B_{lm} \dot{u}_l(r, E_l)] Y_{lm}(\hat{r}) & \text{inside sphere} \end{cases} \tag{2.24}$$

Where $Y_{lm}(\hat{r})$ is the spherical harmonics and $u_l(r, E_l)$ is the solution of the radial schrödinger equation for energy E_l and azimuthal quantum number l and $\dot{u}_l$ is its energy derivative evaluated at a fixed linearization energy E_l. A_{lm} and B_{lm} are chosen such that basis functions are continuous and smooth at sphere boundaries, and k_n=k+K_n;K_n are the reciprocal lattice vectors and k is the wave vector inside the Brillouin zone.

According to the linear variation method, the solution of the Kohn-Sham equations are expanded as follows.

$$\phi_k = \sum_n c_n \phi_{k_n} \tag{2.25}$$

where the coefficients c_n are determined by the Rayleigh-Ritz variational principle. The convergence of the basis set is controlled by the cut-off parameter R_{MT} K_{Max}, R_{MT} is the smallest atomic sphere (Muffin-Tin sphere) and the K_{Max} is the magnitude of the largest K vector (plane-wave cut-off).

The potential (and charge density) can be of general form, no shape approximation is considered and this is called full-potential.

$$V(r) = \begin{cases} \sum\limits_{lm} V_{lm}(r) Y_{lm}(\hat{r}) & \text{inside sphere} \\ \sum\limits_{K} V_K e^{iKr} & \text{outside sphere} \end{cases} \tag{2.26}$$

2.5 Pseudopotential method

Since most of the material properties depend upon the valence electrons, one can distinguish core and valence electrons and this is implemented in the pseudopotential method. In this method the core electrons are replaced by a pseudopotential. This method is simple and requires lesser computational resources. So it is easier to solve the heavier system with more electrons. The pseudo potentials will be set in such a way that the pseudo wavefunction must not have any radial nodes within the core region and at a certain distance, r_c the pseudo wavefunction becomes equal to the real wavefunction.

The criteria which it must satisfy is that, the pseudo wavefunctions and pseudopotential should be identical to the all electron wavefunction and potential outside a radius of cut-off r_c. In addition pseudo wavefunctions must be continuous at r_c as well as its first and second derivative and also be non-oscillatory. So to get the pseudo potential, the all-electron(AE) Schrödinger equation has to be solved:

$$\left(\frac{1}{2}\nabla^2 + V\right) \psi_l^{AE} = \epsilon \psi_l^{AE} \tag{2.27}$$

Here ψ_l^{AE} is the wavefunction for the all electron (AE) atomic system with angular momentum component l. The pseudo wavefunction is of the form

$$\psi_l^{ps} = \sum_{i=1}^{n} \alpha_i j_l \tag{2.28}$$

Where j_l are the spherical Bessel functions and α_i is the fitting parameter. The scattering properties of pseudo-potential or pseudo wavefunction are identical to the all-electron scattering properties, i. e it is an angular dependent quantity. A pseudo-potential that satisfy this constraint is called norm-conserving pseudopotential. The schematic diagram for all-electron and pseudo potential and the corresponding wavefunctions are presented in Fig. 2.2.

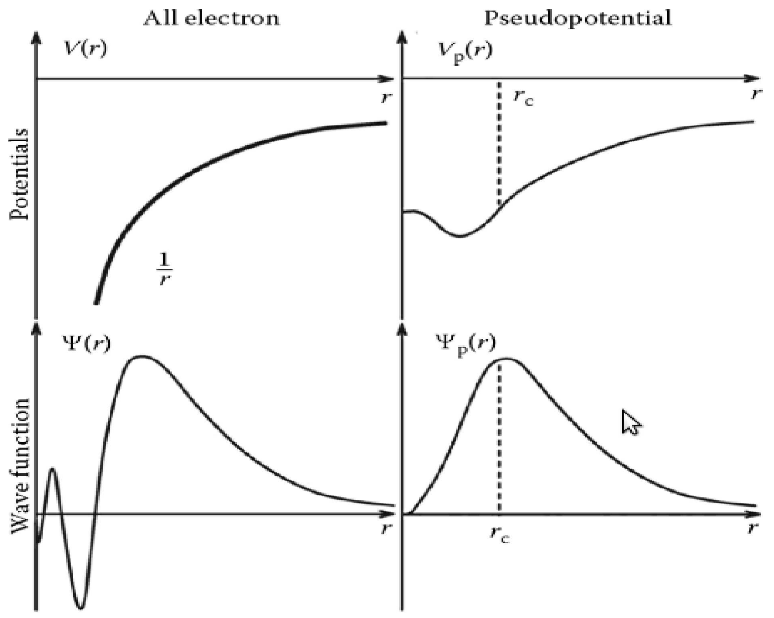

Figure 2.2: Schematic diagram of the potential and wave function for all-electron and pseudopotential schemes. Outside of the core radius, r_c, the potential and wave functions are identical. The figure is taken from Ref.[102].

Limitation of norm-conserving pseudo-potential

The norm-conserving pseudo-potentials are still hard and require a large plane wave basis sets, and consume more computational time.

Ultrasoft pseudo-potentials

Throughout this work to study the phonon and dynamical properties of the material the ultrasoft pseudo-potentials (USPP) have been used as implemented in Quantum Espresso package[103, 104]. The USPP generator is developed by Professor David Vanderbilts group[105]. To generalize the eigen value problem, they defined an operator $\hat{S}$ such that the pseudo-wavefunction $|\phi_{nk}\rangle$ satisfy the orthonormalization condition:

$$\left\langle \phi_{nk}|\hat{S}|\phi_{n'k'} \right\rangle = \delta_{nn'} \tag{2.29}$$

The orbital in the core region are allowed to be soft and low kinetic energy cut-off is used. The obtained integral of the charge-density distribution of each pseudo-wavefunction inside the core region and all-electron wave function is different. The Hamiltonian is solved by introducing the operator $\hat{S}$.

$$\hat{H}|\phi_{nk}\rangle = \epsilon_{nk}\hat{S}|\phi_{nk}\rangle \tag{2.30}$$

To conserve the total charge, the valence charge-density is redefined and the details of the calculations are found elsewhere[105]. Pseudo-potentials obtained using this method are called ultrasoft.

2.6 The de Haas van Alphen effect

Fermi surface is an important feature for the metallic system, as most of the material properties depend upon the valence electrons. A programme called "Supercell K-space Extremal Area Finder" (SKEAF)[106], which is interliked to the WIEN2k can be used to calculate the de Haas van Alphen effect, effective mass etc. from the calculated Fermi surface, and we have used the same in our present study on skutterudites.

Chapter 3

Pressure effect on Fermi surface topology of AX_3 compounds

The electronic structure, density of states, Fermi surface (FS), and elastic properties of the isostructural and isoelectronic AX_3 (A = La, Y; X = In, Tl, Sn, Pb) intermetallic compounds are studied under pressure, within the framework of density functional theory including spin-orbit coupling. The states at the Fermi level (E_F) are dominated by X '*p*' states with significant contributions from the A '*d*' states. Under ambient conditions, all AX_3 compounds are found to have two Fermi surface sheets, except YSn_3, where we have an extra electron sheet and the same is found to appear in $LaSn_3$ under compression ($V/V_0 = 0.94$, pressure (P) = 1 GPa). Among the two sheets the second one appears to be more complex. Fermi surface topology changes are observed within the complex sheet for all the isostructural AX_3 compounds under compression except in YSn_3 and YPb_3. The reason for the different FS behaviour noticed between $LaSn_3$ and YSn_3 could be mainly due to the effect of spin-orbit coupling (SOC), leading to considerable change near the vicinity of the Fermi level particularly at the X point, which is well explained using the band structure calculation. In the case of $LaPb_3$, softening of the C_{44} elastic constant under pressure may be related to the appearance of a new hole pocket around the X point in the same complex sheet, leading to the observed FS topology change, which is absent in YPb_3, despite the electronic structures being similar in $LaPb_3$ and YPb_3 at ambient.

3.1 Introduction

The RX_3-type (R = rare earth elements, X = In, Sn, Tl, Pb) intermetallic compounds, which crystallize in the simple cubic Cu_3Au-type structure, have been the subject of many experimental and theoretical investigations because of their diverse properties such as oscillatory behaviour in superconducting property, magnetic susceptibility and thermopower, as a function of their valence electron concentration [82, 49, 107]. At first, this behaviour was interpreted in a nearly-free electron model as a reflection of the Fermi surface close to the Brillouin zone boundary [61, 108], a viewpoint later contested by Grobman [109] where the authors concluded that these compounds behave like transition metal. Many of these compounds are superconductors. Some of the RX_3 compounds, such as $PrSn_3$ and $NdSn_3$, are found to order antiferromagnetically at T_N= 8.6 K and 4.5 K, respectively [110] and $CeSn_3$ has been categorized as a dense Kondo compound exhibiting valence fluctuations [111]. The pressure dependence of the superconducting transition temperature of $LaSn_3$ is anomalous, as shown by Huang et. al [81] in which these authors expect the same to be driven by a Fermi surface topology change. Recently Bittar et. al [112] found that the effective exchange interaction parameter of $LaIn_{3-x}Sn_x$ decreases by substitution of Sn in $LaIn_3$ and suggested that it might be due to the increase of the lattice parameter. Canepa et. al [113] explained the anomalous behaviour of the heat capacity at constant volume (C_v) for $LaPb_3$ with temperature. Recently, the superconducting transition temperature (T_c) of $LaIn_3$ has been reported to be 1.08 K, 0.95 K and 0.9 K by resistivity, susceptibility and heat capacity measurements, respectively [114]. To understand and explore the various properties of AX_3 intermetallic compounds, we have examined the electronic structure of AX_3 (A = La, Y and X = In, Tl, Sn, Pb) at ambient as well as at high pressure. A number of studies are available on the band structures of $LaSn_3$ and YSn_3 [115, 116, 117, 118], while less efforts have been devoted for the studies related to pressure dependence of the electronic structure, Fermi surface and elastic properties of these compounds. Hence we focus our attention in this chapter on analysing the pressure induced FS topology change in AX_3 type compounds, which might be associated with the anomalous behaviour of T_c under pressure. In the present study, we calculate the FS of AX_3 and indeed observe a change in topology under pressure for all compounds except in YSn_3 and YPb_3, despite the electronic structures being similar at ambient. The rest of the chapter is organized as follows: section-3.2 describes the method of calculation used in this study. The results and discussions are presented in section-3.4, while section-3.4 concludes this chapter.

3.2 Method of calculation

The calculations were performed using the full-potential linearized augmented plane wave (FP-LAPW) method [119] as implemented in the WIEN2*k* computer code [101], based on density functional theory (DFT) [86], which has been shown to yield reliable results for the electronic and structural properties of crystalline solids. All the calculation were performed with the inclusion of spin-orbit coupling (SOC). For the exchange-correlation functional the local density approximation (LDA) in the form proposed by Perdew and Wang [96] was used. In order to achieve desired convergence on the energy eigenvalues, the wave functions in the interstitial region were expanded using plane waves with a cutoff of $\mathrm{R}_{MT}\mathrm{K}_{max}= 9$, where K_{max} is the plane wave cut-off, and R_{MT} is the muffin tin radii. The charge density was Fourier expanded up to $G_{max} = 9$ (a.u.$^{-1}$). We carried out convergence tests for the charge-density Fourier expansion using higher G_{max} values and found no significant changes in the calculated properties. The muffin-tin radii were chosen as 2.95 a.u for both La and Y and 2.85 a.u for the X atoms. A (32 × 32 × 32) *k*-point mesh in the Monkhorst-Pack [120] scheme was used during the self-consistency cycle. The total energy was converged up to 10^{-6} *Ry*. The Birch-Murnaghan equation of state [121] was used to fit the total energy as a function of unit cell volume to obtain the equilibrium lattice constants and bulk moduli for the investigated systems. A (44 × 44 × 44) *k*-mesh, corresponding to 2300 *k*-points in the irreducible part of the Brillouin zone (BZ), was used for the FS calculations to ensure accurate determination of the Fermi level. The three-dimensional FS plots were generated with the help of the XCrySDen ((*X*-Window) CRYstalline Structures and DENsities) molecular structure visualization program [122].

The elastic constants have been calculated within the total-energy method, where the unit cell is subjected to a number of small amplitude strains along several directions. The elastic constants of solids provide links between the mechanical and dynamical properties of the crystals. In particular, they provide information on the stability and stiffness of materials. It is well known that a cubic crystal has only three independent elastic constants [123, 124, 125] C_{11}, C_{12} and C_{44}. From these one may obtain the Hill's [126] shear modulus G_H, (which is the arithmetic mean of the Reuss, G_R [127] and Voigt, G_V [128] approximations), Young's modulus E, and the Poisson's ratio σ by using standard relations.

$$G_V = \frac{C_{11} - C_{12} + 3C_{44}}{5} \tag{3.1}$$

$$G_R = \frac{5(C_{11} - C_{12})C_{44}}{4C_{44} + 3(C_{11} - C_{12})} \tag{3.2}$$

$$G_H = \frac{G_V + G_R}{2} \tag{3.3}$$

$$\sigma = \frac{3B - 2G_H}{2(3B + G_H)} = \frac{1}{2}(1 - \frac{E}{3B}) \tag{3.4}$$

$$E = \frac{9BG_H}{3B + G_H} \tag{3.5}$$

For a completely isotropic system, the anisotropy factor (A) takes the value of unity and the deviation from unity measures the degree of elastic anisotropy and can be calculated from the equation given below.

$$A = \frac{2C_{44}}{C_{11} - C_{44}} \tag{3.6}$$

Furthermore, the Debye temperature may be obtained in terms of the mean sound velocity v_m:

$$\Theta_D = \frac{h}{k_B} \left(\frac{3n\rho N_A}{4\pi M} \right)^{1/3} v_m, \tag{3.7}$$

where h, k_B and N_A are Planck's, Boltzmann's constants, and Avogadro's number, respectively. ρ is the mass density, M is the molecular weight, and n is the number of atoms in the unit cell. The mean sound velocity is defined as:

$$v_m = \left[\frac{1}{3} \left(\frac{2}{v_t^3} + \frac{1}{v_l^3} \right) \right]^{-1/3}, \tag{3.8}$$

where v_l and v_t are the longitudinal and transverse sound velocities, which may be obtained from the shear modulus G_H and bulk modulus B as:

$$v_l = \sqrt{\frac{(B + \frac{4}{3}G_H)}{\rho}} \tag{3.9}$$

and

$$v_t = \sqrt{\frac{G_H}{\rho}}. \tag{3.10}$$

Table 3.1: Calculated lattice constant, a (in Å) and bulk modulus, B (in GPa) for AX_3 (A = La, Y; X = Sn, Pb, In, Tl). The bulk moduli are evaluated at the theoretical equilibrium volumes. Experimental values are quoted for comparison. The experimental lattice constants which we have used in our present calculation for $LaSn_3$, $LaPb_3$, $LaIn_3$, $LaTl_3$, YSn_3, YPb_3, YIn_3, and YTl_3 are 4.774Å, 4.903Å, 4.725Å, 4.799Å, 4.667Å, 4.813Å, 4.592Å and 4.678Å respectively.

Compounds		Lattice constant	B
$LaSn_3$	present work	4.70	68
	Expt	4.774^a,4.769^b	52^c
	Others^d	4.73	
$LaPb_3$	present work	4.838	62
	Expt.	4.903^a,4.905^e	
$LaIn_3$	present work	4.66	64
	Other Theory	$4.70,^d$ 4.925^f	$59,^d$ 73^f
	Expt.	4.739^e,4.725^g,4.735^h	
$LaTl_3$	present work	4.747	62
	Expt.	4.806^a, 4.799^e	
YSn_3	present work	4.61	71
	Expt.	4.667^i	
YPb_3	present work	4.76	63
	Expt.	4.813^a,4.823^h	
YIn_3	present work	4.514	70
	Expt.	4.592^a,4.594^h,4.593^j	
YTl_3	present work	4.615	66
	Expt.	4.678^e,4.68^h	

a: Ref. [129]; b: Ref. [130]; c: From elastic constants obtained in Ref. [131]
d: LMTO-ASA, Ref. [132]; e: Ref. [82]; f: ASW, Ref. [133];
g: Ref. [134]; h: Ref. [135]; i: Ref. [80]; j: Ref. [136].

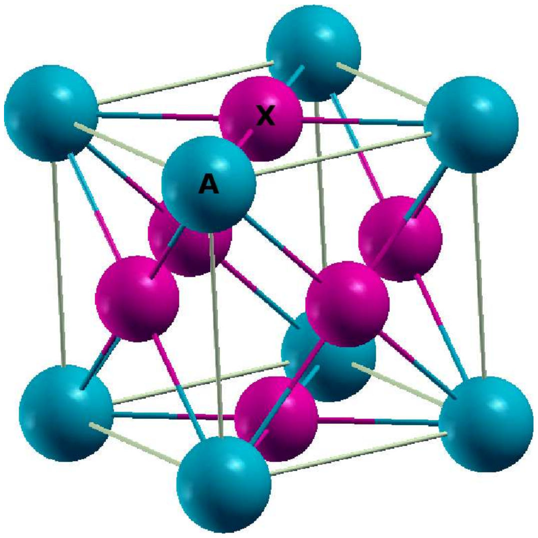

Figure 3.1: Crystal structure of AX_3 (A = La, Y; X = In, Tl, Sn, Pb) compounds.

3.3 Results and discussions

3.3.1 Crystal structure and ground state properties

AX_3 (A = La, Y; X = In, Tl, Sn, Pb) intermetallic compounds crystallize with space group $Pm\bar{3}m$ (no. 221) which is a simple cubic lattice. The A atoms are placed at (0.0, 0.0, 0.0) and X are located at (0.0, 0.5, 0.5) and the crystal structure is presented in Fig. 3.1.

The calculated equilibrium lattice parameter, a and zero-pressure bulk modulus, B are listed in Table-3.1. The results are in good agreement with available experimental data and other earlier calculations. The lattice constants are slightly underestimated with respect to their experimental values, between 1.1% (for $LaTl_3$) and 1.7% (for YIn_3), which is a well-known deficiency of the LDA. No experimental results are available for the bulk modulus. The calculated bulk modulus for all the compounds are very similar, between 62 and 70 GPa.

3.3.2 Band structure and density of states

Figures 3.2 and 3.3 shows the band dispersions along the high symmetry directions for AX_3 series of compounds with X = Sn, Pb and X = In, Tl, respectively at experimental volume (V_0). The band structure of $LaSn_3$ with SOC compares well with the earlier work [116, 117] and our calculated band structure of $LaIn_3$ is quite similar to that of Ref.[132]. Overall, the band structures of $LaSn_3$ and YSn_3 are very similar, as reported in Ref. [118], which also discussed the effect of SOC. The major difference between the two compounds in the vicinity of the Fermi level, E_F, occurs at the X point,

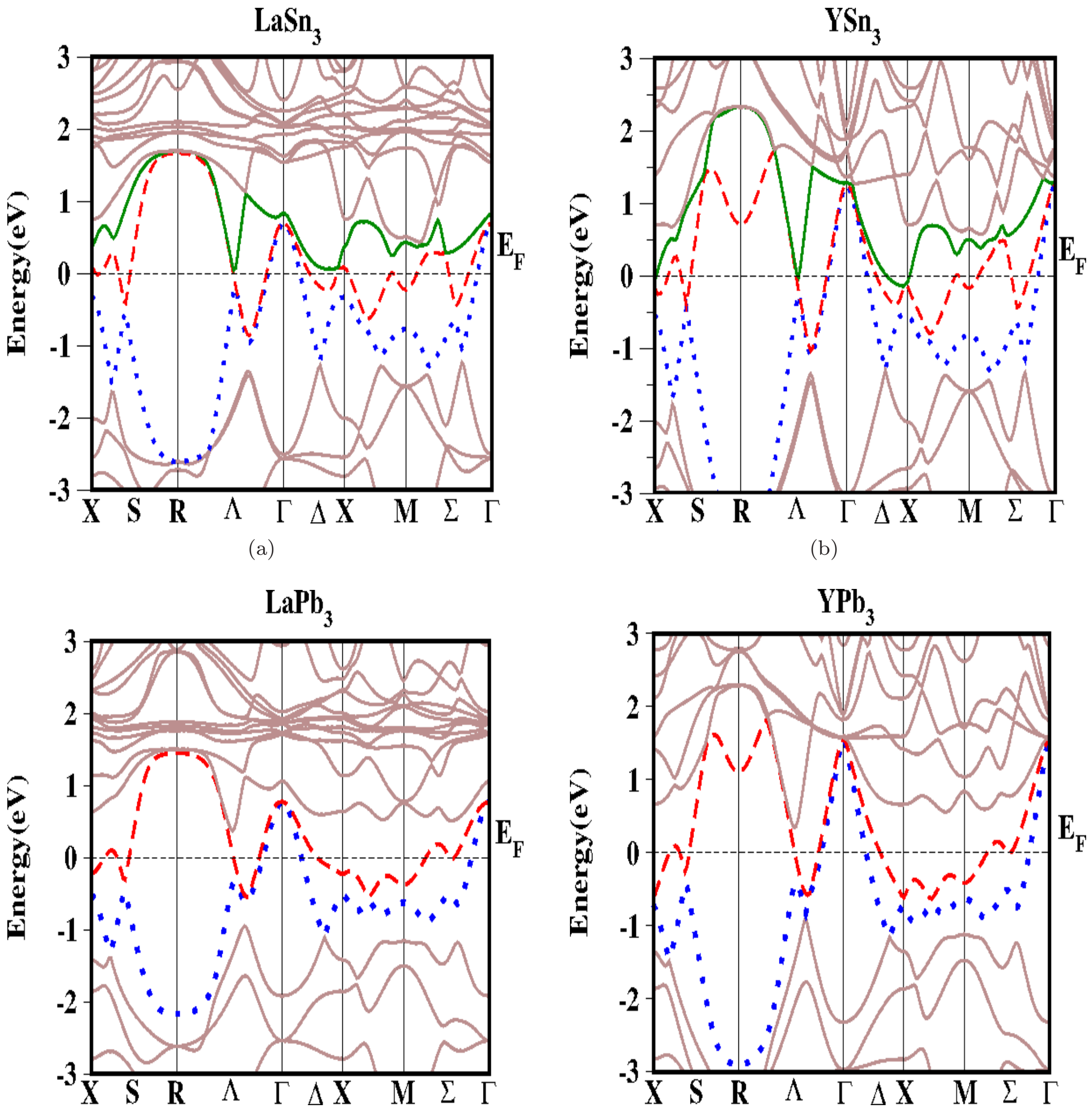

(a)

(b)

(c)

(d)

Figure 3.2: Band structure of AX_3 (A = La, Y; X = Sn, Pb) compounds at their experimental lattice constants. Two bands cross the Fermi level, marked in the plots by a red dashed line and a blue dotted line, except in YSn_3 (an extra band crosses, green solid line).

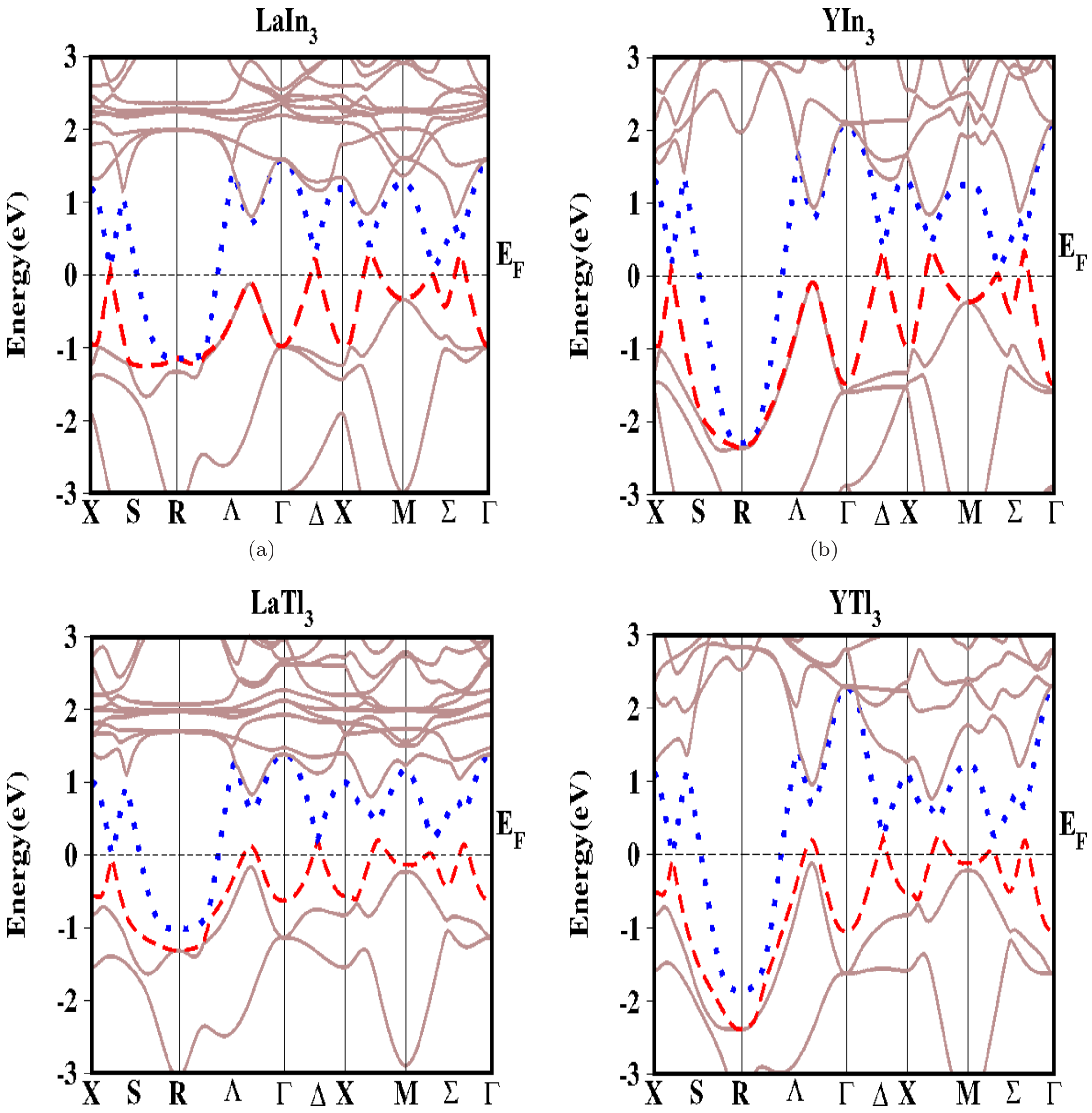

(a) (b)

(c) (d)

Figure 3.3: Band structure of AX$_3$ (A = La, Y; X = In, Tl) compounds at their experimental lattice constants. Two bands cross the Fermi level, marked in the plots by a red dashed line and a blue dotted line.

where a band crosses the E_F for $LaSn_3$, but stays below E_F for YSn_3. This gives rise to a small hole pocket around the X point in $LaSn_3$, which does not appear for YSn_3 (and which would not be if SOC is not included) and is evident from the Fig. 3.4 (a, c). A second, less significant feature, is a very dispersive band along $\Gamma - R$, which dips below E_F for YSn_3, but stays above E_F for $LaSn_3$. This is illustrated from Fig. 3.4 (b, d). This band contributes to the third Fermi surface of YSn_3 which in $LaSn_3$ only appears under pressure. Comparing the band structure of all the remaining investigated AX_3 compounds for A = La, Y and X = Pb, In, Tl, it is evident that the bands in the vicinity of the Fermi level for LaX_3 and YX_3 look very similar along all the high symmetry lines at zero pressure. In contrast, the electronic structure of $LaSn_3$ and YSn_3 [118] did display some discrepancies around E_F, particularly in the regions close to the X and M points in the Brillouin zone. On the other hand, when comparing the electronic structures of the AX_3 compounds with the same A but varying X some minor deviations are seen. For X = Sn, Pb, which corresponds to an average valence electron count (number of valence electrons per atom) of $n = 3.75$, slight differences around the X and M points are evident from comparison of the band structures in Figs. 3.2 (a, b) for the Sn compounds with their Pb counterparts in Figs. 3.2 (c, d). For X= In, Tl, having valence electron count $n = 3$, deviations in the band structure along the Λ and S symmetry lines are observed, in Fig. 3.3 (a, c) for A = La and in Fig. 3.3 (b, d) for A = Y. For AIn_3, in Figs. 3.3 (a) and 3.3 (b), the band marked in red crosses E_F twice along the S line but not along Λ. In contrast, for ATl_3 the same (red coloured, broken line) band in Figs. 3.3 (c) and 3.3 (d) does not cross E_F along S, but crosses twice along Λ. These minor differences lead to slight differences also in the FS of the AX_3 compounds, which we discuss in succeeding subsection.

The densities of states are included in Fig. 3.5 and 3.6. In all the AX_3 compounds, we find strong hybridization between the X 'p' states and the A 'd' states in the region around the Fermi level. The La 'f' bands contribute a large density of states around 2 eV above the Fermi level in the LaX_3 compounds, which naturally is absent in the YX_3 homologues. These unoccupied La '$4f$' bands overlap with the La '$5d$' bands, with some influence on the energy band structure in the vicinity of the Fermi energy. This is illustrated with the density of states, which is shown in Fig. 3.5 (a, c) and 3.6 (a, c) for LaX_3 with X = Sn, Pb and In, Tl, respectively. A distinct difference between La and Y is the proximity of the 'f' levels of La to the Fermi energy, which introduces 'f' hybridization into the states around the Fermi level in the La compounds. The similarity between the Fermi surfaces of the La and Y compounds (we discuss in next paragraph) show that this 'f' hybridization into the bands around the Fermi level is rather insignificant for X = In, Tl, Pb. From the partial densities

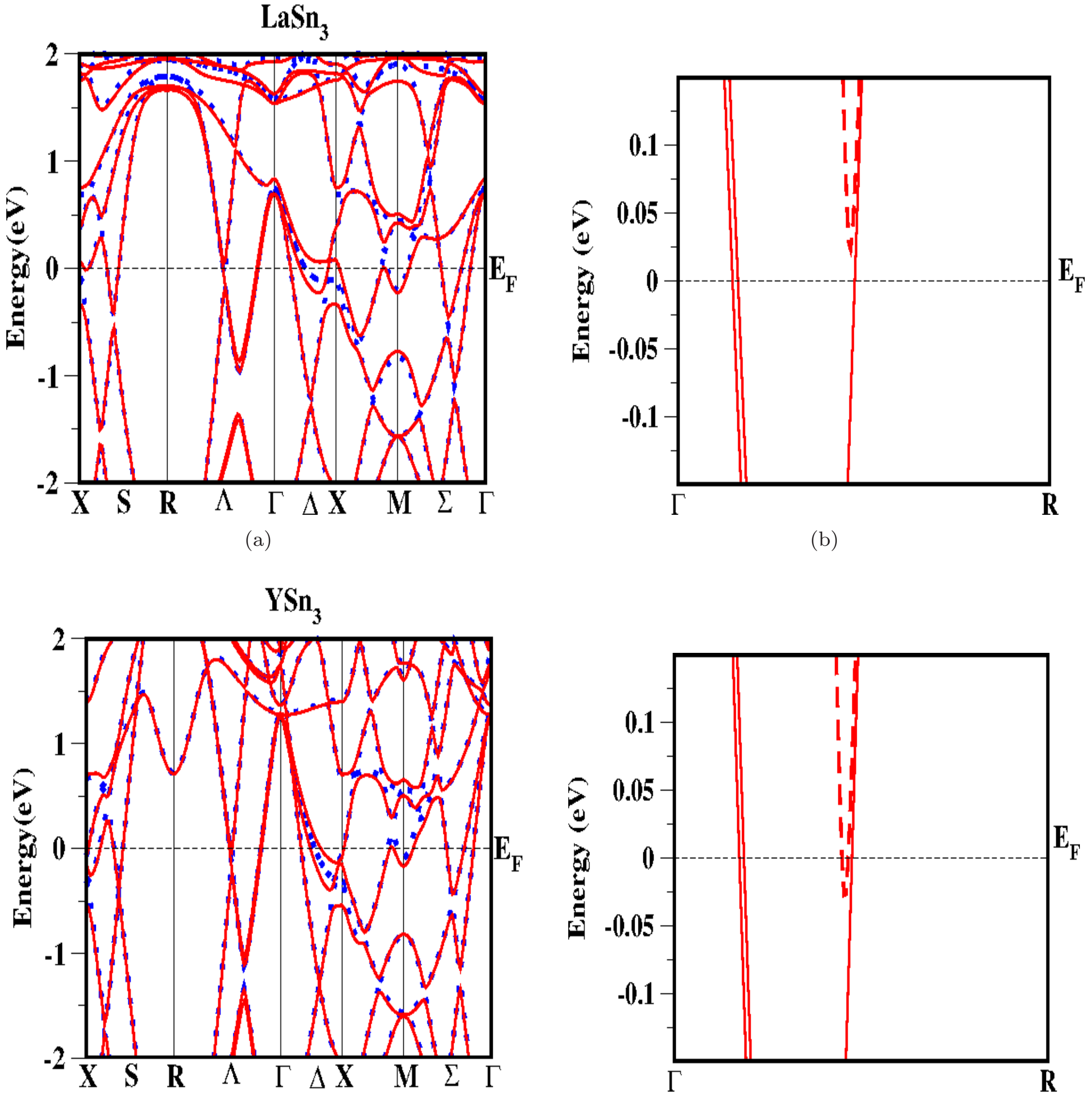

(a) (b)

(c) (d)

Figure 3.4: Electronic band structures of (a) $LaSn_3$ with and without SOC, (b) zoomed region along Γ-R direction for $LaSn_3$ with SOC, (c) YSn_3 with and without SOC and (d) zoomed region along Γ-R direction for YSn_3 with SOC. The solid lines (red colour) show the electronic levels calculated with SOC, while the dotted lines (blue colour) show the electronic levels as calculated without SOC. The energies are given in eV relative to the Fermi level, E_F, which is marked with the horizontal dashed line.

of states, examplified for LaX_3 and YX_3 with X = Pb, In, Tl, in Figs. 3.5 (c, d) and 3.6 (a-d), the La '*d*' states are seen to have larger weight at E_F than the La '*f*' states. In contrast, for $LaSn_3$ (Fig. 3.5 (a)) the La '*f*' states contribution to the density of states at the Fermi level was found to be relatively larger as evident from Figs. 3.5 (a) and (b), which in combination with the SOC leads to the slight differences in the band structures between $LaSn_3$ and YSn_3. For the remaining AX_3 compounds, X being In, Tl or Pb, the effects of SOC are very similar in the La and Y homologues. Interestingly, the Sn compounds reveal (see Fig. 3.5 (a, b)) a pseudogap only below E_F [118]. In the Pb compounds distinct pseudogaps appear both above and below E_F as shown in Figs. 3.5 (c, d). In the Tl compounds a pseudogap appears only above E_F, while no particular features appear around E_F for the In compounds, which is also evident from Figs. 3.6 (a-d). So we may rationalize such that the pseudogap above E_F is a feature associated with the heavier X elements Tl and Pb, while the pseudogap below E_F is a feature of the $n = 3.75$ compounds with X=Sn, Pb.

3.3.3 Fermi surface topology at ambient and under pressure

Looking next at the Fermi surfaces of AX_3 compounds, (displayed in Fig. 3.7-3.10) in all cases two FS sheets are observed with the exception of YSn_3, for which a small third surface exists as displayed in Fig. 3.7 (e) (see solid green color band in Fig 3.2 (b)). Among the two surfaces, one surface is the complicated surface as evident from Fig. 3.7 (b, d) for ASn_3, Fig. 3.8 (b, d) for APb_3, Fig. 3.9 (a, c) for AIn_3 and Fig. 3.10 (a, c) for ATl_3 and the other surface consists of hole pocket centered at Γ point for X = Sn, Pb as shown in Fig. 3.7 (a, c) for ASn_3, Fig. 3.8 (a, c) for APb_3 and it is a electron pocket around the R point in the Brillouin zone for X = In, Tl as shown in Fig. 3.9 (b, d) for AIn_3 and Fig. 3.10 (b, d) for ATl_3 at zero pressure. For the same element A, we find larger differences for the complex Fermi sheet depending on the X element. Thus, comparing $LaSn_3$ and $LaPb_3$ (Fig. 3.7 (b), 3.8 (b)), the connectivity on the faces of the cubic Brillouin zone (which include points X and M) differs. Similar conclusions are reached for $LaIn_3$ and $LaTl_3$ (Fig. 3.9 (a) and 3.10 (a)) as well as for YIn_3 and YTl_3 (Fig. 3.9 (c) and Fig. 3.10 (c)). For YSn_3 [118] and YPb_3, Fig. 3.7 (d), Fig. 3.8 (d), the connectivity in the vicinity of the M points (i. e. the middle of the cube edges) is different with a detached electron pocket in the former case. The topology of the Fermi surface of LaX_3 is found to be similar with YX_3 for X = Pb, In, Tl at ambient pressure, as shown in Fig. 3.8, 3.9, 3.10 (a, b) for La containing compounds and 3.8, 3.9, 3.10 (c, d) for Y containing compounds, which is again illustrating the dominating nature of the X '*p*' like states in the vicinity of the Fermi level and less importance of '*f*' hybridization at the vicinity of the Fermi level as discussed above.

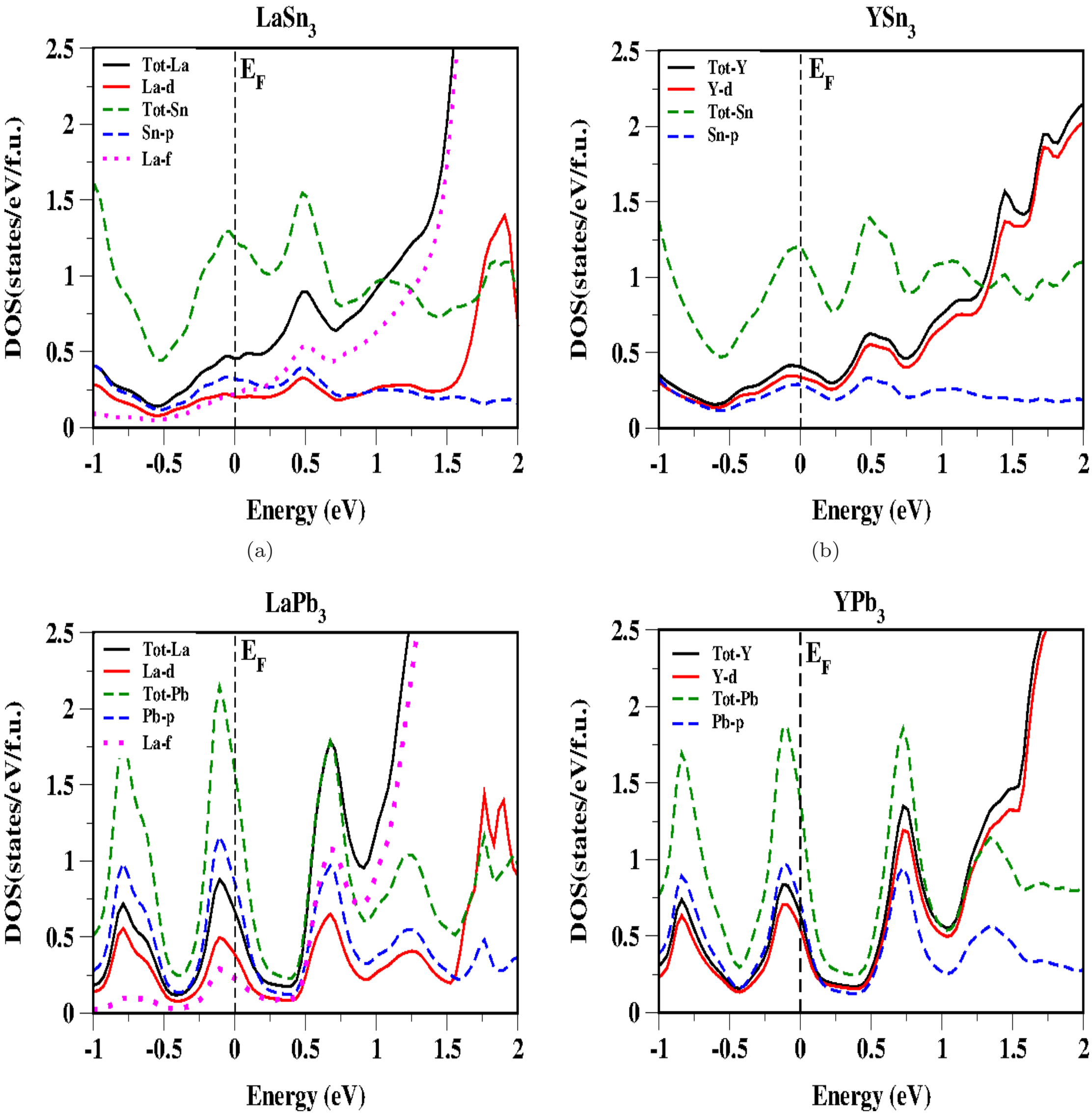

(a) (b)

(c) (d)

Figure 3.5: Density of states of AX$_3$ (A = La, Y; X = Sn, Pb) as calculated at the experimental lattice constants. (a, c) the total atomic DOS as well as La '*d*', Sn '*p*', Pb '*p*' and La '4*f*' partial contributions are shown, (b, d) the total atomic DOS as well as Y '*d*', Sn '*p*' and Pb '*p*' partial contributions are shown. The unit is states per *eV* per formula unit (f.u.).

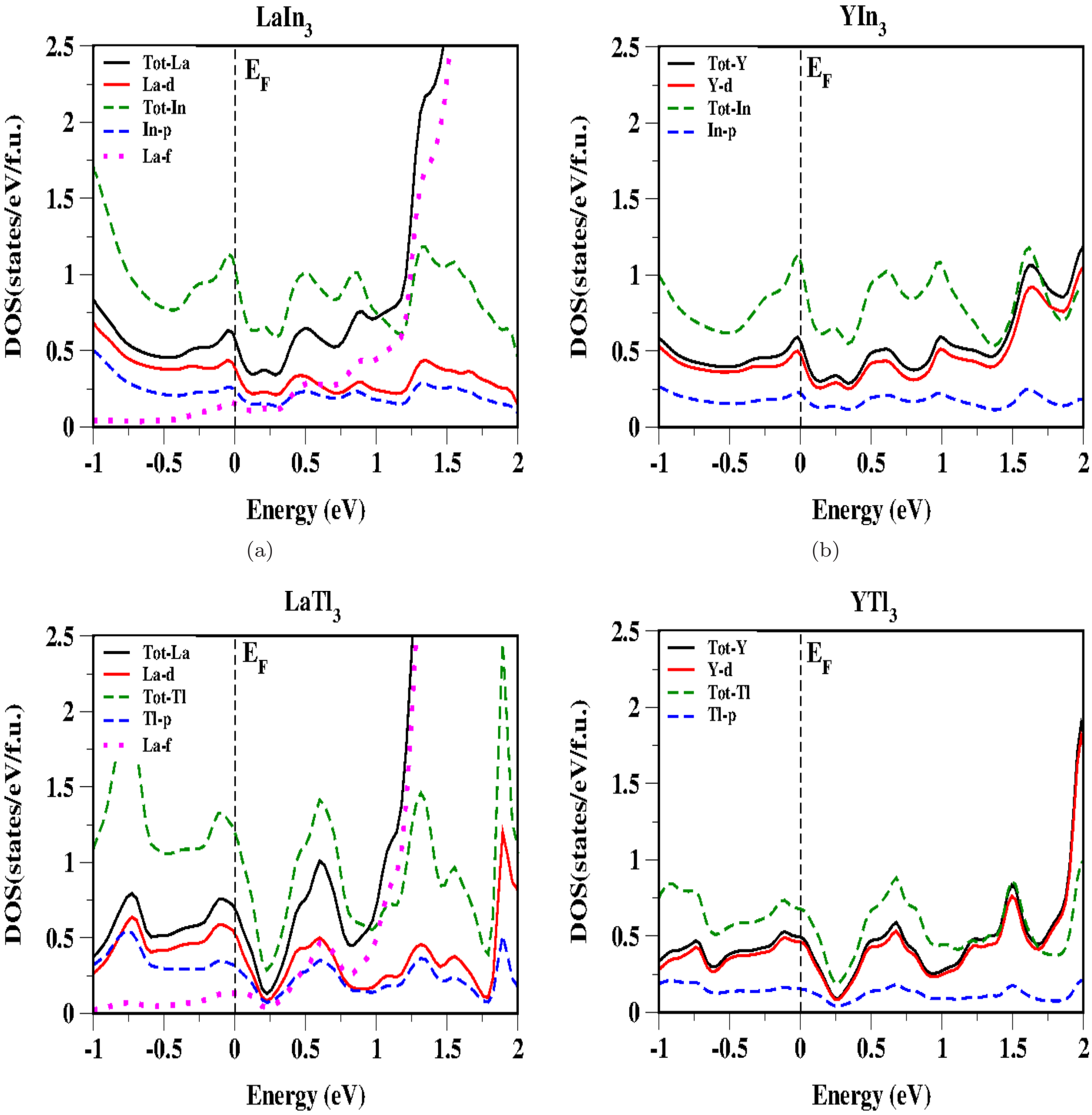

(a) (b) (c) (d)

Figure 3.6: Density of states of AX_3 (A = La, Y; X = In, Tl) as calculated at the experimental lattice constants. (a, c) the total atomic DOS as well as La '*d*', In '*p*', Tl '*p*' and La '4*f*' partial contributions are shown, (b, d) the total atomic DOS as well as Y '*d*', In '*p*' and Tl '*p*' partial contributions are shown. The unit is states per *eV* per formula unit (f.u.).

But the topology of YSn_3 is slightly different, where (at ambient pressure) it has an extra electron pocket along the Δ line, which for $LaSn_3$ only appears under compression. As we discussed earlier, the difference among Pb and Sn containing compounds is seen particularly at the X and M points in the BZ, as can be seen from the complicated FS in Fig. 3.7 (b), (d), for Sn containing compounds and in Fig. 3.8 (b, d) for Pb containing compounds. It is interesting to note that the topologies of the Fermi surfaces of the Sn, Pb containing compounds are completely different from the topology of In, Tl containing compounds. Now, when we compare AIn_3 with ATl_3, we observe the nearly similar electronic structure in the vicinity of the Fermi level, except for points along the Λ and S symmetry lines as discussed earlier, resulting in the hollow triangular tubes interconnected along S line in AIn_3 (see Fig. 3.9 (a, c)) and an open gap is not seen along the Λ line in ATl_3 (see Fig. 3.10 (a, c)). Our calculated FS of $LaIn_3$ is also quite similar to the earlier study [54]. Apart from this, we find the FS topology of $LaIn_3$ and YIn_3 to be the same at zero pressure, as is also evident from the band structure plots in Fig. 3.3.

Under compression Fermi surface topology changes are found in all the compounds apart from YSn_3 and YPb_3. The most striking change in the FS of $LaSn_3$ under pressure is the appearance of the third surface, already seen in YSn_3 at ambient conditions (Fig. 3.7 (e)). This appears at a compression of $V/V_0 = 0.94$ (corresponding pressure equivalent to 1 GPa), as shown in Fig. 3.11 (a). A second, less drastic change occurs in the second Fermi surface of $LaSn_3$, where the hole pocket around the X point, increases and merges with the surrounding triangular hole regions as evident from Fig. 3.11 (b). In contrast, for $V = V_0$, Fig. 3.7 (b), this pocket is detached from the larger hole region, facilitating a small closed electron orbit. At the same time, the electron concentration around the M point (the midpoints of all edges of the BZ) increases under compression, which eventually leads to the connection of all electron pockets. This happens around $V/V_0 = 0.90$ (see Fig. 3.11 (b) and the pressure nearly equals to 4 GPa). Altogether, under compression the electron concentration at M and the hole concentration at X increase simultaneously in $LaSn_3$ and is also evident from the band structure plots in Fig. 3.12 (a), (b). In the case of YSn_3 only the electron concentration at the M point increases, while there is no hole pocket at X even at ambient volume, and therefore the Fermi surface topology of YSn_3 remains unchanged under (modest) compression. In $LaPb_3$ a new hole pocket appears at the X point for a compression V/V_0=0.90 (corresponding to an applied pressure around 8 GPa), as shown in Fig. 3.11 (c). This is also seen from the band structure plot in Fig. 3.12 (c, d). This is mainly due to the upward movement of the band only at the X point irrespective of the other points in the BZ, where the simultaneous downward shifts of the band is

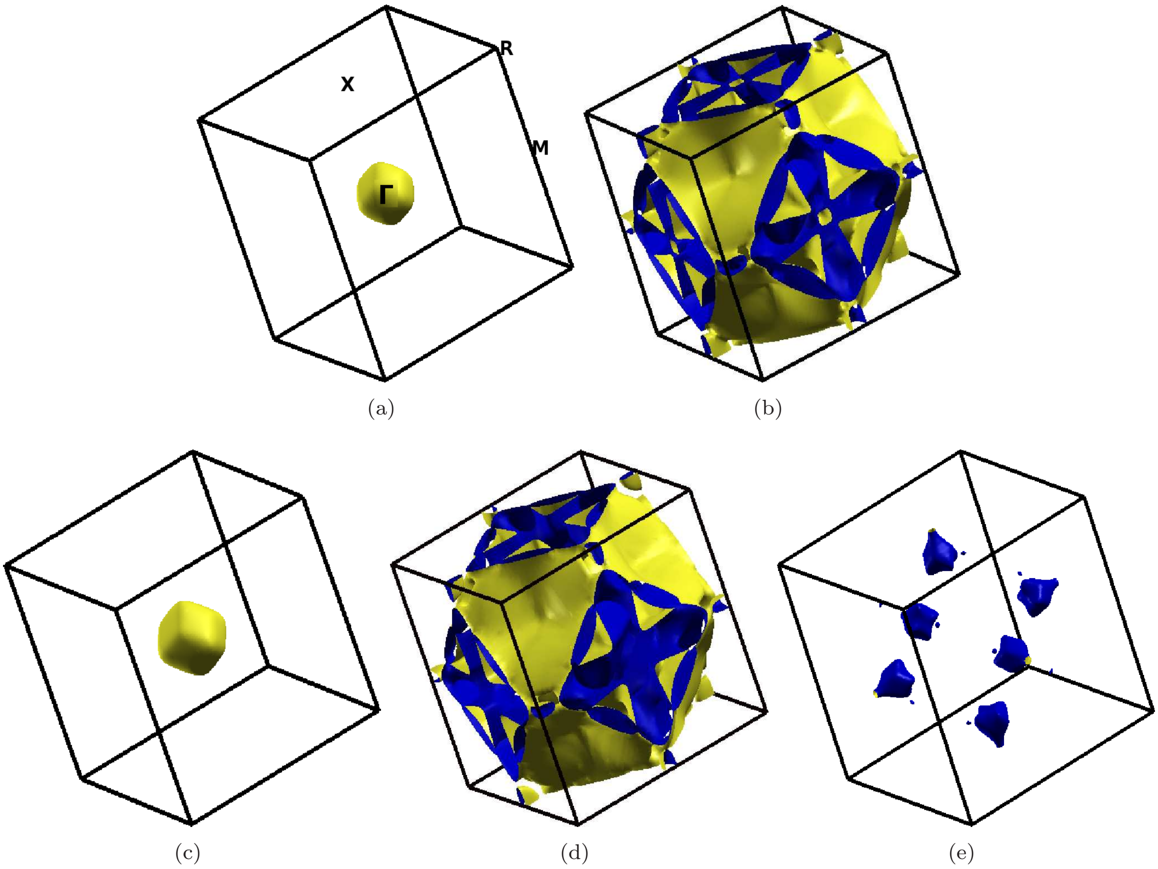

(a) (b)

(c) (d) (e)

Figure 3.7: Fermi surface at zero pressure of (a, b) $LaSn_3$ and (c-e) YSn_3 at experimental lattice constants. The second FS of $LaSn_3$ and YSn_3 is different. YSn_3 has an extra Fermi surface (Fig. (e)). The two different color is only to distinguish the outer and the inner region of the FS throughout the thesis.

found under pressure, the same hole pocket is also found in $LaSn_3$ at ambient pressure. But no such topology change is seen in YPb_3 similar to YSn_3, although they have the same band structure as $LaPb_3$ around E_F at ambient pressure (see Figs. 3.2 (c) and (d)). This could be due to the band being more dispersive in YPb_3, especially at the X point as can be seen in Fig. 3.2 (d) (red, dashed line), and of Y 'd' character at that particular point. Under pressure, the FS topologies of $LaSn_3$ and $LaPb_3$ are nearly identical, and this indicates that $LaPb_3$ and $LaSn_3$ could behave alike under compression. As noted by Havinga et al. [82] the variation of T_c is quite regular for $La(Pb_{1-x}Sn_x)_3$ alloys where the valence electron concentration remains the same, which may also support our result. The FS topology remains unchanged for the other simple hole pocket (see Fig. 3.7 (a, c) and Fig. 3.8 (a, c), blue colour, dotted line band in Figs. 3.2 (a-d) under compression. Comparing AIn_3 and ATl_3 under compression near $V/V_0 = 0.98$ (pressure around 1.5 GPa) a FS topology change is observed in AIn_3 due to a downward shift of the band along the Σ line which is mainly of In 'p'

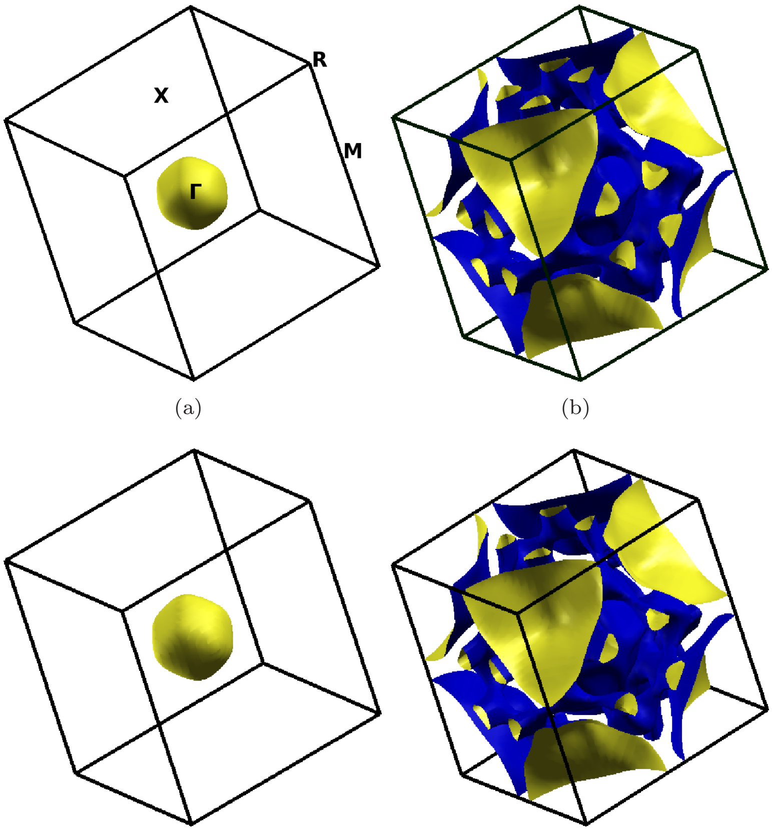

(a) (b)

(c) (d)

Figure 3.8: Fermi surface at zero pressure of (a, b) $LaPb_3$ (c, d) YPb_3 at experimental lattice constants. The topology of the Fermi surface of LaX_3 is similar to that of YX_3 for X = Pb. The topology of the first sheet for ASn_3 is similar to that of APb_3.

character, resulting in the interconnected triangular open tubes becoming disconnected along the same Σ line, as is evident from Fig. 3.11 (d). In the case of ATl_3 a FS topology change is found near $V/V_0 = 0.80$ (corresponding to a pressure in excess of 18 *GPa*) and is illustrated from Fig. 3.11 (e). Under compression, the downward shift of the band is seen along the Σ line, as in AIn_3, with a simultaneous upward movement of the band along the S line. Owing to this, the triangular open regions open up along S, with simultaneous partial detachment of the same open tube along Σ, and the band character is mainly Tl '*p*'-like. The same simultaneous upward shift of the band is also observed in AIn_3 along S, but it does not alter the vicinity of E_F in that particular direction. Under compression, the FS topology of ATl_3 is quite similar to AIn_3. The topology of the second surface remains the same for all In and Tl containing compounds at ambient as well as at higher compressions (see Fig. 3.9 (b, d) and 3.10 (b, d), blue colour dotted line band in Fig. 3.3 (a-d)). Under compression, the topology of $LaPb_3$ looks like $LaSn_3$, and similarly the topology of AIn_3

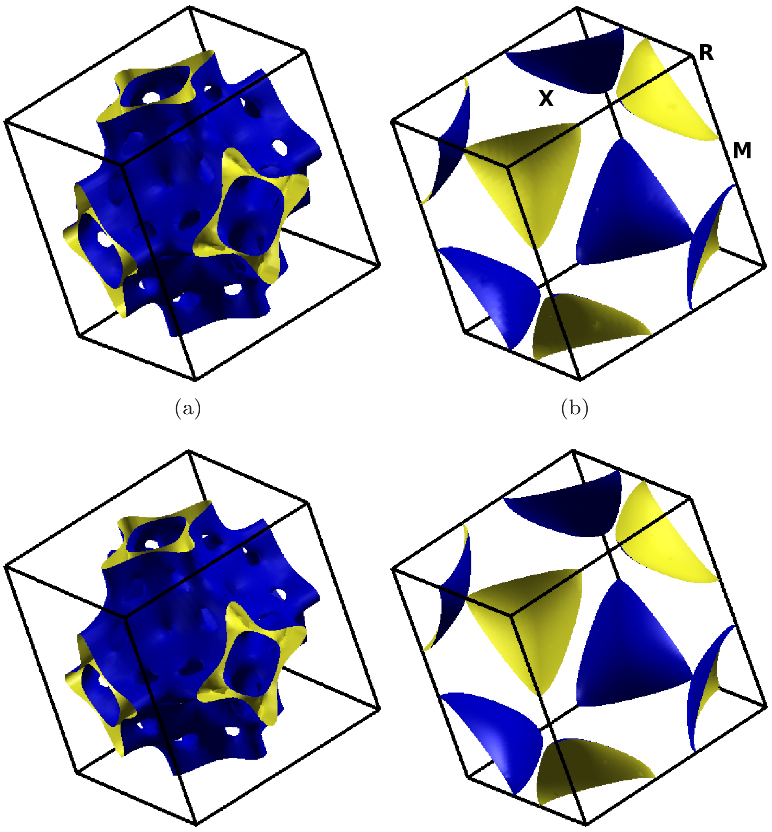

(a) (b)

(c) (d)

Figure 3.9: Fermi surface at zero pressure of (a, b) $LaIn_3$ and (c, d) YIn_3 at experimental lattice constants. The topology of the Fermi surface of LaX_3 is similar to that of YX_3 for X = In.

looks like ATl_3.

The evolution of the total density of states at the Fermi level for the AX_3 compounds under compression is shown in Fig. 3.13. The behaviour is largely monotonically decreasing, with minor irregularities, which maybe related to Fermi surface topology changes under compression. The occurrence of a third Fermi surface sheet for $LaSn_3$ under pressure leads to an increase of the density of states at the Fermi level, as illustrated in Fig. 3.13. Similarly for the rest of the compounds we have also seen the non-monotonic variation of the density of states under pressure, where we have seen the Fermi surface topology change, except for YSn_3 and YPb_3 where it is seen to decrease monotonously under pressure and for both these compounds, we have also not found any Fermi surface topology change. These results for $LaSn_3$ are in accordance with the zero-pressure measurements of the superconducting transition temperature in the (La,Th)Sn_3 alloy system as investigated by Havinga et. al [137]. These authors also speculated that their observed oscillatory behaviour of T_c versus

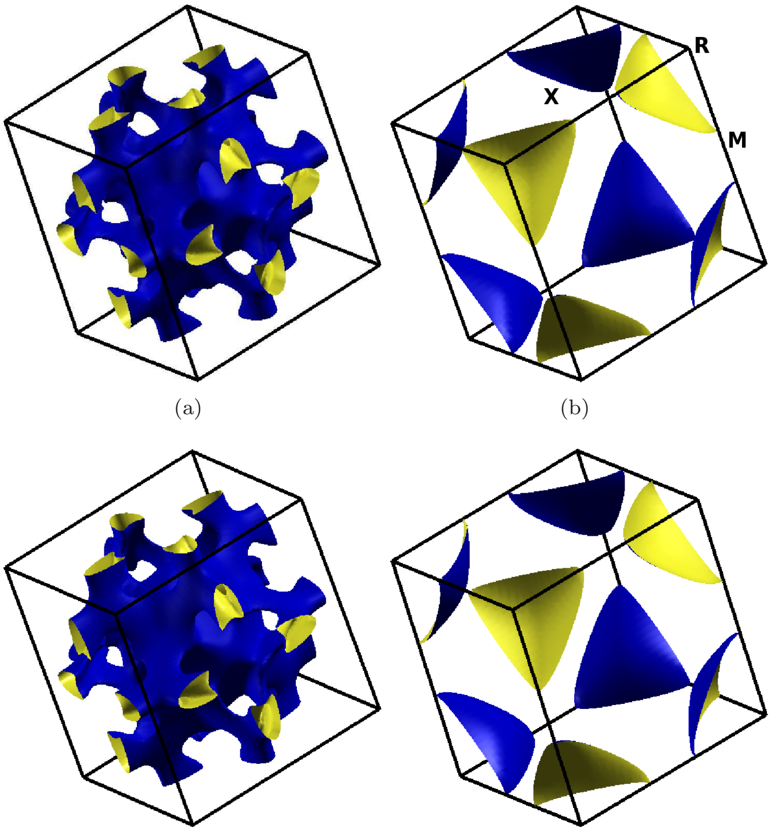

(a) (b)

(c) (d)

Figure 3.10: Fermi surface at zero pressure of (a, b) $LaTl_3$, (c, d) YTl_3 at experimental lattice constants. The topology of the Fermi surface of LaX_3 is similar to that of YX_3 for X = Tl. The topology of the second sheet for AIn_3 is similar to that of ATl_3.

alloy composition might be due to a singular behaviour of the electronic density of states in the vicinity of the Fermi level of $LaSn_3$. Within the BCS framework of superconductivity, the change in T_c observed could reflect a change in the density of states at the Fermi level. Hence the non-monotonic behaviour of density of states observed in AX_3 compounds except for YX_3 (X = Sn, Pb) could be further reflected in the T_c variation which is taken up elaborately in chapter-5.

3.3.4 Elastic constants and mechanical properties

The elastic constants have been calculated within the total-energy method, see Table-3.2. A cubic crystal has only three independent elastic constants [123, 124] C_{11}, C_{12} and C_{44}. To the best of our knowledge, no experimental values on the elastic constants of these compounds have been reported to date, except in $LaSn_3$. The elastic constants extracted from the experimental phonon dispersion curves [131] for $LaSn_3$ are listed for comparison. All the investigated compounds are

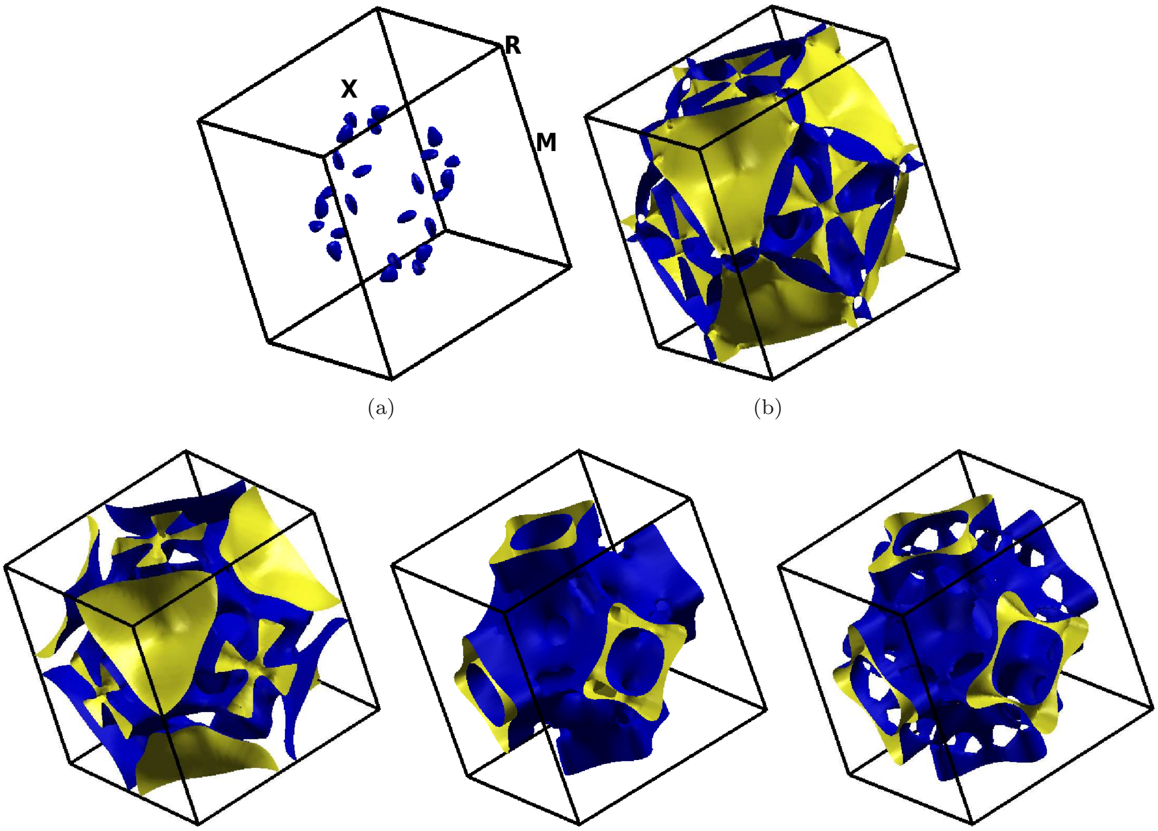

(a) (b)

(c) (d) (e)

Figure 3.11: Fermi surface of $\mathrm{LaSn_3}$ (a) at $\mathrm{V/V_0}$=0.94 (an extra new pocket appeared), (b) at $\mathrm{V/V_0}$=0.90, (c) Fermi surface of $\mathrm{LaPb_3}$ at $\mathrm{V/V_0} = 0.90$, (d) $\mathrm{LaIn_3}$ at $\mathrm{V/V_0} = 0.98$, (e) $\mathrm{LaTl_3}$ at $\mathrm{V/V_0} = 0.80$. $\mathrm{V_0}$ denotes the experimental equilibrium volume.

mechanically stable and satisfy the stability criteria for the cubic system, i.e. $C_{11} > C_{12}$, $C_{44} > 0$, and $C_{11} + 2C_{12} > 0$. From these, one may obtain the Hill's [126] shear modulus G_H by using the equation (3.1-3.3). Apart from this there is no structural phase transition known in the pressure range studied for all our investigated compounds, which is further confirmed from the phonon spectrum and is discussed in chapter-5. All the compounds are found to be ductile in nature according to Pugh's criterion [138] $G_H/B < 0.57$ as seen from the values of G_H/B in Table-3.2. Cauchy's pressure ($C_p = C_{12} - C_{44}$) is another index to determine the ductile/brittle nature of metallic compounds, where positive (negative) values correspond to ductile (brittle) materials. The calculated Cauchy pressures for the compounds considered here are all positive, i.e. also indicating a ductile nature. Poisson's ratio σ (see Table-3.2) is another important parameter for describing the ductile nature of solids. σ is typically around 0.33 [139] for the ductile materials. Thus from the calculated values of σ, the ductility of these compounds is again confirmed. Another important

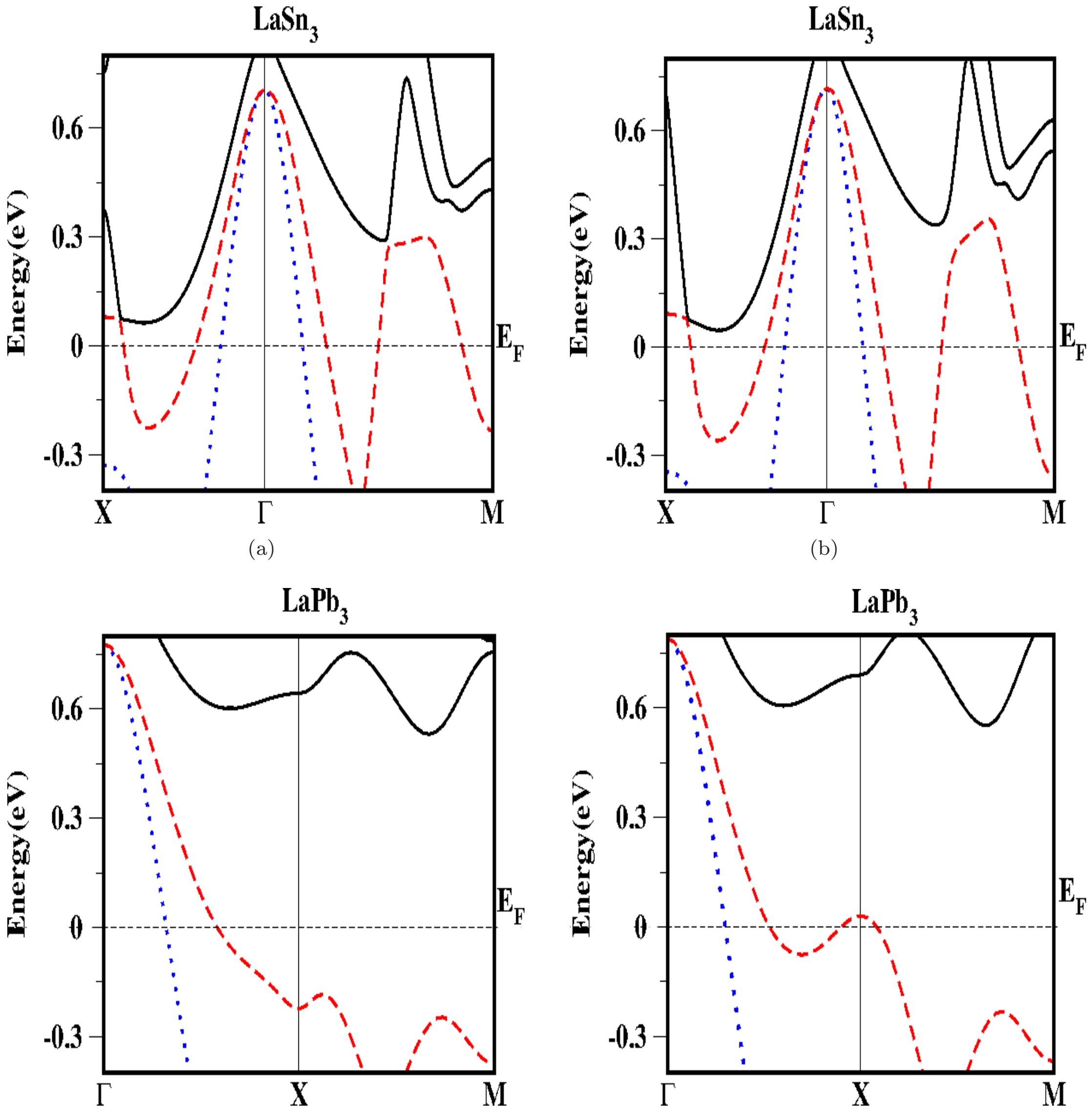

(a) (b)

(c) (d)

Figure 3.12: Band structure of LaSn$_3$ under compression (a) at V/V$_0$ = 1.0 and (b) at V/V$_0$ = 0.9 (zoom-in on the vicinity of the Fermi level). The electron pocket at M and the hole pocket at X increases under compression. Band structure of LaPb$_3$ (c) at V/V$_0$ = 1.0 and (d) at V/V$_0$ = 0.90, a new hole pocket is emerging at the X point.

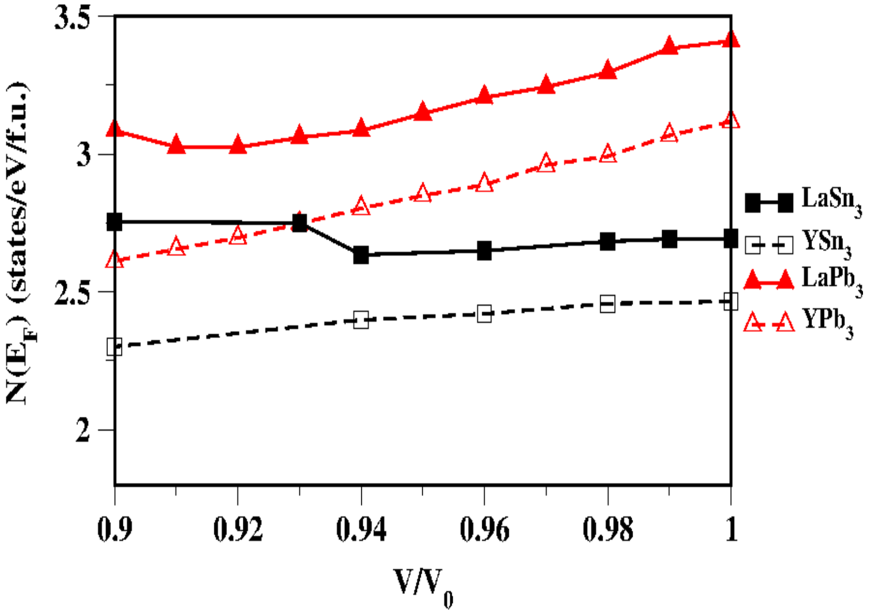

(a)

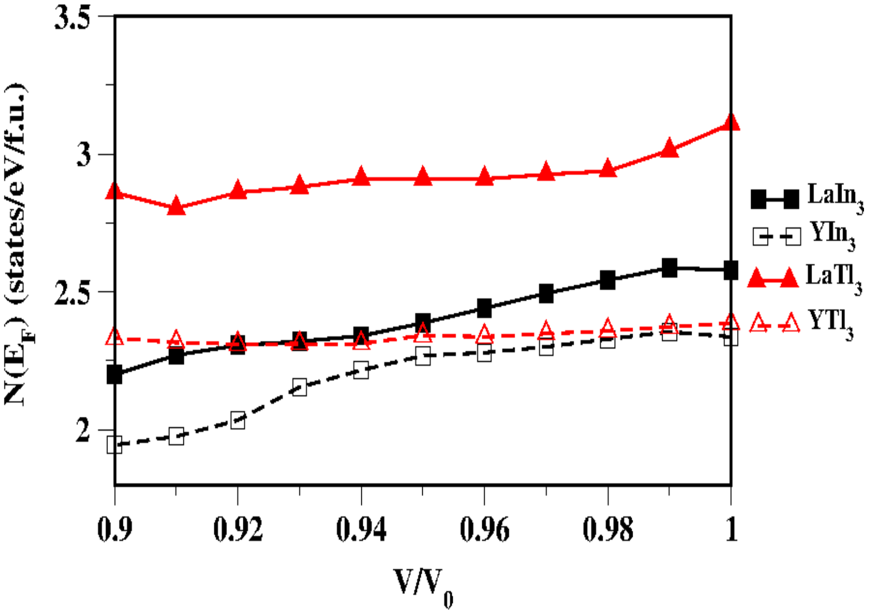

(b)

Figure 3.13: Variation of the density of states at the Fermi level, $N(E_F)$, under compression, (a) for AX$_3$ (A = La, Y; X = Sn, Pb) and (b) for (A = La, Y; X = In, Tl). The unit of the density of states is states per eV per formula unit (f.u.).

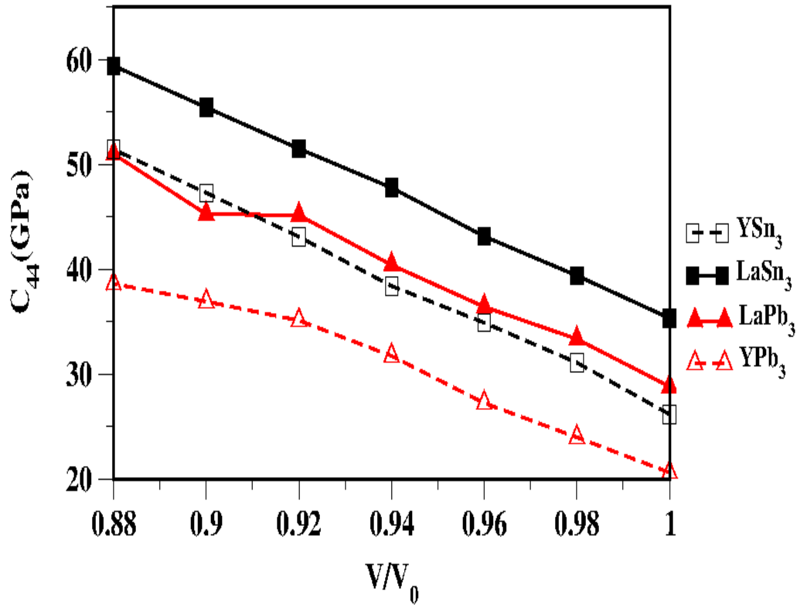

(a)

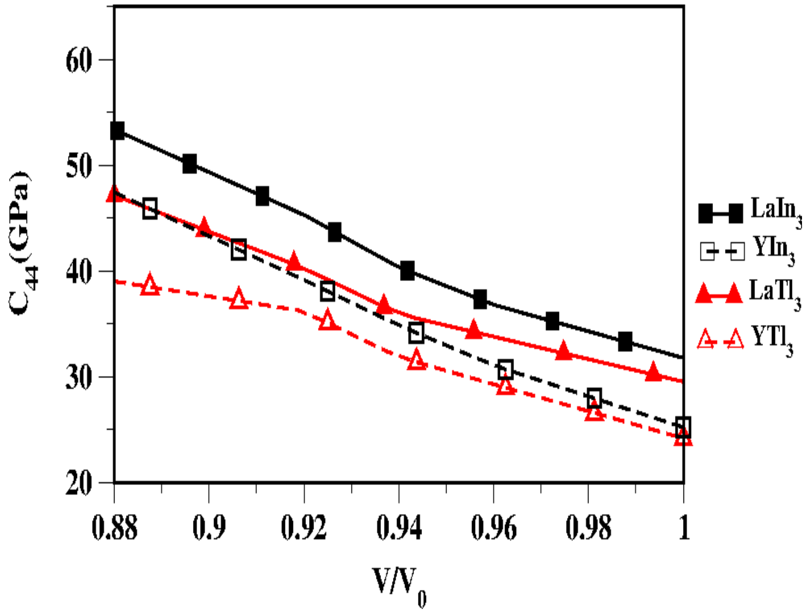

(b)

Figure 3.14: Variation of the C_{44} elastic constant with compression in AX$_3$ compounds (a) for A = La, Y with X = Sn, Pb, (b) for A = La, Y with X = In, Tl.

parameter is the elastic anisotropy factor, A, which gives a measure of the anisotropy in the crystal. For isotropic crystals $A = 1$, while values smaller or greater than unity measure the degree of elastic anisotropy. All our investigated compounds are elastically anisotropic in nature, with $\mathrm{YPb_3}$ being most anisotropic among all the compounds as seen from the Table-3.2. Having calculated Young's modulus E, the bulk modulus B, and the shear modulus G_H, one may derive the Debye temperature using the equation (3.7) as explained above and our calculated values of Debye temperature along with the transverse and longitudinal velocities are also reported in Table-3.2. Apart from this we also calculated the elastic constants for the $\mathrm{AX_3}$ compounds under compression, as shown in Fig. 3.14. An elastic softening is found in C_{44} for $\mathrm{LaPb_3}$ near $\mathrm{V/V_0} = 0.9$ (pressure around 8 GPa). This might be related to the new hole pocket appearing at the X point at this compression of $\mathrm{LaPb_3}$.

Table 3.2: Elastic constants and derived quantities for AX_3 (A = La, Y; X = Sn, Pb, In, Tl), at theoretical equilibrium volume. A is the anisotropy factor, $A = 2C_{44}/(C_{11} - C_{12})$, B is the bulk modulus and $C_p = C_{12} - C_{44}$ is the Cauchy pressure.

Parameters	$LaSn_3$	$LaPb_3$	$LaIn_3$	$LaTl_3$	YSn_3	YPb_3	YIn_3	YTl_3
C_{11} (GPa)	97.3	83.5	103.9	90.6	82.3	70.0	106.2	93.0
	70.5^a							
C_{12} (GPa)	53.6	50.5	44.5	46.4	64. 6	59.5	48.7	53.6
	42.0^a							
C_{44} (GPa)	44.2	35.8	37.7	31.6	34.2	28.0	33.6	30.4
	33.5^a							
A	2.02	2.17	1.27	1.43	3.85	5.3	1.17	1.54
G_H (GPa)	33.3	26.2	34.3	27.4	20.0	14.6	31.6	25.6
B	68	62	64	62	71	63	70	66
E (GPa)	85.9,64^b	68.9	87.3	71.5	54.9	40.7	81.9	68.0
σ	0.29	0.31	0.27	0.30	0.37	0.39	0.30	0.33
G_H/B	0.49	0.43	0.53	0.45	0.28	0.23	0.46	0.38
C_p (GPa)	9.4	14.7	6.8	14.7	30.3	31.5	15.1	23.2
v_l (km/s)	3.77	2.94	3.72	2.89	3.59	2.75	3.75	2.92
v_t (km/s)	2.05	1.53	2.08	1.53	1.63	1.16	2.0	1.47
Θ_D (K)	230	167.6	234.80	170.5	129.8	188.4	234.9	168.7
	205^c	147^d	$170,^d$ 194.4^e		210^f			

a: From phonon measurements, Ref. [131]; b: Ref. [140]; c: Ref. [141]
d: Ref. [142]; e: Ref. [143] (Expt.: From specific-heat measurements). f: Ref. [80].

3.4 Conclusion

An *ab initio* study of the intermetallic compounds $\mathrm{LaX_3}$ and $\mathrm{YX_3}$ was performed within the local density approximation. The Fermi surface topology change under compression is observed for all the investigated isostructural compounds $\mathrm{AX_3}$ (A = La, Y; X = Sn, Pb, In, Tl) except in $\mathrm{YSn_3}$ and $\mathrm{YPb_3}$. The calculated elastic constants and the related mechanical properties confirmed the ductility of all the $\mathrm{AX_3}$ compounds. A Fermi surface topology change is observed in $\mathrm{LaSn_3}$ at a compression of around $V/V_0 \sim 0.94$, where a third Fermi sheet occurs and around $V/V_0 \sim 0.90$, the X point gets connected to the remaining surface, and this might be due to the SOC together with the 'f' hybridizing effect. In addition we found an elastic softening of C_{44} under pressure only in $\mathrm{LaPb_3}$, which might be related to the appearance of a new hole pocket at the X point. The density of states near to the Fermi level are mainly X 'p'-like states in all compounds with admixture of the A 'd' states and La 'f' like states.

Chapter 4

Comparative study of La_3X and LaX_3 compounds

The effect of compression on the electronic structure and Fermi surface (FS) topology of La rich La_3X (X =In, Tl, Sn) compounds is studied and compared with X rich LaX_3 compounds based on density functional theory calculations. All the La rich compounds are found to have high density of states at the Fermi level, dominated by the La '*d*' orbital contributions with small contributions from X '*p*' and La '*f*' states. This leads to almost identical Fermi surfaces for the La_3X compounds. In contrast, the isostructural LaX_3 compounds have lower densities of states at the Fermi level, dominated by the X '*p*' states and their FS topologies vary with X. A strong interaction exists between the atoms in La_3X compounds, more pronounced than in the LaX_3 type compounds. This can be attributed to the local tetragonal and octahedral site symmetry of La in La_3X and LaX_3, respectively, causing a difference in the crystal field splitting of the '*d*' orbitals in the two cases, although the crystal structure is cubic in both the cases. Fermi surface topology changes under compression are found in all the investigated compounds in all the FS sheets for La_3X compounds, while for LaX_3 changes are seen only in the complicated FS sheet. The elastic constants and related mechanical properties of the La_3X compounds were calculated. From the calculated values of elastic constants, all the investigated compounds are found to be of ductile nature with elastic anisotropy. The mechanical properties of all La_3X and LaX_3 compounds are found to be similar, although their electronic structures and Fermi surface topologies are different.

4.1 Introduction

La_3X compounds with X = Sn, In and Tl crystallize in the cubic Cu_3Au-type structure with space group $Pm\bar{3}m$ (no. 221). These compounds are well known superconductors with higher [63, 144, 65, 64] superconducting transition temperatures (T_c) than found in the isostructural LaX_3 family [82, 49, 129]. Superconductivity, magnetic and thermodynamic properties of La_3Tl were determined experimentally by Bucher et. al [145]. The compounds La_3In and La_3Tl have been identified as strong-coupling superconductors [63]. Theoretically, the electronic structure and cohesive properties of La_3In have been reported [133], while Ravindran et. al [69] studied the structural stability, electronic properties and superconductivity of La_3X as well as La_3XC (X= Al, Ga, In, Tl) compounds. In this present chapter the elastic and mechanical properties for the La_3X compounds (X = Sn, In, Tl) are presented and their Fermi surfaces are calculated and pressure-induced topology changes identified. The results will be compared to those of the isostructural LaX_3 compounds, which have been studied extensively [113, 133, 54, 132, 118]. The remainder of this chapter is organized as follows: in section-4.2, details of the computations are presented, results and discussions presented, in section-4.3, while section-4.4 concludes the chapter.

4.2 Method of calculation

The electronic structure calculations were performed using the full-potential linearized augmented plane wave (FP-LAPW) method as implemented in the WIEN2*k* code [101] based on the generalized gradient approximation of Perdew, Burke and Ernzerhof [98]. For the total energy convergence R_{MT} K_{max}= 8.5 was used, where R_{MT} is the smallest muffin-tin radius, and K_{max} is the plane wave cut-off. The charge density was Fourier expanded up to G_{max} = 9 a.u.$^{-1}$ and the muffin-tin radii were chosen as 2.75 a.u for La and 2.5 a.u for the X atoms. We carried out convergence tests for the charge-density Fourier expansion using higher G_{max} values and found no significant changes in the calculated properties. A (32 × 32 × 32) k-point mesh in the Monkhorst-Pack [120] scheme was used during the self consistent cycle. The total energy was converged up to 10^{-6} Ry. A (44 × 44 × 44) mesh corresponding to 2300 k-points in the irreducible part of Brillouin zone was used for the Fermi surface calculations to ensure accurate determination of the Fermi level. The three dimensional (3D) Fermi surface plots were generated with the help of the XCrySDen ((*X*-Window) CRYstalline Structures and DENsities) molecular structure visualization program [122]. Spin-orbit coupling (SOC) is included for all the electronic structure calculations. We have used the experimental lattice constant of 5.07 Å, 5.06 Å, and 5.10 Å, for La_3In (Ref. [63]), La_3Tl (Ref. [63]) and La_3Sn (Ref. [64]), respectively, and the corresponding experimental volumes are denoted by V_0 in the following.

For the calculation of the elastic constant and the related mechanical properties we have used the formulas as given in the previous chapter (chapter-3). In addition, we have also calculated the Debye temperature from the mean sound velocity, which is the arithmetic mean of the longitudinal and the transverse sound velocities and the corresponding relations are reported again in chapter-3 and the related references are found therein.

4.3 Results and discussions

4.3.1 Structural properties

La_3X and LaX_3 compounds crystallize in the simple cubic structure with space group $Pm\bar{3}m$ (no. 221). In La_3X, the La atom occupies the crystallographic position (0.0, 0.5, 0.5) with tetragonal point group symmetry D_{4h}, while the X atom occupies the crystallographic position (0.0, 0.0, 0.0) with octahedral point group symmetry O_h. For the LaX_3 compounds, the La and X positions are interchanged, i.e. La is having O_h point group symmetry with position (0.0, 0.0, 0.0) and X is having D_{4h} point group symmetry with position parameter (0.0, 0.5, 0.5). The local La symmetry in La_3X and LaX_3 compounds is illustrated in Fig. 4.1. The difference in symmetry of the La sites in La_3X and LaX_3 induces a different splitting of the La '*d*' orbitals as discussed in the next sub-section.

4.3.2 Band structure and density of states

The calculated band structures of La_3X (X = In, Tl, Sn) with (solid black line) and without (dotted red) spin orbit coupling are presented in Fig. 4.2. The effect of SOC is negligible near the Fermi level (E_F) for La_3In, whereas effects are seen in particular at the R and Γ points for La_3Tl (Fig. 4.3 (a)) and La_3Sn (Fig. 4.3 (b)), respectively. The lowest single band in the energy range -8 to -5 eV is mainly derived from the X '*s*' states, while the bunch of narrow unoccupied bands in the 1.5 to 3 eV above the Fermi level are La '*f*' states. The states just below the Fermi level, between -3 eV and 0 eV, are strongly hybridized admixtures of X '*p*' and La '*d*' states. The bands crossing the Fermi level represent non-bonding states, mainly of La '*d*' (d_{xz},d_{yz}) character. The density of states (DOS) and their contributions from different atoms and orbital characters of La_3X and

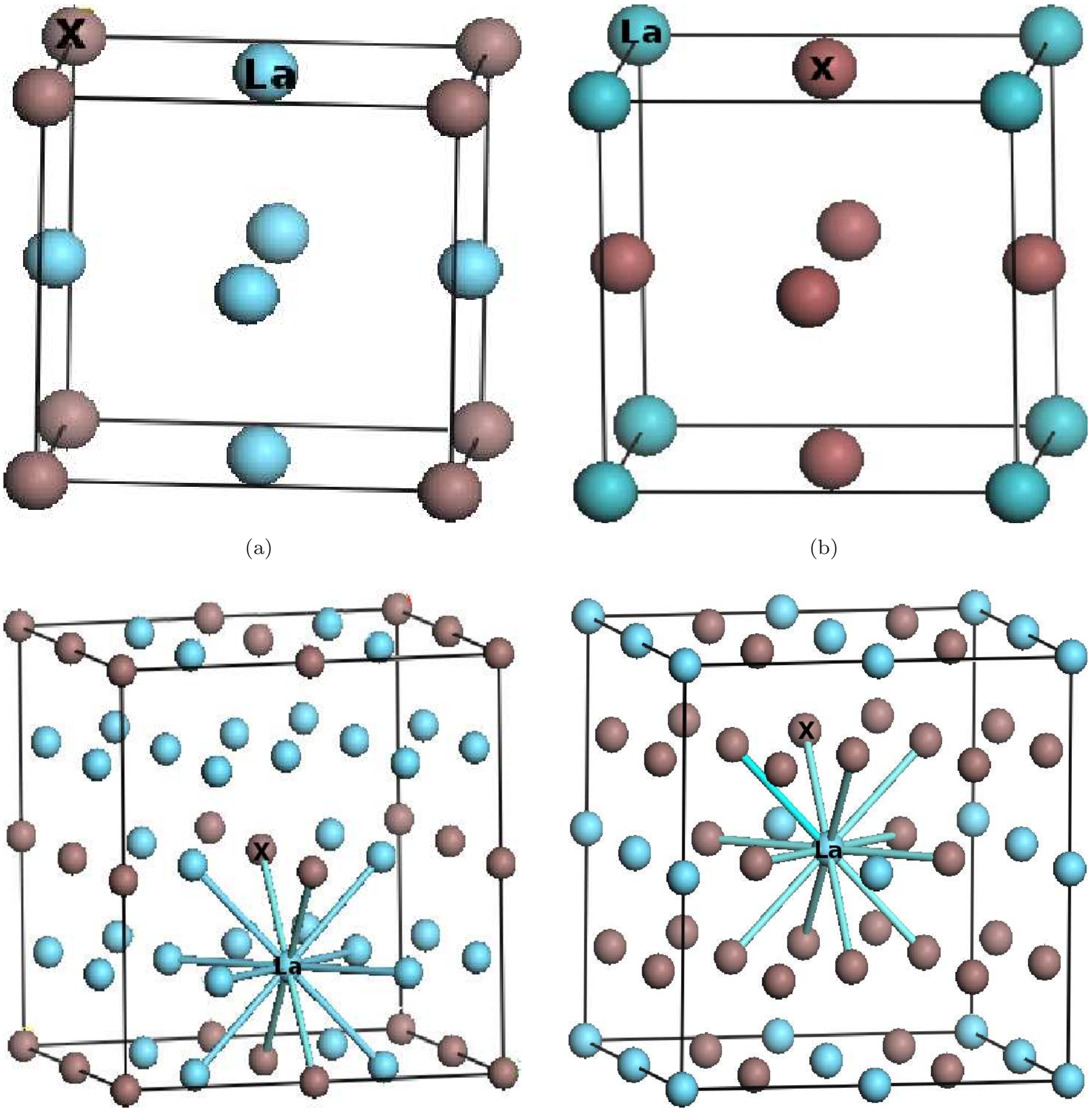

(a) (b)

(c) (d)

Figure 4.1: Unit cell for (a) La_3X and (b) LaX_3. The local environment of La in (c) La_3X and (d) LaX_3 is of D_{4h} and O_h symmetry, respectively. A 2×2×2 supercell is shown.

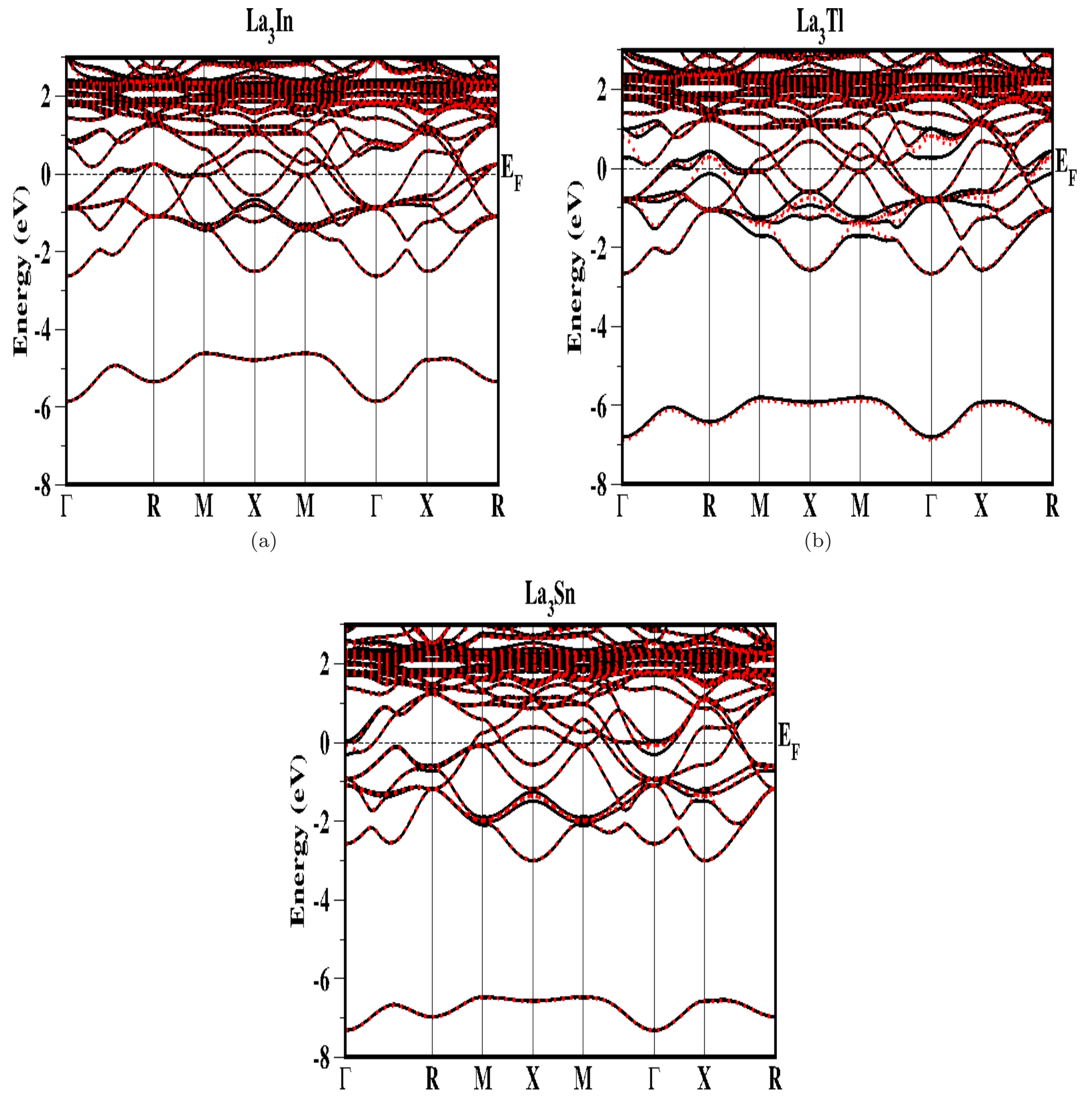

(a)

(b)

(c)

Figure 4.2: Band structure of La_3X (X = In, Tl, Sn) at the experimental lattice constants with and without spin-orbit coupling (SOC). The solid black (dotted red) lines show the bands with (without) SOC. In the vicinity of the Fermi level, the SOC effect is negligible for La_3In.

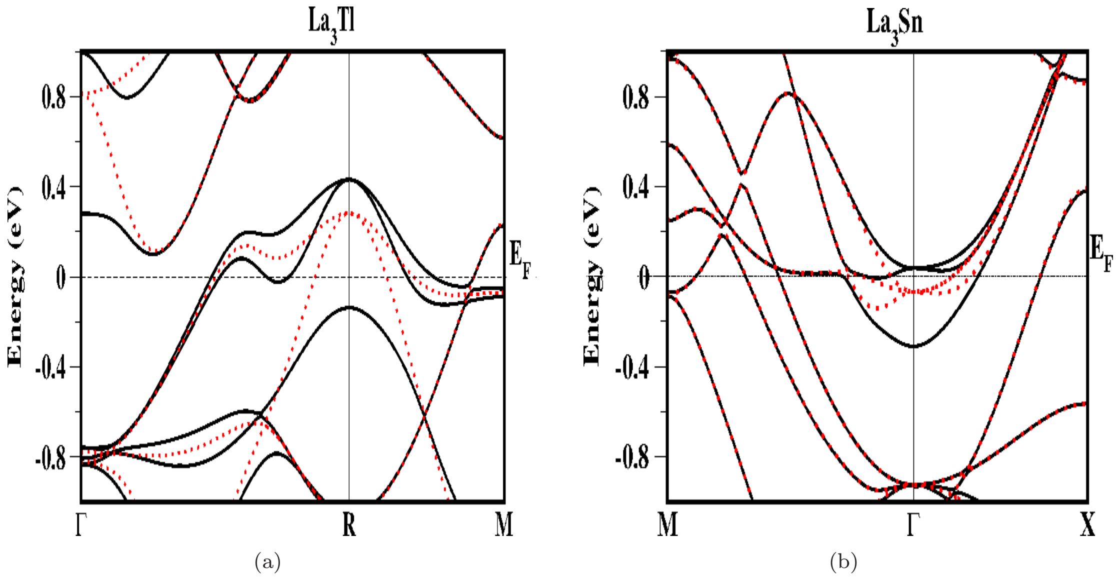

Figure 4.3: Zoomed band structure of (a) La$_3$Tl and (b) La$_3$Sn at the experimental lattice constants with and without spin-orbit coupling (SOC). The solid black (dotted red) lines show the bands with (without) SOC. In the vicinity of the Fermi level, the SOC effect is significant especially at the R and Γ points for La$_3$Tl and La$_3$Sn, respectively.

LaX$_3$ compounds are shown in Figs. 4.4-4.7. The total DOS functions for the three compounds are rather similar, although the X atoms are different and from different groups in the periodic table. A detailed analysis of La$_3$X compounds show that the highest peak in the antibonding region is dominated by the La 'f' and 'd' states, whereas the states in the bonding region just below E_F are hybridized La 'd' and X 'p' states (Fig. 4.4 (a-c)). At the Fermi level, the La 'd' (d_{xz},d_{yz}) orbitals dominate (see Fig. 4.6 (a-c)) with some admixture of X 'p' orbitals, and the La 'd' states spread out over the bonding and antibonding regions. For LaX$_3$ compounds, on the other hand, the DOS at E_F is dominated by X 'p' orbital with minor contribution from La 'd' (mainly $d_{t_{2g}}$ (see Fig. 4.7 (a-c)) states, and the admixture of La 'd' in the antibonding region is comparatively less, as shown in Fig. 4.5 (a-c).

All the La$_3$X compounds possess a pseudogap in the DOS on both sides of the Fermi level. This is an effect of the strong hybridization between La 'd' and X 'p' states, which causes the separation of the bonding and antibonding states through nonbonding states and formed pseudogap [146, 147, 148]. In the present case the strong 'p'-'d' hybridization gives rise to the pseudogap and separates the bonding and antibonding states through nonbonding states. The states in the lower energy region, which are mainly derived from the X 's' states (as shown in Fig. 4.4), do not take part in the bonding, and they are well separated from the bonding X 'p' and La 'd' hybridized states. In contrast to La_3X compounds, in LaX_3 compounds the bonding and antibonding states are separated only by a single pseudogap, and the nonbonding states are less distinct, which can be seen from Fig. 4.5 (a-c). This difference is mainly due to the splitting of the La 'd' orbital which is different in La_3X and LaX_3 compounds. As discussed in Fig. 4.1, the nearest neighbours of the La and X atoms in La_3X and LaX_3 are quite different although the co-ordination number is the same, resulting in different crystal field splitting of La 'd' states. In La_3X compounds doubly degenerate La 'd' (d_{xz},d_{yz}) together with triply degenerate X 'p' states dominate at E_F, whereas for LaX_3 compounds triply degenerate La 'd' (t_{2g}) and doubly degenerate X 'p_x', 'p_y' states dominate at E_F, as shown in Fig. 4.7 for the 'd' states.

Table 4.1: Calculated density of states at the Fermi level, $N(E_F)$ (in states per eV per formula unit, evaluated at the experimental equilibrium volumes), together with derived Sommerfeld coefficient of specific heat, γ, for La_3X (X= In, Tl, Sn).

Compounds		N(E_F)	γ (mJ/mole K^2)
La_3In	This work	7.80	18.40
	Expt.	6.0^a	$56.0(2.4)^a$
	Other theory^b	4.41	
La_3Tl	This work	6.87	16.2
	Expt.	5.35^a	$49.6(4.0)^a$
	Other theory^b	4.75	
La_3Sn	This work	6.29	14.83
	Expt.		

a: Ref. [63]; b: Ref. [69]

Comparing La_3X with LaX_3 for X= Tl and Sn, the pseudogap is found only on one side of E_F, and it is located above E_F in $LaTl_3$ (Fig. 4.5 (b)) and below E_F in $LaSn_3$ (Fig. 4.5 (c)), which is due to the band filling by one extra electron per Sn compared to Tl. A similar feature is somewhat weaker in the case of $LaIn_3$ as shown in Fig. 4.5 (a). In addition, the gap in the lower energy regime mainly reflecting the separation of X 's' and 'p' states is found only in $LaSn_3$ and $LaTl_3$, while these

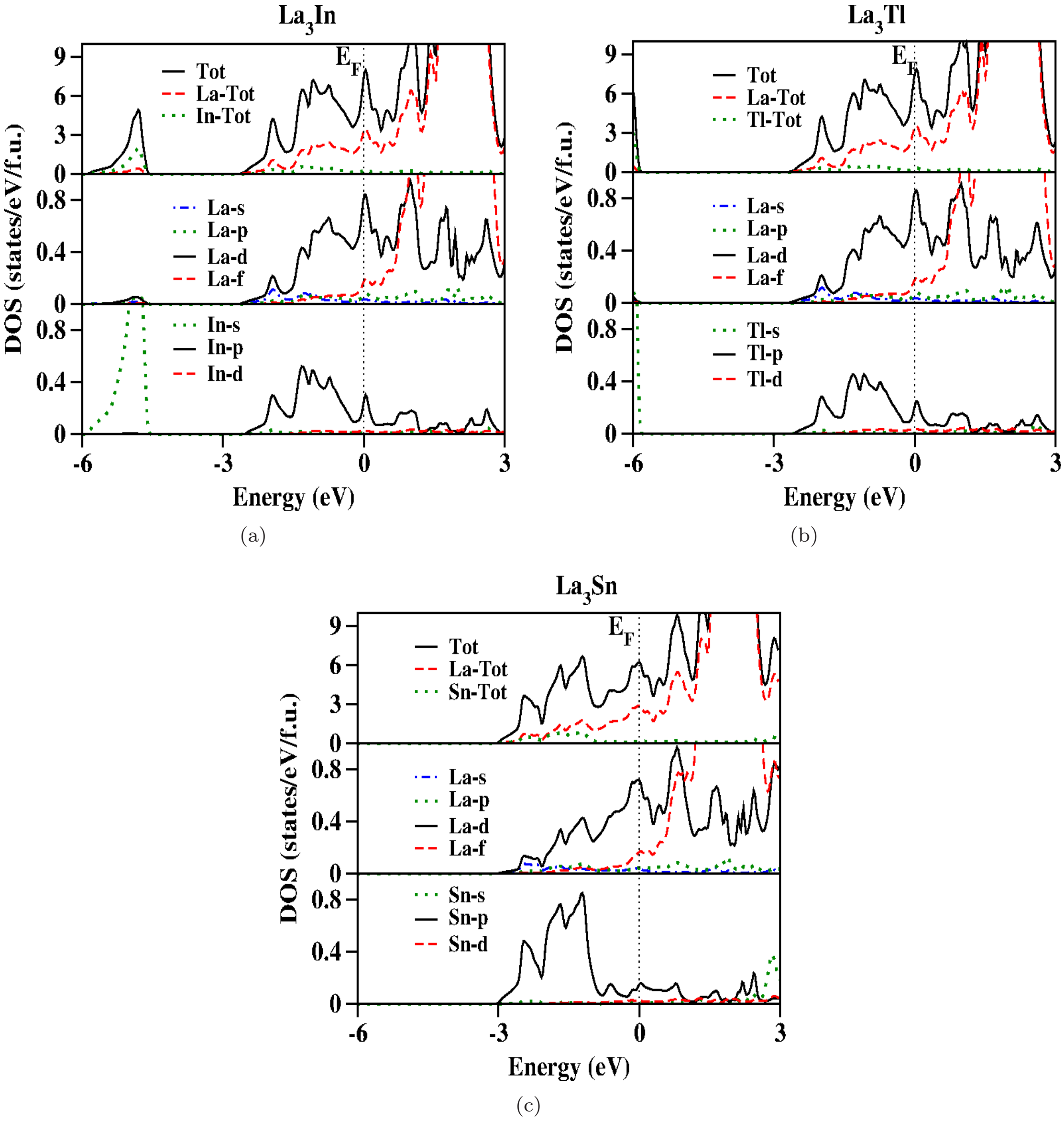

(a) (b)

(c)

Figure 4.4: Total and partial density of states of La$_3$X compounds (X = In, Tl, Sn) at experimental lattice constants and including spin-orbit coupling (SOC).

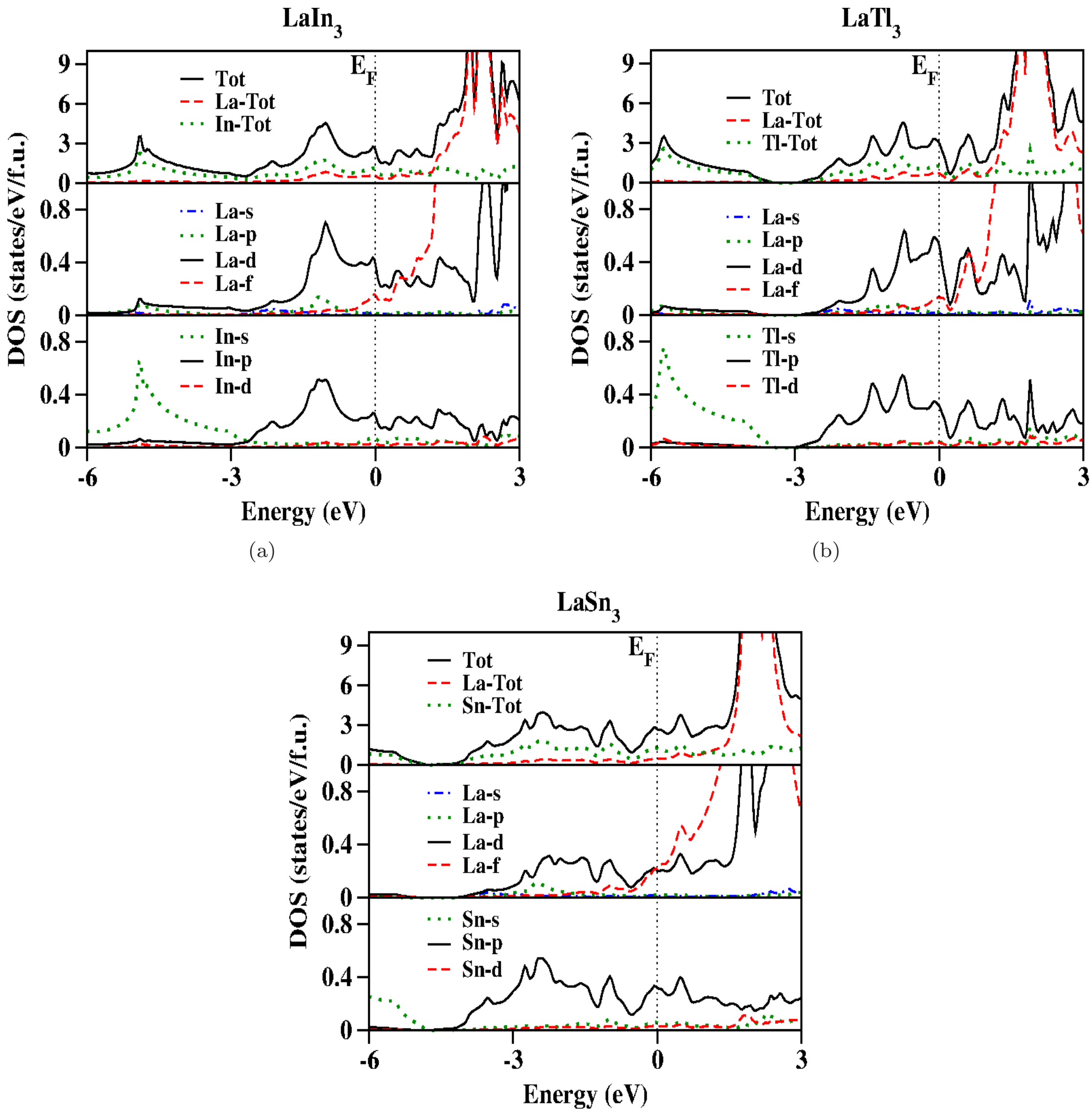

(a)

(b)

(c)

Figure 4.5: Total and partial density of states of LaX_3 compounds (X = In, Tl, Sn) at experimental lattice constants and including spin-orbit coupling (SOC).

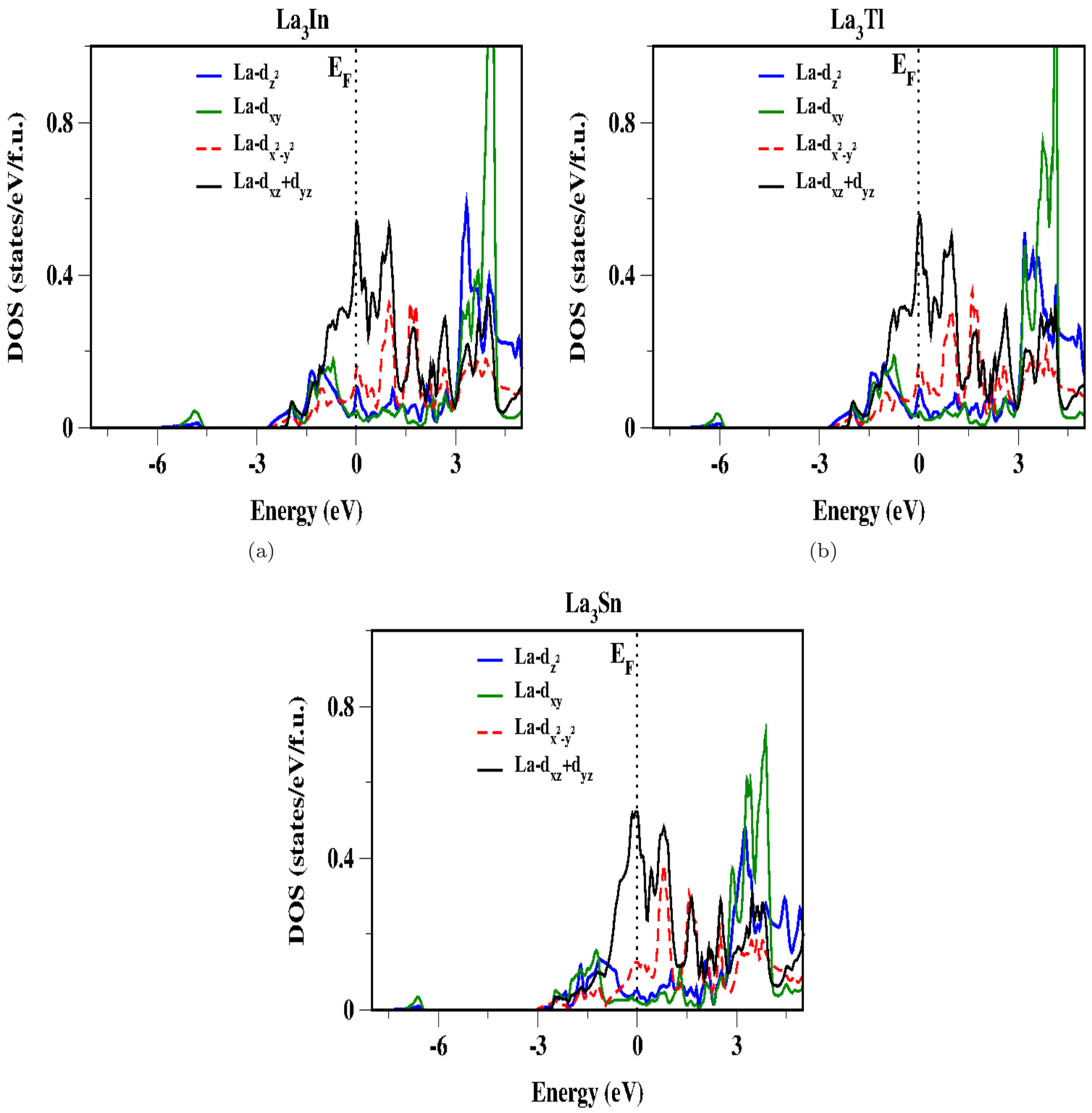

(a)

(b)

(c)

Figure 4.6: m-projected DOS of La 'd' states for La$_3$X with X = In, Tl, Sn, at the experimental lattice constants and including spin-orbit coupling (SOC). The contribution at E_F is mainly due to the La '$d_{xz,yz}$' orbital character.

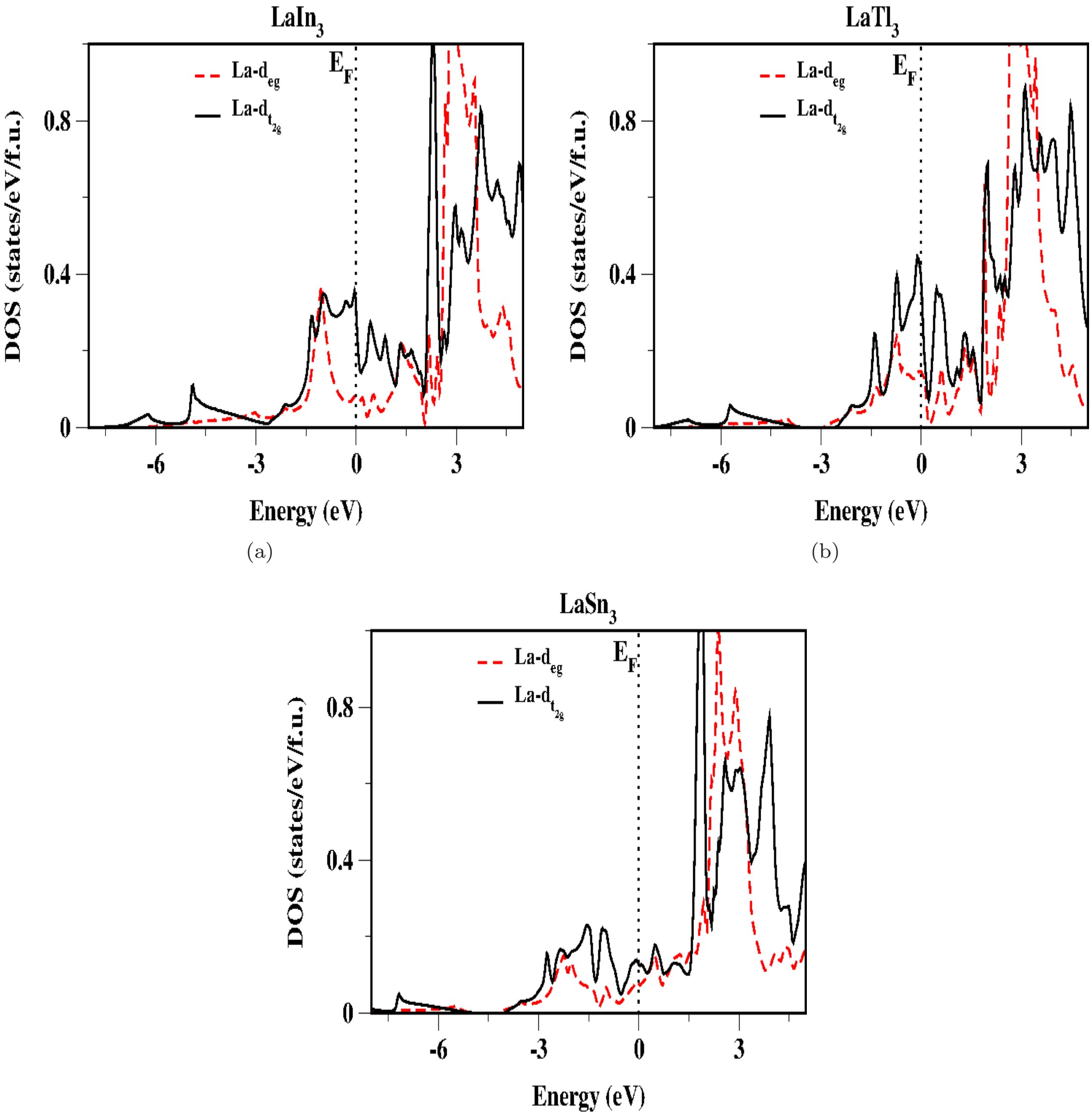

(a)

(b)

(c)

Figure 4.7: m-projected DOS of La 'd' states for LaX$_3$ with X = In, Tl, Sn, at the experimental lattice constants and including spin-orbit coupling (SOC). The contribution at E_F is mainly due to the La '$d_{t_{2g}}$' orbital character.

splittings are larger in their “partner materials” La_3Sn and La_3Tl, wheras in $LaIn_3$, the X ‘*s*’ and ‘*p*’ states merge. The occurrence of the pseudogap in binary alloys may be either of ionic origin or due to hybridization [146]. The electronegativity difference between La and X is not large, so the La_3X and LaX_3 compounds cannot be termed as ionic. Rather, the appearance of the pseudogap reflects the covalent bonding between the La and X atoms, as the valence state energies of La and X atom are nearly the same. Only one pseudogap is found in the LaX_3 type compounds, while La_3X compounds exhibit two pseudogaps, which indicates a stronger ‘*p*’-‘*d*’ hybridization in the La_3X compounds.

An interesting feature of the investigated La_3X compounds is their high values of the total DOS at the Fermi level, $N(E_F)$. This feature was already concluded on the basis of measured specific heat and susceptibility [63]. A large value of $N(E_F)$ may indicate instability of the compounds with respect to symmetry lowering distortions, but from the calculated elastic constants, to be discussed in the next section, all these compounds are found to be mechanically stable. The calculated total density of states at E_F are 7.8, 6.9 and 6.3 states/eV/f.u., for La_3In, La_3Tl and La_3Sn, respectively, i.e. slightly decreasing from La_3In to La_3Tl and La_3Sn. The Sommerfeld coefficient of specific heat may be obtained as

$$\gamma = \left(\frac{\pi^2}{3}\right) N(E_F) k_B^2,$$

where k_B is Boltzmann’s constant, leading to γ = 18.4, 16.2 and 14.8 mJ/mole K^2, for La_3In, La_3Tl and La_3Sn, respectively. These values are compared with other available theoretical and experimental results in Table-4.1. The total DOS at the Fermi level calculated in Ref. [69] is in excellent agreement with the present values, while the measured Sommerfeld coefficients are significantly higher than the calculated, suggesting that a considerable phonon-induced enhancement is present in these compounds [63]. In next chapter a quantitative analysis of electron-phonon interaction and superconductivity in the La_3X and LaX_3 families of compounds will be presented.

4.3.3 Fermi surface at ambient condition

The Fermi surface (FS) of the La_3X compounds as calculated at their experimental equilibrium volumes including SOC are shown in Fig. 4.8 and 4.9. The similarity of the FS topology for La_3In, La_3Tl and La_3Sn is evident, which confirms the dominance of the La ‘*d*’ orbitals at E_F, discussed in connection with the DOS plots in Fig. 4.4 and 4.5. In La_3In, there are three bands crossing the Fermi level and the corresponding FS is shown in Fig. 4.8 (a-c). For La_3Tl (Fig. 4.8 (d, e))

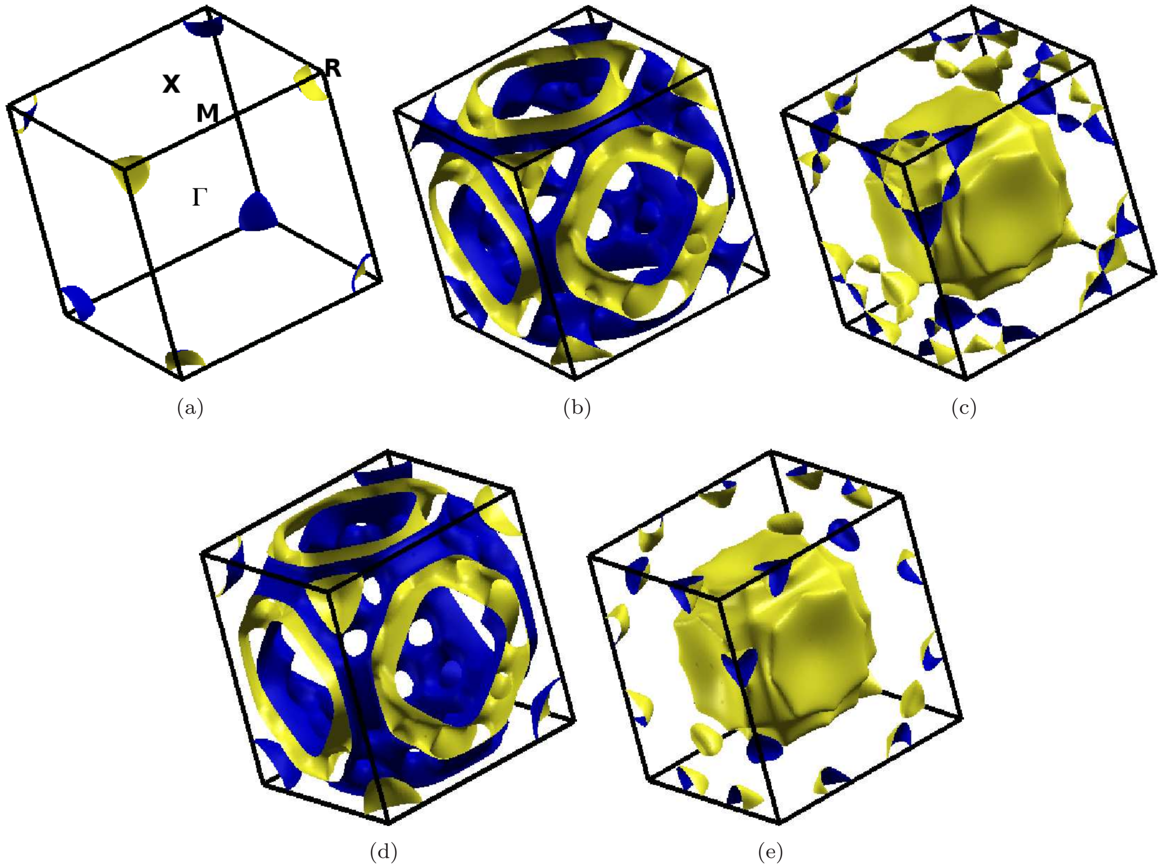

(a) (b) (c)

(d) (e)

Figure 4.8: Fermi surface topology of (a-c) La_3In, (d-e) La_3Tl including spin-orbit coupling (SOC) at their experimental lattice constants.

and La_3Sn (Fig. 4.9 (a-d)) the number of FS sheets are two and four, respectively. Comparing the topology of La_3In and La_3Tl, an extra hole pocket around the R point appears in La_3In (Fig. 4.8 (a)), but not in La_3Tl. This originates from the red colored band in Figs. 4.10 (a) and (c)), which remains below E_F in La_3Tl. Furthermore, in the second sheet of La_3In (Fig. 4.8 (b)) there is an opening along the Γ-R direction, which becomes closed in the corresponding first sheet of La_3Tl (Fig. 4.8 (d)). This is due to the band (broken blue line in Fig. 4.10 (a) and 4.10 (c)) crossing E_F three times along the Γ-R direction in La_3Tl but only once in La_3In, leading to the formation of an isolated closed hole pocket around the R point in La_3Tl (Fig. 4.8 (d)). Finally, in the third sheet of La_3In (Fig. 4.8 (c)) an electron pocket appears along the X-R direction, which is absent in the corresponding second sheet of La_3Tl (Fig. 4.8 (e)). This is due to the band (dotted magenta band in Fig. 4.10 (a) and (c)) crossing E_F twice along X-R in La_3In, but remaining above E_F in La_3Tl.

In the case of La_3Sn there is one more electron, and compared to La_3Tl two extra electron pockets around Γ are formed, as shown in Fig. 4.9 (c ,d). The first sheet (Fig. 4.9 (a)) is a thin

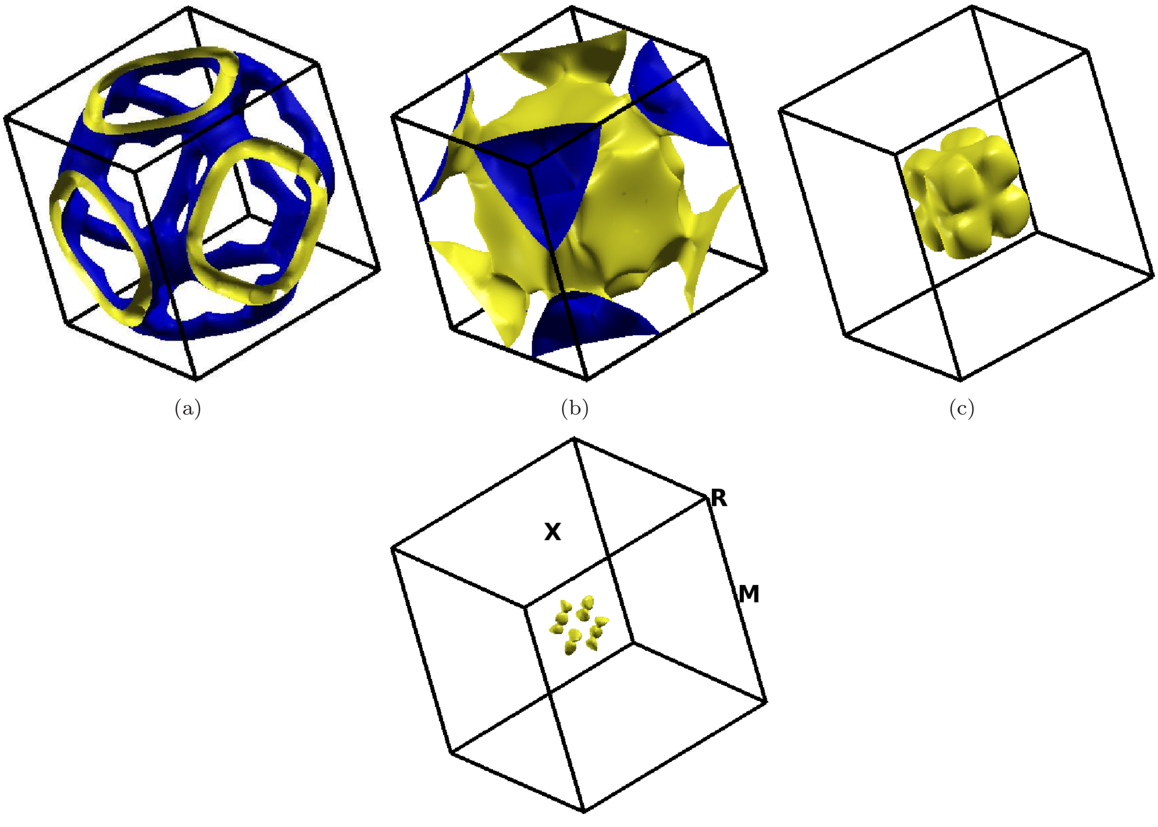

(a) (b) (c) (d)

Figure 4.9: Fermi surface topology of (a-d) La_3Sn, including spin-orbit coupling (SOC) at their experimental lattice constants.

filamental hole-structure corresponding to the first sheet of La_3Tl and second sheet of La_3In. The second sheet of La_3Sn (Fig. 4.9 (b)) is similar to the second sheet of La_3Tl (Fig. 4.8 (e)) and third sheet of La_3In (Fig. 4.8 (c)), however open along the Γ-R direction, leading to one singly connected sheet, as opposed to the fragmented sheets in La_3In and La_3Tl. This is also revealed from the band structure plots in Fig. 4.11, where a band (dotted magenta) is seen to cross E_F along the Γ-R direction once for La_3In (Fig. 4.10 (a)) and La_3Tl (Fig. 4.10 (c)) but remaining below E_F in the case of La_3Sn (Fig. 4.11 (a)).

In previous chapter, we have discussed the Fermi surfaces of LaX_3 compounds. The bands around E_F in La_3X and LaX_3 share the property that they are strongly hybridized between La '*d*' and X '*p*', however the dominance of La '*d*' states in the La_3X compounds versus the dominance of X '*p*' states in the LaX_3 compounds leads to different sets of bands, even when X is a trivalent atom and the total electron count would be the same. The LaX_3 compounds all have two Fermi sheets, one sheet of complex structure together with one simple electron pocket around the R point ($LaIn_3$ and

$LaTl_3$) or hole pocket around Γ ($LaSn_3$).

4.3.4 Effects under compression

The effects of compression on La_3X materials are analyzed by comparing the bands and Fermi surfaces calculated for the experimental equilibrium volumes, V_0, to those found when the volumes are reduced to $V/V_0 = 0.8$, i.e. a 20% compression. Generally, application of compression causes the band widths to increase, see Fig. 4.10 and 4.11, and leads to the FS topology changes, illustrated in Fig. 4.12 and 4.13. By comparing the left-hand and right-hand panels of Fig. 4.10 and 4.11, several details of these changes can be understood. In the case of La_3In the electron pocket along the X-R line seen in the third Fermi sheet at V_0 vanishes at $0.8{\times}V_0$ and it is evident from the Fig. 4.12 (a), due to the upward movement of the band shown in Fig. 4.10 (a, b) as the dotted, magenta line. In addition, there is a major change in the second surface where the interconnected two sheets around the Γ-R direction become separated as shown in Fig. 4.12 (b). In the complicated second FS sheet the connectivity of the upper and lower sheet breaks around Γ-R, the region is indicated by the arrow in Fig. 4.12 (b). Looking at the FS topology of La_3Tl under pressure, the similarity to La_3In is evident by the Fig. 4.12 (d-f). Under compression the valence band (red, solid line Fig. 4.10 (c,d)) moves upwards at the R point leading to the formation of a new hole pocket around the R point (Fig. 4.12 (d)), similar to the first Fermi sheet seen in La_3In already at V_0 (Fig. 4.8 (a)). In the second surface the closed hole sheet at the R point opens up along the Γ-R direction similar to what happens in La_3In as shown in Fig. 4.12 (e) and is indicated by the arrow. A FS topology change is also observed in La_3Sn under compression, as the fourth electron sheet disappears (Fig. 4.9 (e)). In addition a major change is found in the first sheet, where the completely interconnected sheet transforms into a large number of small pieces of Fermi surface pockets (Fig. 4.13 (a)). In addition, the opening along the Γ-R direction in the second surface is closing at $V/V_0 = 0.8$ (Fig. 4.13 (b)). The shape of the electron pocket around the Γ point in the third sheet is changing, but the topology is unaltered (Fig. 4.13 (c)).

4.3.5 Elastic constants and mechanical properties

The elastic constants C_{11}, C_{12} and C_{44} [123, 124] and the related mechanical properties of La_3In, La_3Tl and La_3Sn are calculated at the experimental equilibrium volumes and listed in Table-4.2. There are no other experimental or theoretical results available for comparison. All the compounds are found to be stable by satisfying the stability criteria $C_{11} > C_{12}$, $C_{44} > 0$, and $C_{11} + 2C_{12} > 0$.

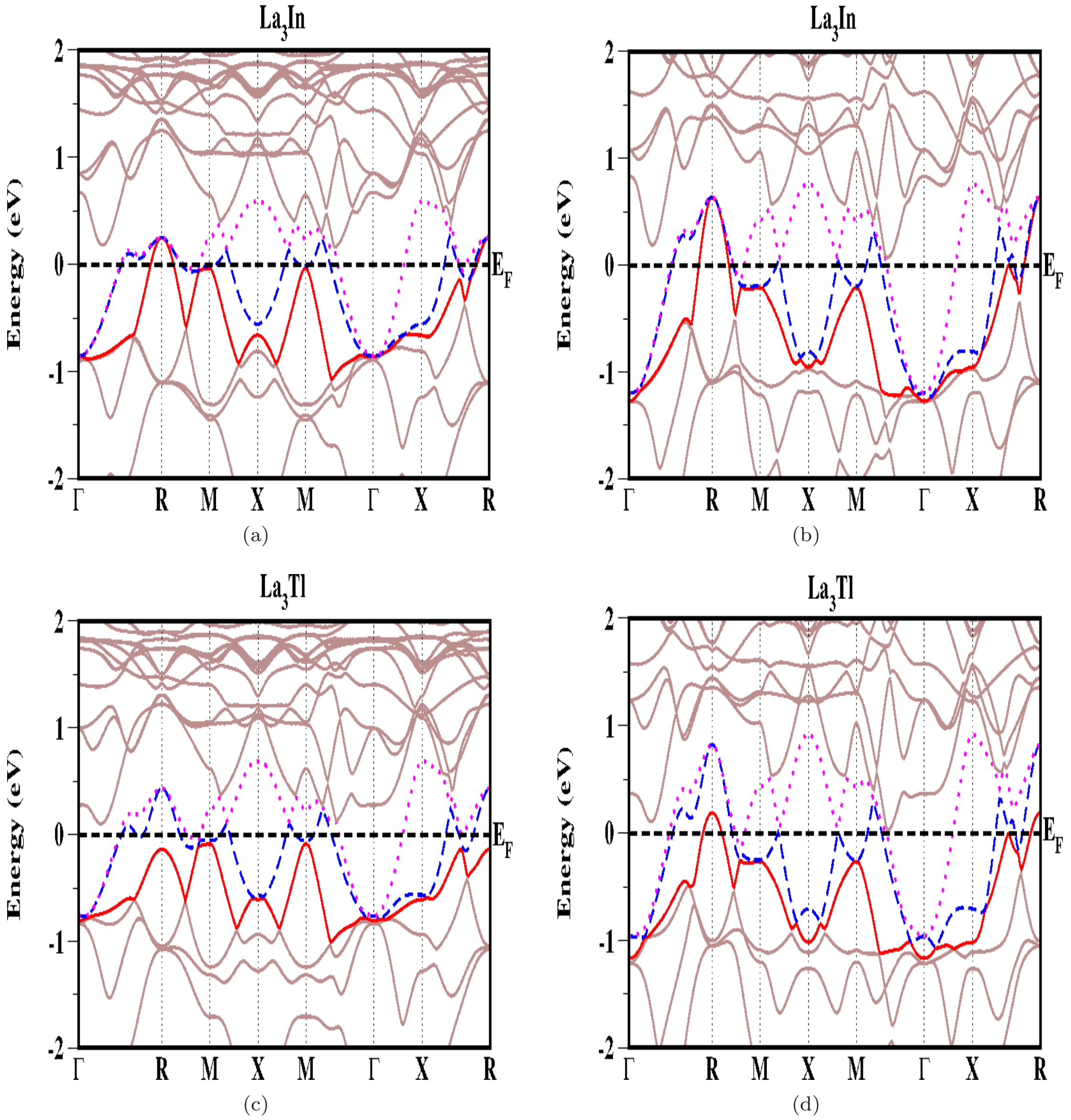

(a) (b) (c) (d)

Figure 4.10: Band structure of La$_3$In, La$_3$Tl with spin-orbit coupling (SOC), left panels (a, c) are at the experimental lattice constants, while the right panels (b, d) are under compression at V/V$_0$ = 0.80, where V$_0$ denotes the experimental volume. The color code used for the plots is similar at ambient and compressed volume and is introduced to ease the identification of pressure induced changes to the band structure.

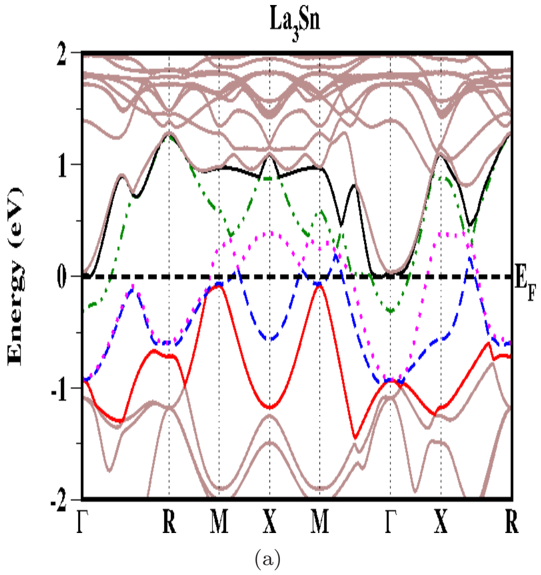

(a)

(b)

Figure 4.11: Band structure of La_3Sn with spin-orbit coupling (SOC), left panels (a) is at the experimental lattice constants, while the right panels (b) is under compression at $V/V_0 = 0.80$, where V_0 denotes the experimental volume. The color code used for the plots is similar at ambient and compressed volume and is introduced to ease the identification of pressure induced changes to the band structure.

The calculated bulk modulus, B of the La_3X compounds are reported in Table-4.2. The La_3X compounds are found to be softer than their "partner compound" LaX_3 for a specific X atom: For $LaIn_3$ $B = 51\ GPa$, as opposed to $B = 39.3\ GPa$ for La_3In; for $LaTl_3 = B = 48\ GPa$, as opposed to $B = 40.3\ GPa$ for La_3Tl; for $LaSn_3$ $B = 56\ GPa$, as opposed to $B = 37.8\ GPa$ for La_3Sn.

From the values of C_{11}, C_{12} and C_{44} one may calculate Hill's [126] shear modulus G_H (which is the arithmetic mean of the Reuss [127] and Voigt [128] approximations), Young's modulus E, the Poisson ratio σ and several related elastic properties, which are included in Table-4.2 (the formulas are given in chapter-3 in equation-(3.1-3.5)). According to Pugh [138], the ratio between the shear modulus and the bulk modulus G_H/B relates to the ductile versus brittle nature of a given compound. If $G_H/B < 0.57$, the material behaves in a ductile manner, otherwise the material is brittle. Sometimes, a positive value of the Cauchy pressure ($C_p = C_{12} - C_{44} > 0$) is used for the same classification. From Table-4.2, $LaIn_3$ and La_3Tl obey these inequalities and thus may be classified as ductile materials, while La_3Sn is on the borderline between brittle and ductile. Poisson's ratio σ (see Table-4.2) is calculated using the formula from equation-3.4 given in chapter-3.

Another important parameter of a material is the elastic anisotropy $A = 2C_{44}/(C_{11} - C_{12})$ (see Ref. [149]). A value of A smaller or greater than unity measures the degree of elastic anisotropy of the material. The calculated values of A indicate that the La_3X compounds are elastically

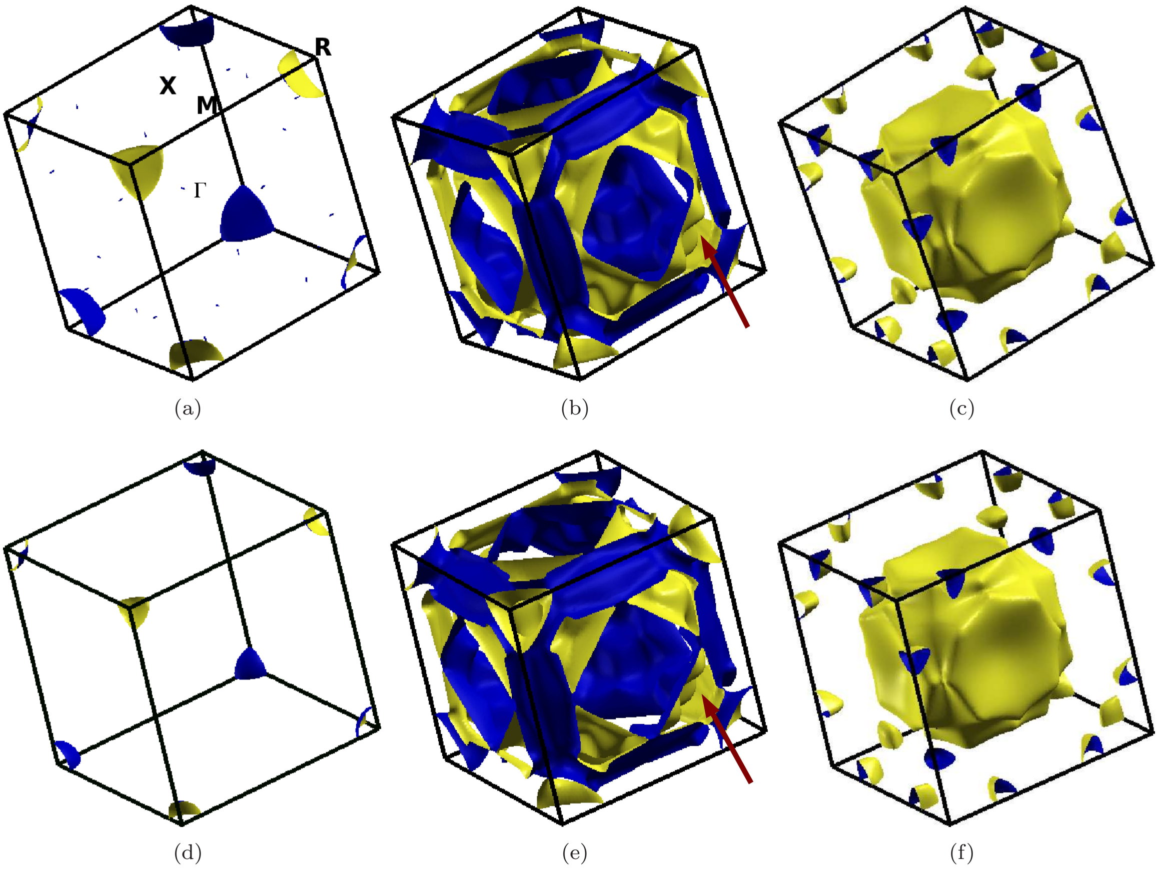

(a) (b) (c)

(d) (e) (f)

Figure 4.12: Fermi surface topology of (a, b, c) La_3In, (d, e, f) La_3Tl, including spin-orbit coupling (SOC) under compression at $V/V_0 = 0.80$. The arrow in (b, e) points to the region where the FS connectivity changes compared to $V = V_0$ (Fig. 4.8 (b, d)).

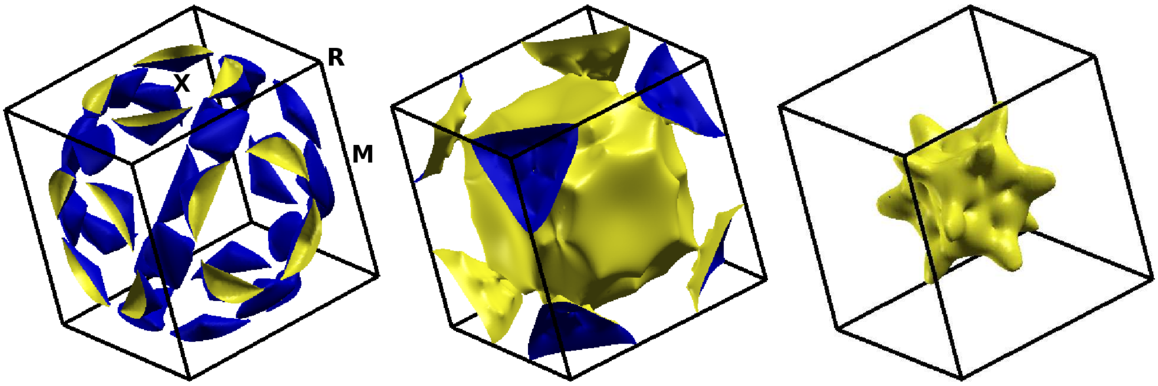

(a) (b) (c)

Figure 4.13: Fermi surface topology of (a, b, c) La_3Sn, including spin-orbit coupling (SOC) under compression at $V/V_0 = 0.80$.

anisotropic. To compare the relative magnitude of the elastic anisotropy, A^*, calculated in percent are tabulated in Table-4.2. It emerges that the anisotropy of the crystal is decreasing from In → Tl → Sn. The calculated Debye temperatures of La_3In and La_3Tl are in good agreement with the available experimental values. Unfortunately, there are no values available for comparison in the case of La_3Sn. Comparing the elastic properties of La_3X with LaX_3 both the La rich and the X rich compounds are found to be ductile in nature with considerable elastic anisotropy.

Table 4.2: Elastic constants and derived quantities for La_3X (X= In, Tl, Sn), as calculated with the experimental equilibrium volume. A is the anisotropy factor, $A = 2C_{44}/(C_{11} - C_{12})$, the degree of the elastic anisotropy, $A^* = 3(A-1)^2/[3(A-1)^2 + 25A)]$ (Ref. [149]), B is the bulk modulus and $C_p = C_{12} - C_{44}$ is the Cauchy pressure.

Parameters	La_3In	La_3Tl	La_3Sn
C_{11} (GPa)	54.2	54.3	59.1
C_{12} (GPa)	31.8	33.2	27.2
C_{44} (GPa)	21.9	20.5	26.9
A	1.96	1.95	1.69
A^*(%)	5.3	5.3	2.4
G_H (GPa)	16.7	15.7	21.8
B	39.3	40.3	37.8
E (GPa)	43.9	41.7	54.9
σ	0.31	0.33	0.26
G_H/B	0.42	0.39	0.576
C_p (GPa)	9.9	12.7	0.3
v_l (km/s)	3.01	2.77	3.16
v_t (km/s)	1.57	1.41	1.80
Θ_D (K)	163.9	147.2	185.8
	170(10)[a]	163(8)[a]	

a: Ref. [63]

4.4 Conclusion

The electronic structure, density of states and Fermi surfaces of La_3X (X= In, Tl, Sn) are calculated using the density functional theory at ambient volume as well as under compression. The states at the Fermi level are dominated by the La '*d*' orbitals in all La_3X compounds with a significant admixture of X '*p*' states. In contrast, in the LaX_3 compounds the X '*p*' orbitals dominate at E_F. In addition, a strong '*p*'-'*d*' hybridization is found in La_3X type compounds, leading to high densities of states at E_F, which is comparatively weaker in LaX_3 compounds. This is attributed to the different nearest-neighbor surroundings of the atoms in La_3X and LaX_3 with local tetragonal symmetry around La in La_3X but octahedral symmetry around La in LaX_3. Compression induced FS topology changes are predicted for all the compounds. The elastic and related mechanical properties have been calculated for all the compounds. The La_3X compounds are found to be ductile, as are the LaX_3 compounds. Despite having different electronic structure and Fermi surface topology, all La_3X and LaX_3 compounds are found to have quite similar mechanical properties in the La rich and X rich compounds.

Chapter 5

Superconducting properties of binary Cu_3Au-type compounds: Effect of compression

The effects of applying external pressure to the superconducting materials A_3X (A= La; X= In, Sn) and AX_3 (A= La, Y; X = In, Sn, Pb) are simulated by ab initio quantum mechanical calculations using the density functional theory. At zero pressure, the highest value of the superconducting transition temperature (T_c) is found in La_3In, 6.36 K and the lowest, 0.27 K in $LaIn_3$ and the electron-phonon coupling constants, λ_{ep} are 0.98 and 0.36, respectively. Among the AX_3 compounds, the superconducting transition temperature of Y containing compounds are found to be higher than in those with A = La although for a particular X atom the density of states at the Fermi level is higher in LaX_3 than in YX_3. It is found that the two types of compounds AX_3 and A_3X respond differently to application of pressure. T_c of A_3X-type compounds *increases* with pressure, probably due to a softening of the lower phonon frequecy mode especially A_{2g} and E_u mode. On the other hand T_c is found to *decrease* with increasing pressure for AX_3-type compounds due to a simultaneous hardening of all the phonon modes. The calculated trend of T_c under pressure agrees well with the available experimental results for La_3In and $LaSn_3$. In the case of La_3In a pressure-induced dynamical instability is predicted with appearance of imaginary frequencies, in particular at the M and R points in the Brillouin zone due to continuous softening of A_{2g} and E_u modes irrespective of the hardening of the higher frequency modes.

5.1 Introduction

The intermetallic isostructural AX_3 [82, 49] (A= La, Y; X = In, Sn, Pb) and A_3X [63, 144, 65] (A= La; X= In, Sn) type compounds, having cubic Cu_3Au-type structure often exhibit unusual behaviours in superconductivity, resistivity, thermopower etc. as a function of composition. Many studies on LaX_3 (X= Sn, In, Tl, Pb) compounds show an oscillatory behaviour in superconducting transition temperature (T_c), thermopower and magnetic susceptibility as functions of the average valence-electron number [82, 78, 109, 137, 49]. Garde et. al [65] have observed a strong negative curvature in the resistivity versus temperature curves of La_3X compounds with X = Al, Sn, Ru, Ir, Co, Ge, Ga, at intermediate temperatures and a stabilization at higher temperature. Further they [65] found two extrema in thermopower curve for La_3Sn, La_3Ru and La_3Co, whereas only one extremum was seen for La_3In, La_3Al, La_3Ga compounds. Superconductivity, magnetic and thermodynamic properties of La_3Tl were examined experimentally by Bucher et. al [145]. Heiniger et. al [63] found La_3In and La_3Tl to be strong-coupling superconductors and later the presence of high electronic density of states near the Fermi level (E_F) was reported for the same compounds [66]. The effects of heat treatment and stoichiometry variation on the T_c of La_3In were explained by Gschneidner et. al [150]. Recent experimental investigations of superconductivity of YSn_3 [80] and YIn_3 [114] have shown that T_c of YSn_3 is 7 K whereas T_c of YIn_3 is 0.7 K. An earlier experimental study on La_3In by Smith et. al [84] showed that T_c increases with pressure. The superconductivity of $LaSn_3$ under pressure was reported by Huang et. al [81], who found an initial increase of T_c in a small pressure range about 0.8 *kbar* and then a decrease for higher values of pressure. The main motivation to study the lanthanum based intermetallic compounds La_3X and LaX_3 is to investigate the effect of X atom substitution on the superconducting properties at ambient as well as under pressure. The main interesting point is that, among all the investigated systems, La_3In has highest superconducting transition temperature (10.4 K) [63], whereas $LaIn_3$ has the lowest transition temperature, 0.7 K [82, 83] at ambient pressure. Our aim is to understand the origin of the superconductivity for all the investigated systems and to study the behaviour of the T_c under pressure for the A rich A_3X (A = La) compounds and X rich (A = La, Y) AX_3 compounds. Till now, there are no theoretical studies available regarding the superconducting behaviour of these compounds at ambient as well as under pressure, apart from the theoretical studies on superconductivity in YSn_3 by Dugdale [118] and YIn_3 by Billington et. al [151] both at ambient pressure. The present chapter contains a detailed study of the phonon dispersion and T_c for all the mentioned compounds under pressure. The remaining part of this chapter is organized as follows. In section-5.2 the computational method is described, section-5.3 contains the results obtained concerning superconductivity of the AX_3 and A_3X compounds at ambient as well as elevated pressure, and section-5.4 concludes the chapter.

5.2 Method of calculation

The Quantum Espresso package [104] has been used for the electron-phonon coupling constant and the phonon dispersion. To treat the exchange-correlation function we have used generalized gradient approximation of Perdew, Burke and Ernzerhof [98]. In order to deal with the possible convergence problem for metals, a smearing technique is employed using the Methfessel-Paxton (MP) scheme, with the smearing parameter set to 0.04 Ry for La_3X type compounds and 0.02 Ry for the AX_3 type compounds. For the description of the electron-ion interaction the Vanderbilt ultrasoft pseudopotentials were used [152]. For the energy convergence we have used the wave function and charged-density cutoffs of 30 Ry and 360 Ry, respectively. We used density functional linear-response theory [104, 153] to calculate phonon spectra and electron-phonon coupling constants. Within the linear response approach this allows the treatment of arbitrary phonon wave vectors in the Brillouin zone, while avoiding the large supercells. The electrons are approximated in a dense k-mesh of $32 \times 32 \times 32$ in the Monkhorst-pack [120] scheme for self-consistent cycles. In order to obtain the phonon dispersion curves, we have calculated the phonon frequencies on a $4 \times 4 \times 4$ q-point grid and phonon dispersions were then obtained by Fourier interpolation of the dynamical matrices. These dynamical matrices were Fourier transformed to obtain the full phonon spectrum and density of states.

5.3 Results and discussions

5.3.1 Superconductivity of the AX_3 and A_3X type compounds

In order to obtain the superconducting transition temperatures (T_c) and to analyze the electron-phonon coupling mechanism of all the AX_3 (A= La, Y; X = In, Sn, Pb) and A_3X (A= La; X = In, Sn) compounds, we have studied the phonon-dispersion, electron phonon coupling constant λ_{ep} and the Eliashberg [154] function ($\alpha^2F(\omega)$) for all the compounds. The total phonon density of states (PDOS), the Eliashberg function and phonon dispersion at experimental equilibrium volume (V_0) for all the compounds are given in Figs. 5.1-5.7. From the Eliashberg function, we have calculated the electron-phonon coupling constant λ_{ep} for all the compounds. Having calculated the λ_{ep} we estimate T_c for all by using Allen-Dynes formula [43] as in equation-5.1 and the values are reported in Table-5.1 along with the calculated electronic density of states at Fermi level ($N(E_F)$).

$$T_c = \frac{\omega_{ln}}{1.2} \exp\left(-\frac{1.04(1+\lambda_{ep})}{\lambda_{ep} - \mu^*(1+0.62\lambda_{ep})}\right) \tag{5.1}$$

Here ω_{ln} is the logarithmically averaged phonon frequency and the dimensionless μ^* is the Morel-Anderson [155] Coulomb pseudo-potential. The value $\mu^* = 0.1$ was chosen in all T_c calculations reported here [118].

Again λ_{ep} can be calculated from the following relation,

$$\lambda_{ep} = 2\int \frac{d\omega\alpha^2(\omega)F(\omega)}{\omega} = \frac{N(E_F)\langle I^2\rangle}{M\langle\omega^2\rangle} \tag{5.2}$$

Where $\alpha(\omega)$ and F(ω) are the strength of an average electron-phonon interaction and the phonon density of states, respectively. $\langle I^2\rangle$ is the mean of the square of the electron-ion interaction, M is the atomic mass and $\langle\omega^2\rangle$ is the average of the square of the phonon frequency. The calculated T_c and λ_{ep} values obtained here are in good agreement with the available experimental and other theoretical values.

AX_3-type compounds (A = La, Y; X = Sn, Pb, In)

When we compare the superconducting transition temperature of LaX$_3$ and YX$_3$ compounds for a particular X atom with X = Sn, Pb, In, we find T_c as well as electron-phonon coupling constant to be higher in YX$_3$ compounds than the LaX$_3$ compounds and is reported in Table-5.1, although the density of states at the Fermi level ($N(E_F)$) of YX$_3$ is smaller than that of LaX$_3$. The observed trend of T_c for La and Y containing AX$_3$ type compounds agree well with the experimental result [80], where the authors substantiate the result by showing T_c to be small for the compound with large lattice parameter and large for those where the lattice parameter is small. From the analysis of the phonon density of states and the Eliashberg function as shown in Fig. 5.1 (a-c), 5.2 (a-c) and 5.3 (a-c), we find the width of the phonon density of states and the Eliashberg function to be wider in YX$_3$ for X = Sn, Pb, In, compounds than in LaX$_3$. Again in Fig. 5.3 (a-c) it can be seen that the peak of the Eliashberg function is higher in the Y containing compounds than those with La, which indicates the electron-phonon coupling constant to be higher for YX$_3$ in comparison with the LaX$_3$ and is well supporting our calculated values of T_c for the investigated LaX$_3$ and YX$_3$ compounds. Comparing AX$_3$ compounds for different X atoms, the highest peak in the Eliashberg function is found for X = Sn, and then followed by APb$_3$ and AIn$_3$, in accordance with the trend in the calculated values of T_c. The calculated phonon dispersion relations (Fig. 5.4 (a-c), 5.5 (a-c) for AX$_3$

Table 5.1: Calculated electronic density of states at the Fermi level, $N(E_F)$ (evaluated at the experimental equilibrium volumes (V_0)), together with derived Sommerfeld coefficient of specific heat, γ, electron phonon coupling constant, λ_{ep} and superconducting transition temperature, T_c for AX_3 (A = La, Y; X = In, Sn, Pb) and A_3X (A = La; X= In, Sn) compounds.

Compounds		$N(E_F)$	γ (mJ/mol K^2)	λ_{ep}	T_c (K)
$LaIn_3$	Present work	2.58^*	6.06	0.36	0.27
	Expt.	2.19^a			0.7^b,0.71^c
	Others^d	1.89	5.09		
$LaSn_3$	Present work	2.67^*	6.28	0.81	5.23
	Expt.	2.6, 2.8	11.66^e, 10.96^f	0.8	6.45^h, 6.02^b
			11.0^g		
	Others^d	2.15	6.03	0.82	
$LaPb_3$	Present work	3.41^*	8.02	0.72	3.28
	Expt.				4.05^h,4.1^b,4.18^c
YIn_3	Present work	2.34^*	5.49	0.37	0.34
	Expt.				0.78^b, 1.08^i
	Others^j	1.81	4.26	0.42	0.77
YSn_3	Present work	2.41^*	5.67	0.83	5.42
	Expt.		7.57^k		7.0^k
	Others^l	1.92	4.53	0.99	5.93
YPb_3	Present work	3.12^*	7.33	0.86	4.58
	Expt.				4.72^b, 4.6^m
La_3In	Present work	7.8^*	18.40	0.97	6.36
	Expt.	6.00^n	14.00^n		9.54^n, 10.4^o
	Others	4.41			13.11^p
La_3Sn	Present work	6.29^*	14.83	0.76	4.26
	Expt.				6.2^q

* from our previous study Ref. [156], [157] and [158]
a: Ref. [49]; b: Ref. [82]; c: Ref. [83]; d: Ref. [132]; e: Ref. [159]; f: Ref. [81]
g: Ref. [131]; h: Ref. [129]; i: Ref. [114]; j: Ref. [151]; k: Ref. [80]
l: Ref. [118]; m: Ref. [78]; n: Ref. [63]; o: Ref. [144]; p: Ref. [69]
q: Ref. [64]

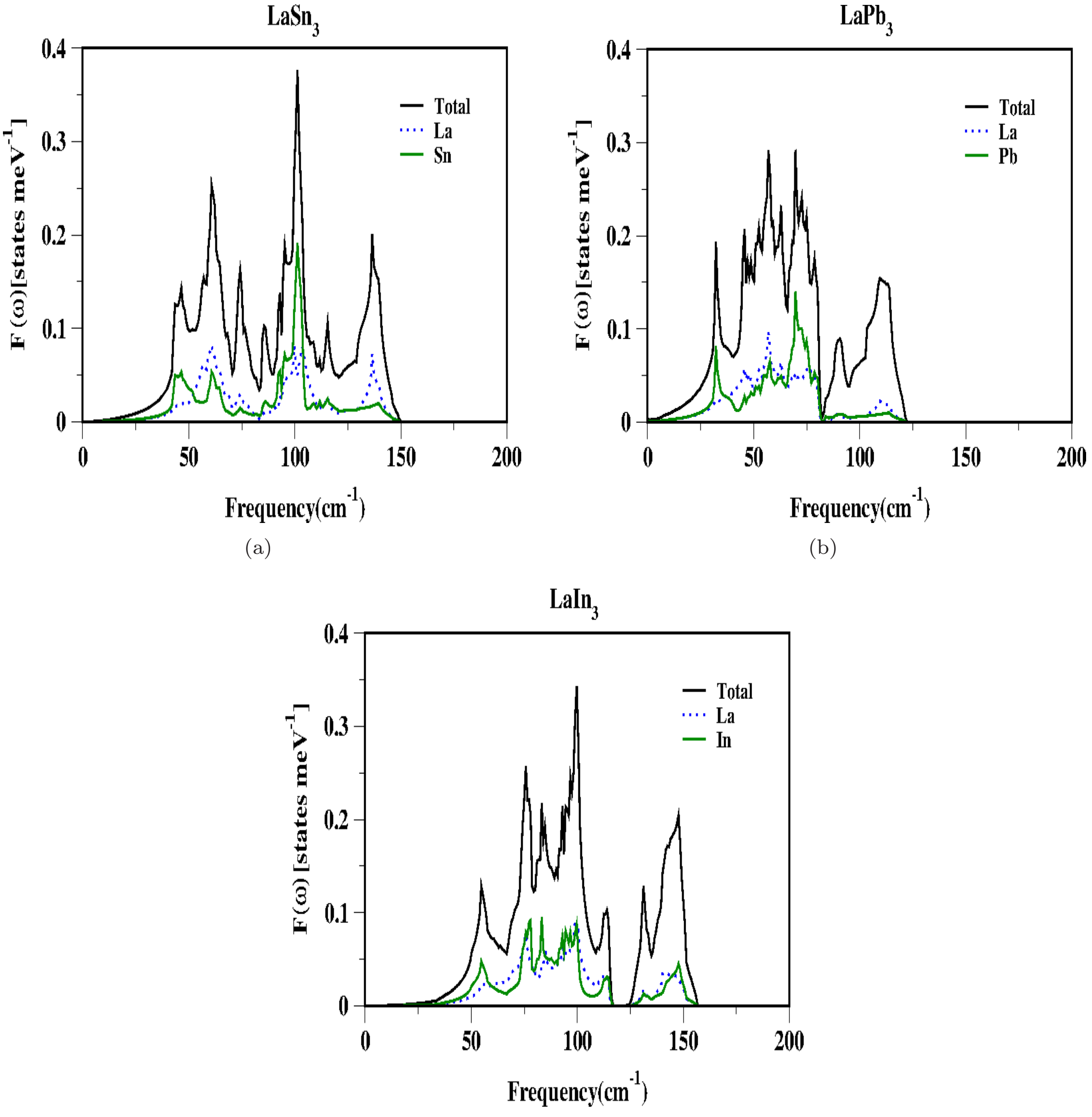

(a) (b) (c)

Figure 5.1: Total and partial phonon density of states for LaX_3 with X = Sn, Pb, In compounds at $V/V_0 = 1.0$.

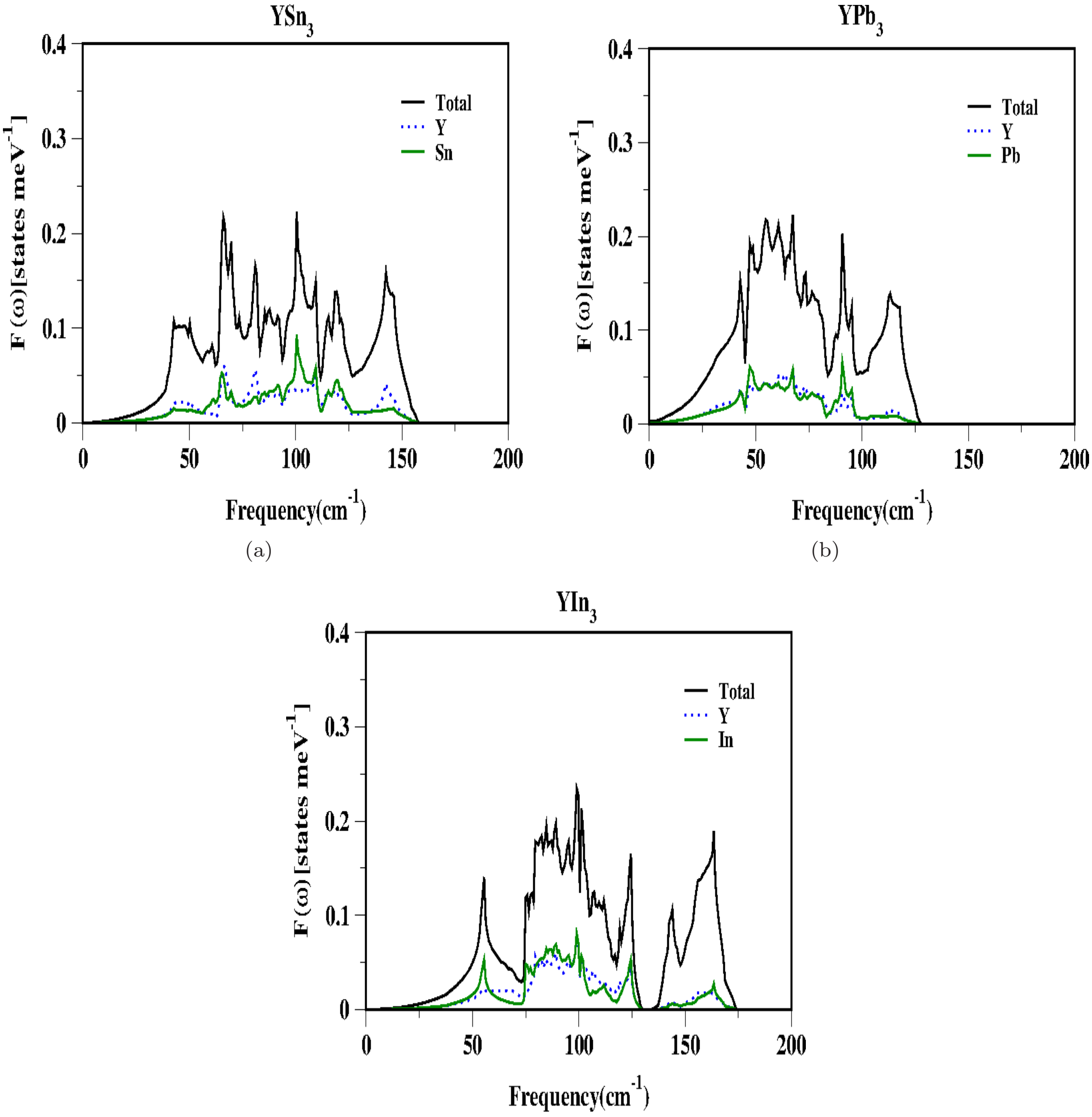

(a)

(b)

(c)

Figure 5.2: Total and partial phonon density of states for YX_3 with X = Sn, Pb, In compounds at $V/V_0 = 1.0$.

compounds and 5.6 (a, b) for La_3X compounds) have shown that no mode softening ("imaginary" frequencies), leading to dynamical instability was found in the compression range considered here.

For AX_3 type compounds a drop in T_c was found in $LaIn_3$ and YIn_3 which could be due to a weak interaction of the atoms, resulting in opening of a gap in the phonon dispersion as shown in Fig. 5.4 (c), 5.5 (c). For all the AX_3 compounds, there is nearly equal contribution from A and X atom, but slightly dominating nature of X atom is seen in the lower frequency regions which is well evident from the partial density of states in Fig. 5.1, 5.2 and the central region is dominated by the X-type atoms, where the Eliashberg function is high as illustrated in Fig. 5.3 (a-c) and this might be the dominating character to determine the superconductivity of these AX_3 compounds.

A_3X-type compounds (A = La; X = Sn, In)

For the La_3X (X = In, Sn) type compounds, it is found that $N(E_F)$ is quite high in comparison with those of LaX_3 (X = In, Sn) compounds, which may be related to the structural instability of the La_3X compounds. To examine the dynamical stability of these La_3X compounds we have calculated the phonon-dispersion along high symmetry direction for all the compounds and found no imaginary phonon modes at ambient for both La_3In and La_3Sn as shown in Figs. 5.6 (a, b) at zero pressure and this gives the conformation about the stability of these compounds. In the previous chapter (chapter-4) we have also studied the mechanical stability of these compounds and found La_3In and La_3Sn [158] to be mechanically stable. When we try to analyse the PDOS for La_3X compounds, we find the highest peak of PDOS at around 100 cm^{-1} as shown in Figs. 5.7 (a) and (b), is dominated by the X (In, Sn) atom and the lower frequency ranges are of La type. From the Eliashberg function as shown in Fig. 5.7 (c, d) it is seen that the peak of La_3In is slightly higher than in La_3Sn suggesting the electron-phonon coupling constant to be higher for former compound, and this agrees with our λ_{ep} values as reported in Table-5.1. The calculated values of the T_c are also found to be higher in La_3In than in La_3Sn, which supports our discussion.

Comparison between AX_3 and A_3X-type compounds

Now, comparing the superconductivity of the La_3X and LaX_3 compounds, it is seen that the superconducting transition temperature (T_c) decreases by replacing In with Sn for La rich La_3X type compounds (La_3In = 6.36 K, La_3Sn = 4.26 K), whereas for X rich LaX_3 compounds T_c is found to increase when In is substituted for Sn ($LaIn_3$ = 0.27 K, $LaSn_3$ = 5.23 K). The T_c is higher in La_3In and $LaSn_3$ in comparison to that of $LaIn_3$ and La_3Sn respectively, and this might be due to the high electron-phonon coupling constant in the former compounds. This is also reflected in the calculated values of λ_{ep} as reported in the Table-5.1. On the other hand the higher T_c for La_3In in comparison to $LaIn_3$ is also mainly due to the electron-phonon coupling constant of La_3In (λ_{ep} = 0.98, T_c =

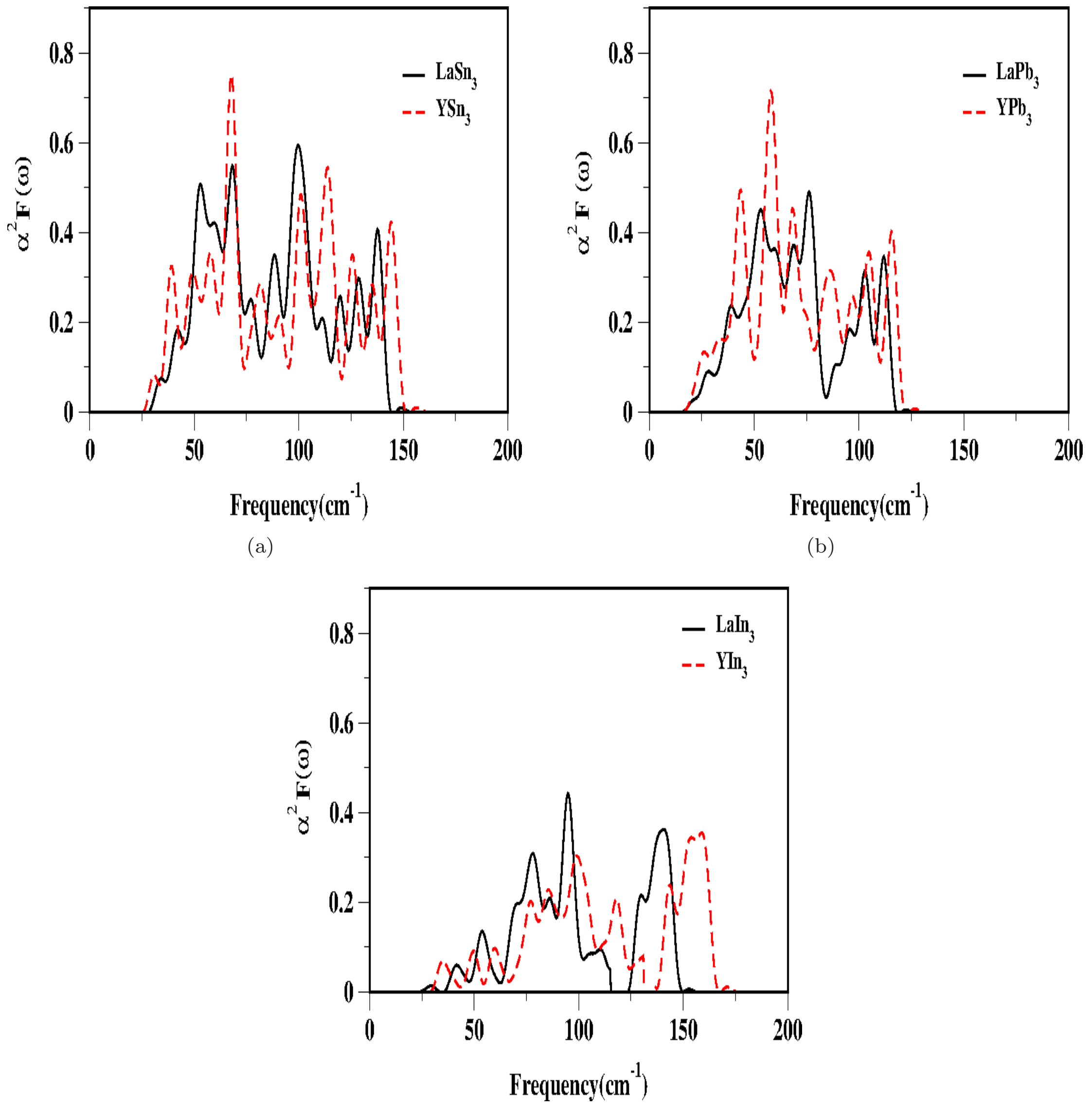

(a)

(b)

(c)

Figure 5.3: Eliashberg function for AX$_3$ with A = La, Y; X = Sn, Pb, In compounds at V/V$_0$ = 1.0.

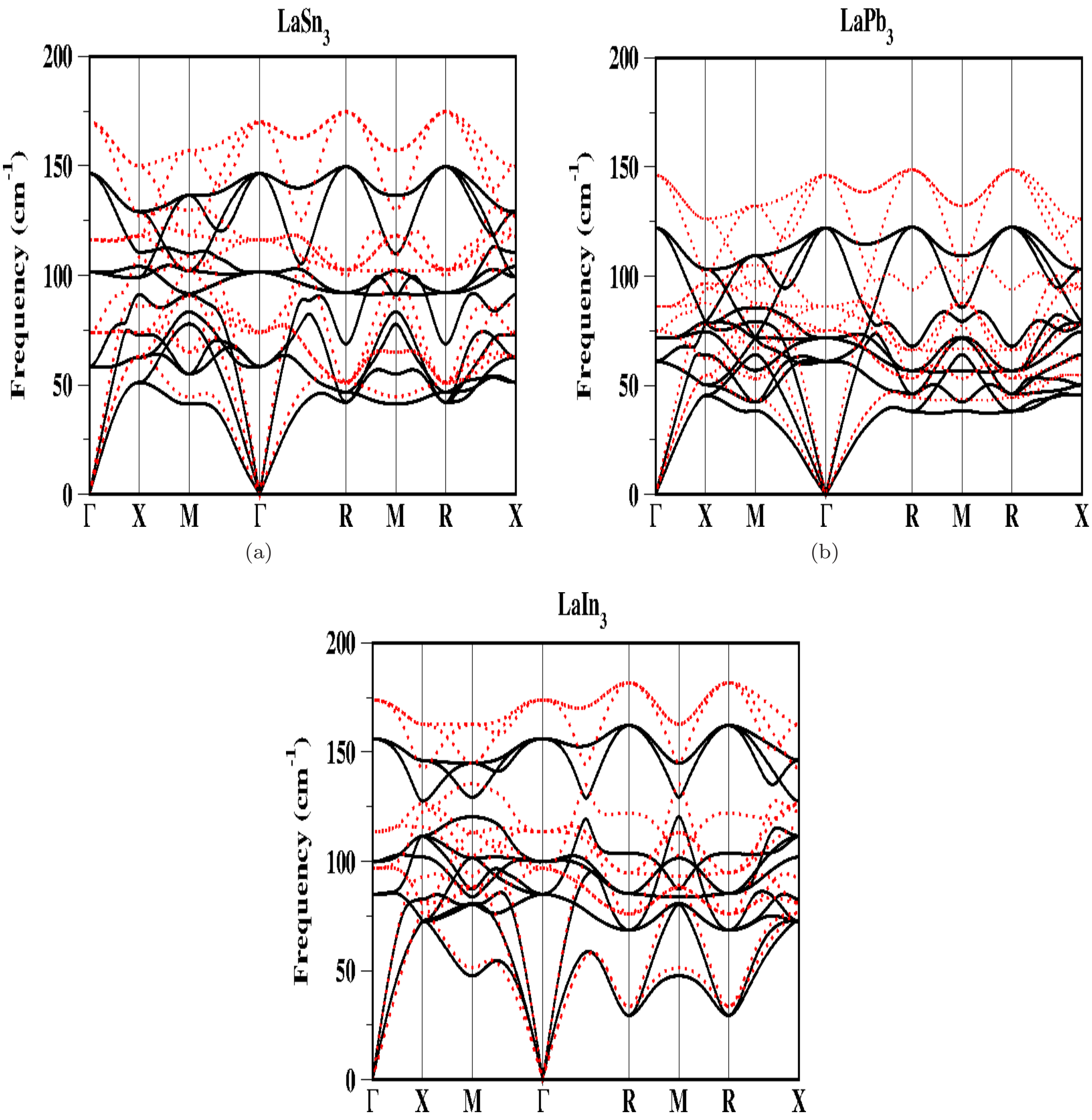

(a)

(b)

(c)

Figure 5.4: Phonon dispersion along high symmetry direction for LaX$_3$ (X = Sn, Pb, In) at ambient as well as under compression at V/V$_0$ = 0.9 (solid black lines for V/V$_0$ = 1.0 and red dotted lines for V/V$_0$ = 0.9). The hardening of all frequency mode is seen in LaX$_3$ compounds.

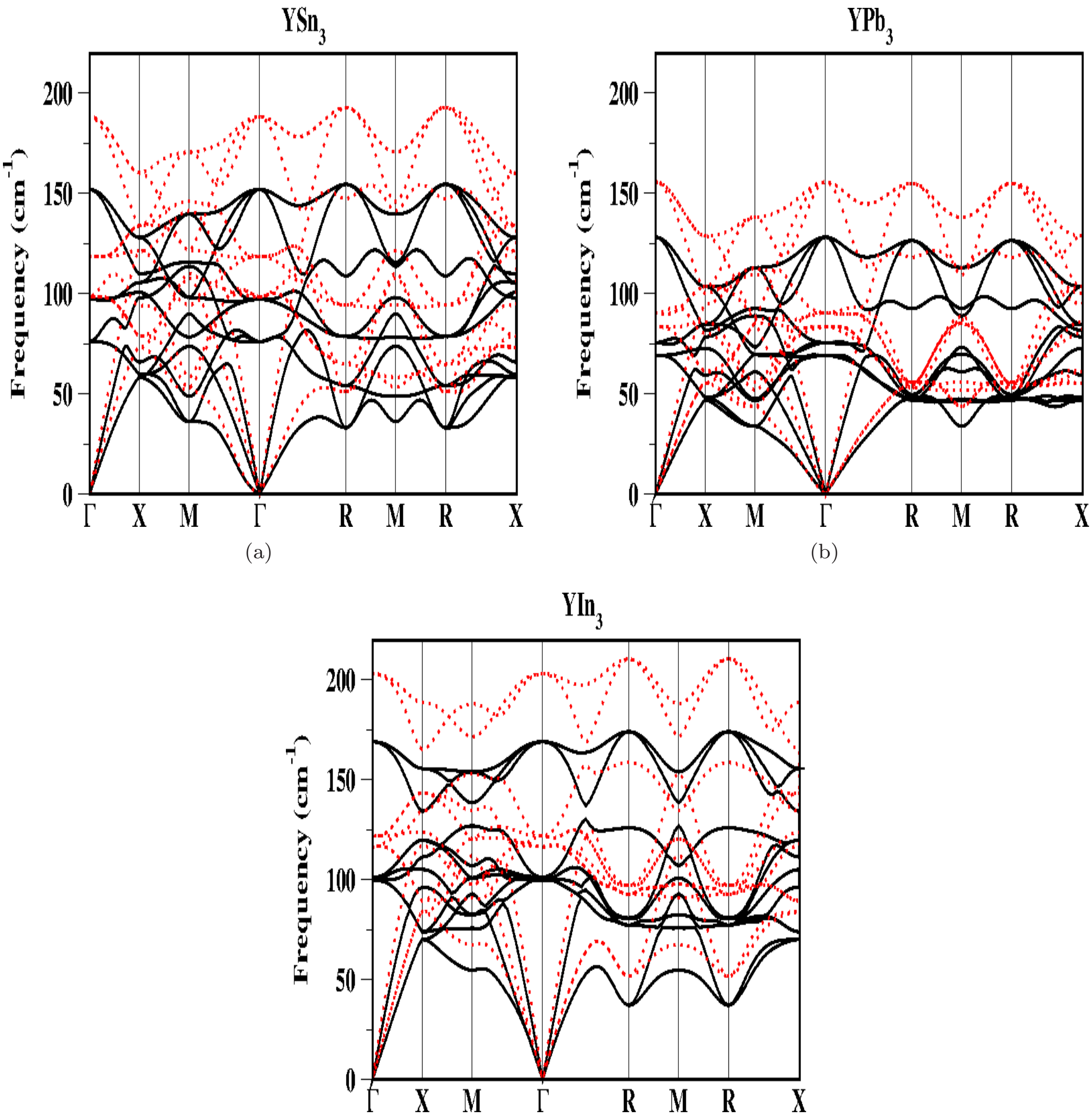

(a)

(b)

(c)

Figure 5.5: Phonon dispersion along high symmetry direction for YX$_3$ (X = Sn, Pb, In) at ambient as well as under compression at V/V$_0$ = 0.9 (solid black lines for V/V$_0$ = 1.0 and red dotted lines for V/V$_0$ = 0.9). The hardening of all frequency mode is seen in YX$_3$ compounds.

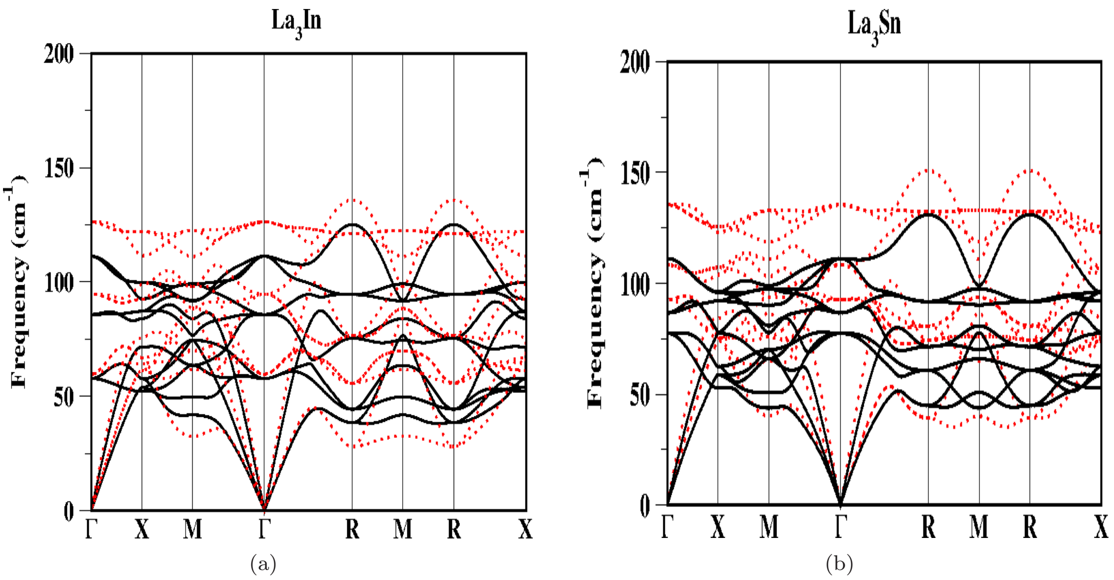

Figure 5.6: Phonon dispersion along high symmetry direction for La_3X (X = In, Sn) at ambient as well as under compression at $V/V_0 = 0.9$ (solid black lines for $V/V_0 = 1.0$ and red dotted lines for $V/V_0 = 0.9$). The softening of lower frequency mode particularly at M and R points is seen in La_3X irrespective to the hardening of higher frequency mode.

6.34 K) being larger than that in $LaIn_3$ ($\lambda_{ep} = 0.36$, $T_c = 0.27$ K), whereas T_c is found to be less in La_3Sn ($T_c = 4.26$ K) than in $LaSn_3$ ($T_c = 5.23$ K) which again is due to λ_{ep} for La_3Sn ($\lambda_{ep} = 0.76$) being smaller than that of $LaSn_3$ ($\lambda_{ep} = 0.81$). Finally, from the calculated λ_{ep}, T_c, PDOS and Eliashberg functions of all the investigated compounds, it emerges that the superconductivity is dominated by the A atom for A_3X (A = La; X = In, Sn) type compounds and for AX_3 type compounds it is dominated by the X atom, and there is a large variation of the coupling constant when X is varied in the AX_3 compounds in comparison to the A_3X compounds.

5.3.2 Pressure effect on superconducting properties

The main interesting feature in all the investigated compounds under pressure is the observed positive dependence of the T_c for A_3X (A = La; X = In, Sn) with increase of the coupling constant and the negative dependence for AX_3 (A = La, Y; X = In, Sn, Pb) type compounds with decrease of the coupling constant and is shown in Figs. 5.8 (a) and (b). Experimentally Huang et. al [81] have reported the pressure effect on T_c for $LaSn_3$ and found initial increase of the T_c for a small range of pressure of about 8 *kbar* and then decreases. In our calculation we have not found the initial increase of T_c for $LaSn_3$, but at nearly $V/V_0 = 0.94$ (pressure around 1 GPa) we find slight increase of T_c, then decrease. A similar situation is found in Nb [160], where the authors were not able to

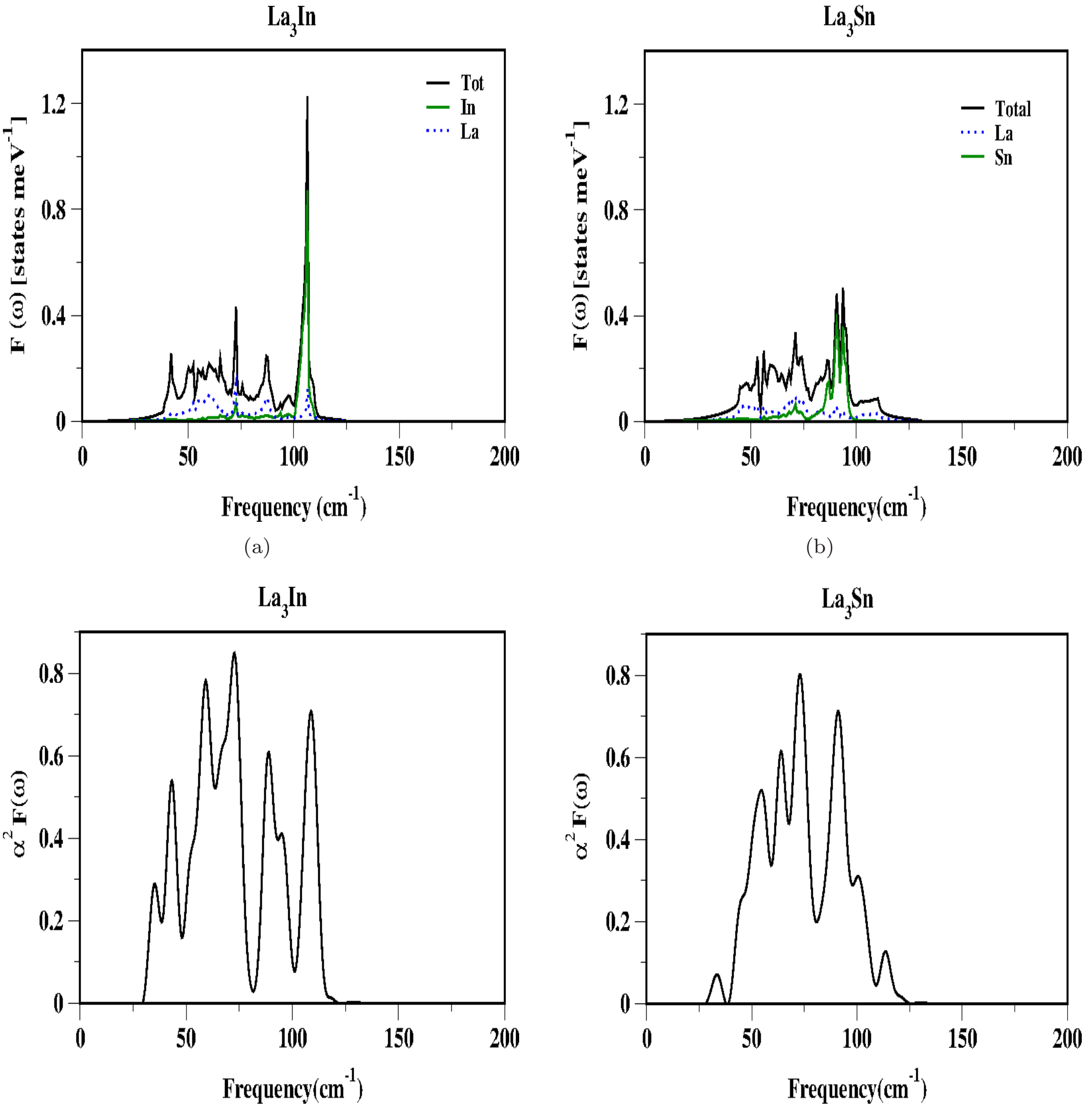

(a) (b) (c) (d)

Figure 5.7: (a, b) Total and partial phonon density of states, (c, d) Eliashberg function, for La$_3$X with X = Sn, In compounds at V/V$_0$ = 1.0.

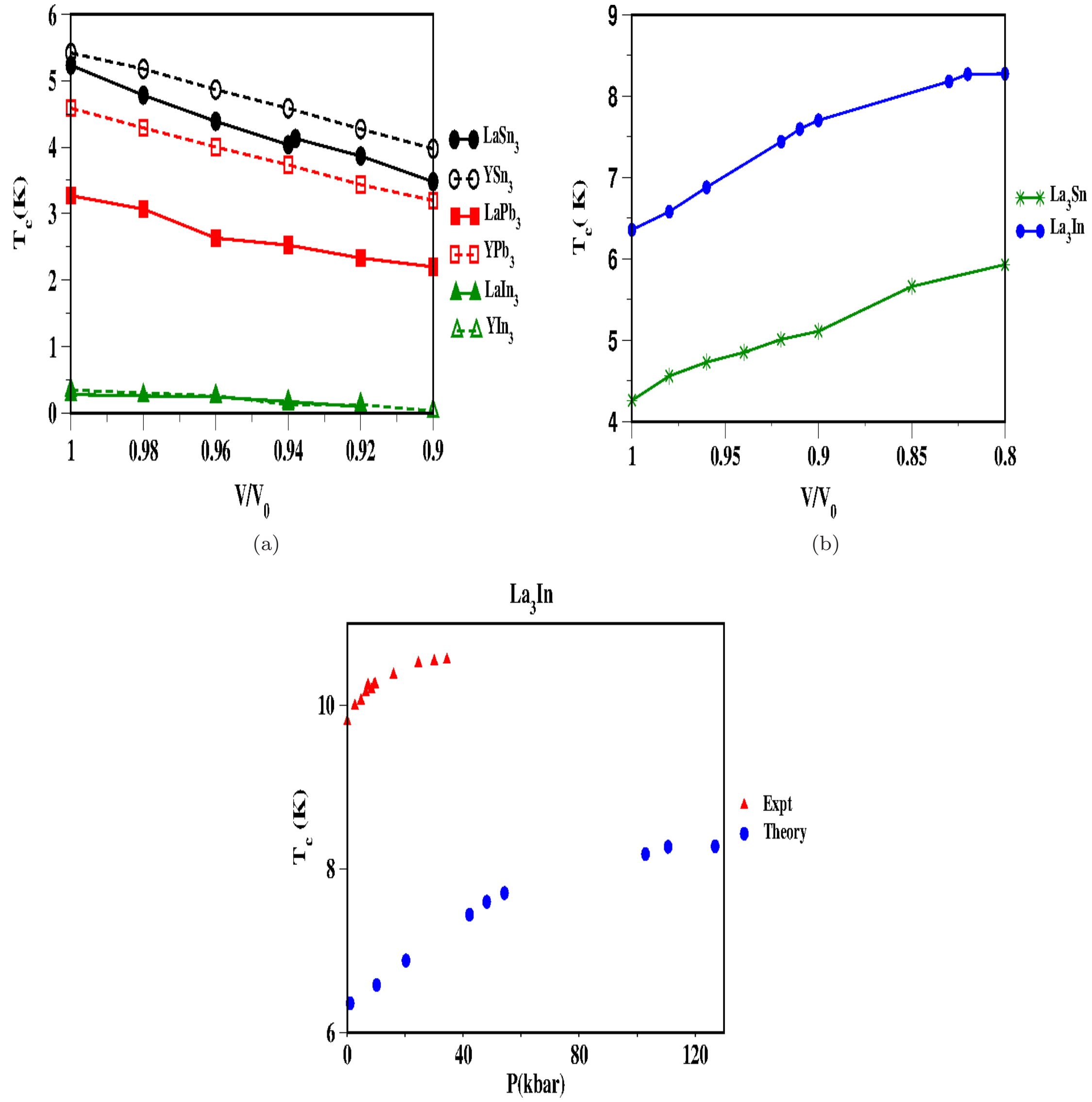

(a) (b)

(c)

Figure 5.8: Variation of superconducting transition temperature, T_c under compression for (a) AX_3 (A = La, Y; X = Sn, Pb, In) and (b) La_3X (X = In, Sn), (c) gives the information about the comparison between the experiment and our present calculation of T_c for La_3In under pressure.

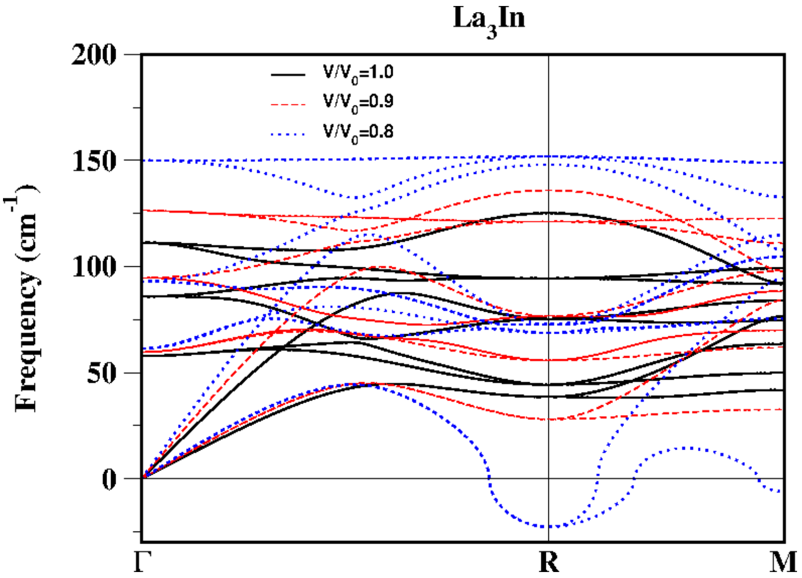

Figure 5.9: Phonon dispersion along high symmetry direction for La_3In at ambient as well as under compression. The phonon instability is seen along Γ-R-M direction at $V/V_0 = 0.8$.

show the initial increase of T_c with pressure as found in experiment and suspected that might be due to the non-hydrostatic pressure or due to the polycrystalline nature of the sample. The pressure dependence of T_c for La and Y containing compounds are found to be similar where we have seen T_c to decrease under compression and is evident from Fig. 5.8 (a). In our previous study [157, 156] we have observed Fermi surface topology to be nearly similar under pressure for $LaSn_3$ and $LaPb_3$ (chapter-3) and suspected the superconducting nature of these compounds to be the same. From the calculated T_c under compression as shown in Fig. 5.8 (a), a similar decreasing non-monotonic behaviour of these two compounds is confirmed. In addition to this, it can be seen that among all compounds the monotonic variation of the T_c under compression is only present for YPb_3 and YSn_3, where we did not find any Fermi surface topology change under compression [156, 157] (chapter-3). The observed Fermi surface topology change for the compounds under study [157, 158] could be related to the non-monotonic variation of the superconducting transition temperature and is well supporting the finding of the Huang et. al [81], where the authors concluded the observed change in T_c for $LaSn_3$ was due to the Fermi surface topology change. The same non-monotonic behaviour in T_c under compression is seen (see Fig. 5.8 (b)) for La_3X compounds, where we again find a Fermi surface topology change [158] (chapter-4). Again for La_3X compounds, an increase of T_c with pressure is found as shown in Fig. 5.8 (b). The calculated behaviour of the T_c under pressure for La_3In agrees well with the experimental finding by Smith et. al [84], where it was also shown that T_c increases with pressure for La_3In and an initially linear increase which at higher pressures changes into a constant is shown in Fig. 5.8 (c). Apart from this, we have also found a hardening of the higher frequency modes under compression for all the investigated AX_3 and La_3X compounds as can be seen from Fig. 5.4, 5.5 and 5.6 (dotted lines), whereas the lower frequency modes soften in La_3X in particular at the M and R points irrespective of the hardening of the modes in the other points (Fig. 5.6). There is no softening in the case of AX_3 compounds and we have seen the continuous hardening of all the modes at all the symmetry points (Fig. 5.4, 5.5). The observed increase of T_c in La_3X compounds with pressure may be due to this observed softening of the lower frequency mode under compression, especially A_{2g} and E_u mode at M and R points respectively, irrespective of simultaneous hardening of the higher frequency modes as shown in Fig. 5.6 (a, b). Similar softening of the A_{2g} and E_u mode is not found for the LaX_3 compounds, as can clearly be seen from Fig. 5.4, 5.5 (a-c). This might be the reason for the decreasing T_c with compression for AX_3 compounds. A phonon instability is predicted for La_3In under high compression ($V/V_0 = 0.8$), due to the continuous softening of the A_{2g} and E_u modes at the M and R points as shown in Fig. 5.9. The similar lattice instability under pressure as found here for La_3In is reported in the case of MgB_2 [161], in that case due to softening of the B_{1g} mode.

5.4 Conclusion

The phonon dispersion, electron-phonon coupling constant and superconducting transition temperature (T_c) of A_3X (A= La; X= In, Sn) and AX_3 (A= La, Y; X= In, Sn, Pb) compounds under compression are studied using density functional theory. The superconducting transition temperature is found to be high in Y containing compounds in comparison with the La containing compounds among AX_3 series despite the density of states being higher in LaX_3 compounds, which is due to the electron-phonon coupling constant being higher in YX_3 than the LaX_3 compounds. An increase of T_c with pressure is found for La_3X, whereas T_c is found to decrease for AX_3 compounds. In addition a continuous hardening of all the modes is found for AX_3 compounds. A softening of the lower frequency mode, in particular at the M and R points is observed for La_3X compounds. This might be the reason for the observed decreasing and increasing behaviour of the superconducting transition temperature with pressure in AX_3 and La_3X compounds, respectively. Opposite to $LaIn_3$, a lattice instability is found in the case of La_3In under high compression due the continuous softening of the A_{2g} and E_u mode at the M and R points.

Chapter 6

Lattice dynamics and superconducting properties of La_3InZ (Z = N, O)

Electronic and superconducting properties of La_3InZ (Z = N, O) compounds are studied and are compared with La_3In. From the density of states of La_3InZ it is quite clear that the hybridization between La '*d*' and In '*p*' states get reduced with the inclusion of the Z atom in comparison with La_3In. A Fermi surface topology change is observed only in La_3InO under compression, which is attributed to the non-monotonic variation of the density of states and ultimately induce a non-linear variation of T_c. The mechanical and the dynamical stability of these compounds is confirmed from the elastic constant and the phonon dispersion calculation respectively. Cauchy's pressure, Pugh's ratio and Poission's ratio values indicate $La_3InN(O)$ to be brittle(ductile) in nature and agree well with the experiment. The calculated superconducting transition temperature (T_c) is less than 2 K for N containing compound, and is found to be above 2 K for O containing compound and the trend agree well with the experimental findings. The reason for the suppression of T_c due to the inclusion of the Z atom is also discussed from the band structure and phonon dispersion plots, where we find the phonon modes to harden in La_3InZ.

6.1 Introduction

Over the past few decades the binary intermetallic alloys of AX_3 and A_3X, (A = La, X = Sn, In, Tl) type have been widely investigated which are found to be superconductors and the reported superconducting transition temperature (T_c) is found to be highest around 10 K in La_3In [63]. It is quite interesting to study the superconducting properties of La_3InZ compounds formed by addition of Z (N, O) atom to La_3In yet retaining in the same space group of La_3In. Earlier studies report an enhancement of the T_c by addition of carbon in YNi_4B [162], whereas the decrease in T_c was reported by addition of carbon in La_3X (X = Al, Ga, In, Tl) compounds [69]. The presence of superconductivity in La-Ca-Cu-O compound was reported under high oxygen pressure, whereas the superconductivity was found to vanish under low oxygen pressure [163]. Apart from this the reduction of T_c was also reported in MgB_2 by carbon doping [164]. Again from experimental study on the superconducting behavior of La_3InZ (Z = N, O) [68], it is to be noted that La_3In and La_3InO have T_c of the same range around 10 K, which further motivate us to study the role of Z in La_3InZ compounds. In this present chapter, we calculate the superconducting transition temperature of these compounds and show the presence of superconductivity below 2 K for La_3InN and above 2 K in the case of La_3InO at ambient. In addition, we also bring out the role of Z on the superconducting properties of La_3InZ compounds. Experimentally Jing-Tai Zhao et. al [68] have synthesized these compounds and reported the superconducting behavior at nearly 10 K for La_3InO, whereas the authors have not found any superconducting nature in La_3InN above 2 K. In addition Kirchner et. al [70] have studied experimentally as well as theoretically a series of $(R_3N)In$ (R = La-Nd, Lu, Sm-Tm) compounds and compared the bonding nature of La_3InN with La_3In theoretically. Apart from this no theoretical studies are available regarding the band structure, density of states, Fermi surface at ambient as well as under compression. The rest of the chapter is organized as follows: in section-6.2, we briefly discuss the computational details, results and discussions are presented in section-6.3, which contains electronic, Fermi surface, superconducting properties of these compounds and finally we summarize and conclude this chapter in section-6.4.

6.2 Method of calculation

The electronic structure calculations were performed using the full-potential linearized augmented plane wave (FP-LAPW) method as implemented in the WIEN2*k* [101] based on the generalized gradient approximation of Perdew, Burke and Ernzerhof (GGA-PBE) [98]. For the total energy convergence $R_{MT}K_{max}$= 8 was used, where R_{MT} is the smallest muffin-tin radius, and K_{max} is the plane wave cut-off. The charge density was Fourier expanded up to G_{max} = 12 a.u.$^{-1}$ The muffin-tin radii were chosen as 2.5 a.u for La, 2.3 a.u for In and 1.7 a.u for Z (N, O) atoms. A (44 × 44 × 44) k-point mesh in the Monkhorst-Pack [120] scheme was used during the self-consistent cycle to ensure accurate determination of the Fermi level. The three dimensional (3D) Fermi surface plots were generated with the help of the XCrySDen ((X-Window) CRYstalline Structures and DENsities) molecular structure visualization program [122]. Spin-orbit coupling (SOC) is not included for all the electronic structure calculations as we find the vicinity of the Fermi level to remain unaltered with the inclusion of the SOC. We have used the experimental lattice constant of 5.11 Å, and 5.19 Å, for La_3InN and La_3InO (Ref. [68]), respectively, and the corresponding experimental volumes are denoted by V_0 in the following.

For the electron-phonon coupling constant and the phonon dispersion plots, we have used the Quantum Espresso package [103, 104]. A smearing technique within Methfessel-Paxton (MP) scheme is used and the smearing parameter is set to 0.02 Ry for La_3InZ (Z = N, O) compounds. We have carried out convergence tests for different values of smearing parameters. For the energy convergence we have used the wave function and charged-density cutoffs of 30 Ry and 320 Ry, respectively for La_3InN and 56 Ry and 560 Ry, respectively for La_3InO. Phonon calculations were carried out for 4 × 4 × 4 Monkhorst-Pack q-point grid with Brillouin zone integrations on a 32 × 32 × 32 k-mesh. In Fig. 6.1 (a, b) we have plotted the crystal structure of La_3In and La_3InO.

6.3 Results and discussions

6.3.1 Band structure, density of states and Fermi surface

The calculated band structures of La_3InZ (Z = N, O) without spin orbit coupling at experimental volume (V_0) are presented in Fig. 6.1 (c, d). The band structure plots reveal the overall profile of both the compounds to be similar except band filling in the case of La_3InO due to an extra electron in O, which is also clearly seen in the corresponding Fermi surface (FS) and the density of states (DOS) as shown in Fig. 6.2, 6.3 and Fig. 6.4, respectively. From the FS plots we can see the three extra hole pockets centered at R point in the case of the La_3InN, which is absent in La_3InO due to the positioning of the band below the Fermi level (E_F) (see Fig. 6.2 (a-c) and see solid black, broken red and dotted blue color band in Fig. 6.1 (d)). In addition we have an extra electron sheet along Γ-R direction in the case of La_3InO as shown in Fig. 6.3 (c) (broken indigo color band in Fig.

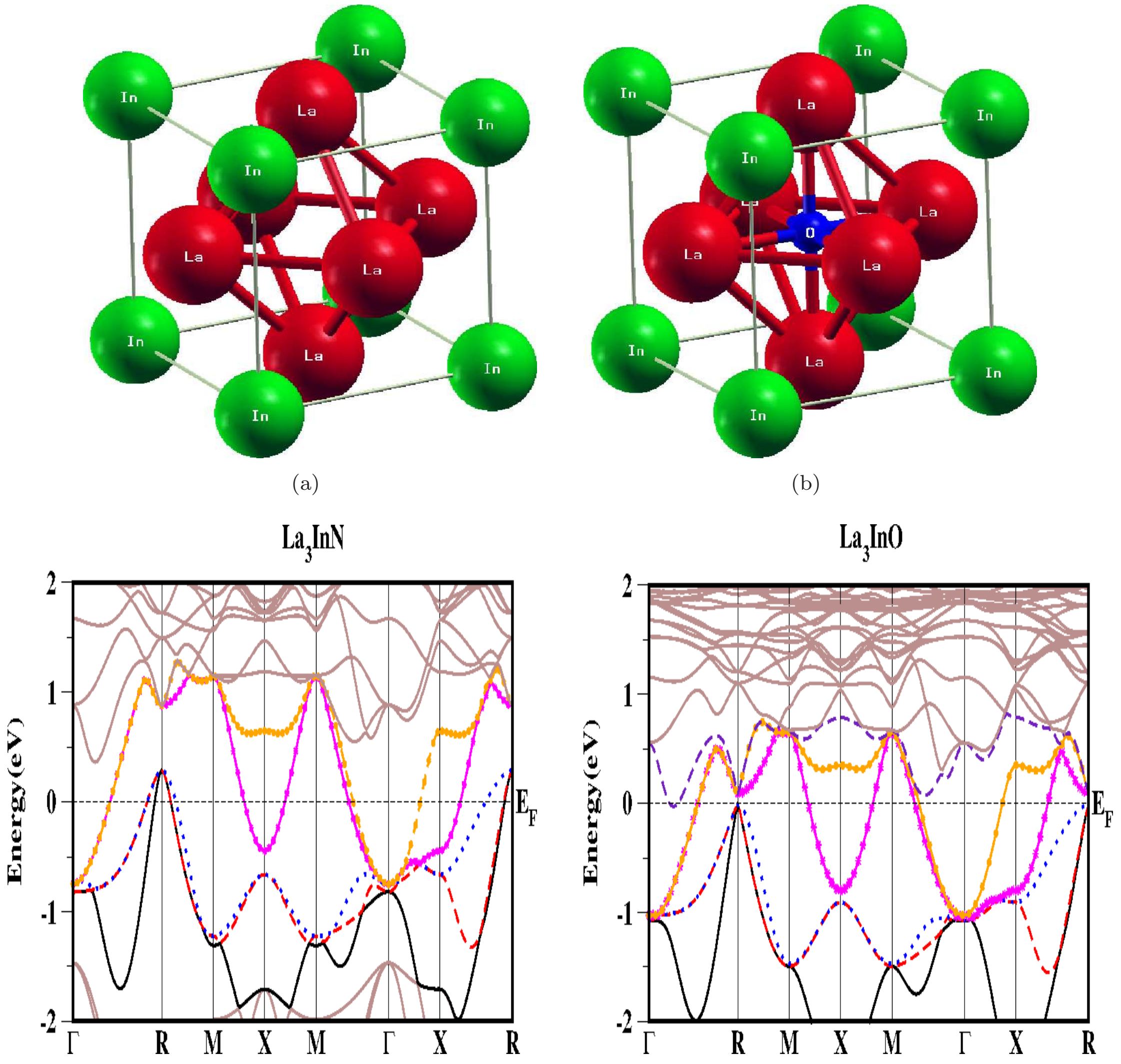

(a)

(b)

(c)

(d)

Figure 6.1: Crystal structure of (a) La_3In and (b) La_3InO and Band structure of (c) La_3InN and (d) La_3InO at $V/V_0 = 1.0$. The bands crossing the Fermi level are shown in different color.

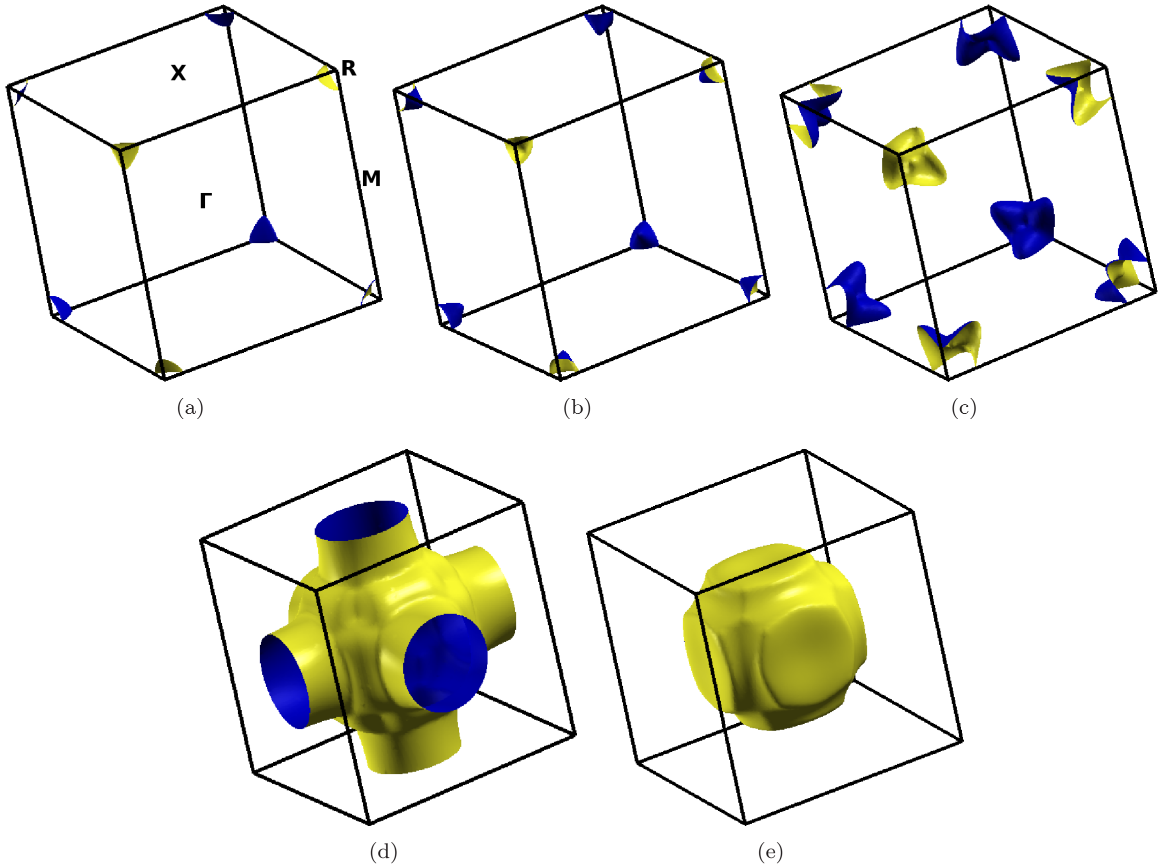

(a) (b) (c) (d) (e)

Figure 6.2: Fermi surface of La_3InN at V/V_0 = 1.0.

6.1 (d)). Apart from this the topology of the fourth FS of N containing compound (Fig. 6.2 (d)) and the first FS of O (Fig. 6.3 (a)) containing compound (see solid line with sphere magenta color band) are found to be similar except the increase in the width of the tube along Γ-X direction and are having both electron as well as hole character. This is again evident from the band structure plots in Fig. 6.1 (d) as we could see the same band to dip more below the E_F at X point in the case of La_3InO, resulting in wider opening along Γ-X. The fifth FS of N containing compound (Fig. 6.2 (e)) and the second FS of O containing compound (Fig. 6.3 (b)) are electron pocket centered at Γ, with size being larger in La_3InO than in La_3InN. If we compare the FS of the La_3In with La_3InZ (Z = N, O), we could find the FS topology of these compounds to be quite different as shown in Fig. 6.3 (d-f) (the details of the calculation regarding La_3In are presented in the chapter-4 [158]) and it is interesting to analyze and to compare La_3In and La_3InO which are claimed experimentally to be a superconductor with T_c around 10 K, provoking us to study the role of O in this compound. To analyze in detail, we have plotted the density of states of La_3InZ along with La_3In as shown in Fig. 6.4. More interestingly we find the E_F of both La_3InO and La_3In to fall very close to the peak.

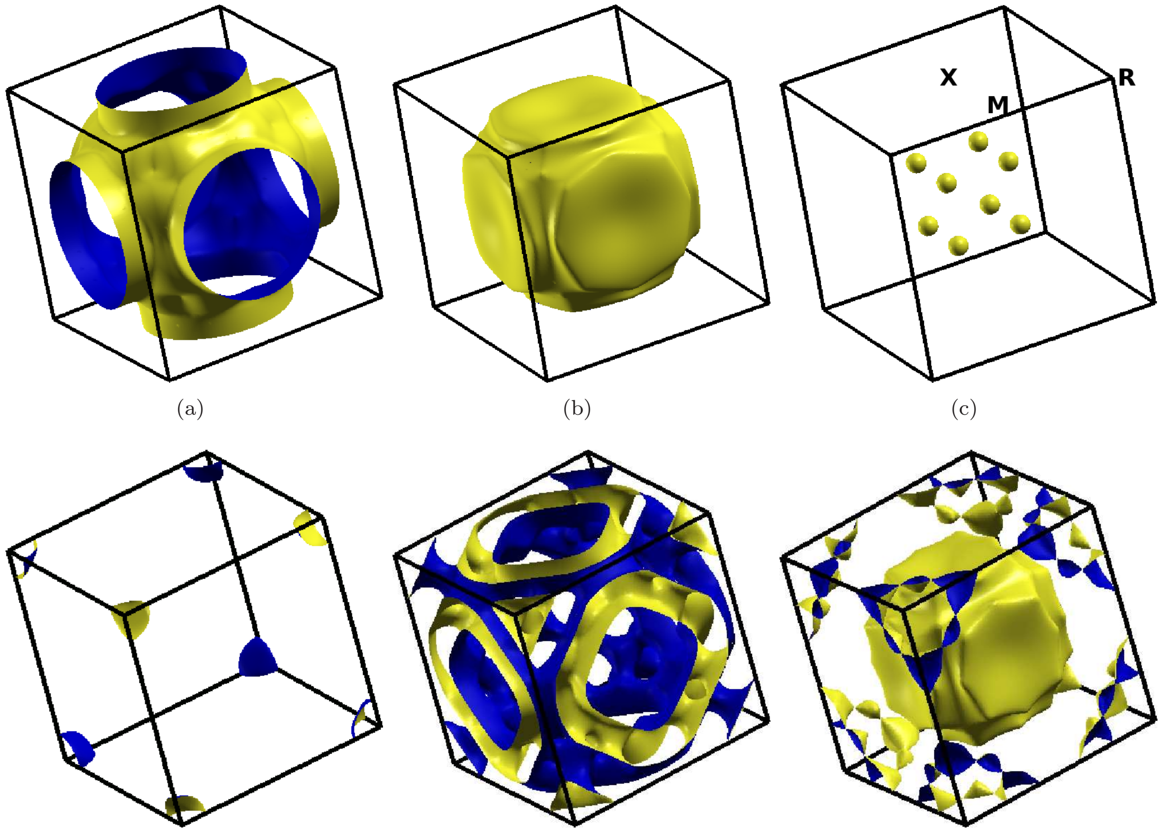

(a) (b) (c)

(d) (e) (f)

Figure 6.3: Fermi surface for (a-c) La_3InO and (d-f) La_3In at $V/V_0 = 1.0$.

But the density of states at the Fermi level ($N(E_F)$) was found to be higher in La_3In [165] ($N(E_F)$ = 7.80 states/eV/f.u.) in comparison with La_3InO ($N(E_F)$ = 2.86 states/eV/f.u.), which might eventually give an indication of the suppression of the T_c in La_3InO which will be discussed little later. Further analyzing the partial density of states of La_3InO from Fig. 6.4 (b), we find the major contribution to stem from La '*d*' along with the hybridization of the In '*p*' and O '*p*' states at the Fermi level. In addition we could also see the Fermi level (E_F) lying close to a peak in the case of La '*d*' and O '*p*' orbital, whereas the E_F falls on pseudogap of In '*p*' orbital. In contrast for La_3In, the E_F lies close to the peak for both La '*d*' and In '*p*' orbital and is well evident from the Fig. 6.4 (c). So the extent of hybridization of In '*p*' with La '*d*' is reduced in the case of La_3InO, whereas there exist a pronounced hybridization between La '*d*' and O '*p*', which brings the role of O in La_3InO. Next we turn our discussion towards comparing La_3InN and La_3InO. As we move from N to O, the band gets filled and is seen in the band structure and FS, which we have presented so far. Now if we compare these compounds from the projected density of states, we could see the Fermi level to fall exactly on the pseudogap in the case of La_3InN and it is clearly evident from the La '*d*' and N

'p' states in Fig. 6.4 (a). The extent of hybridization between La 'd' and In 'p' is again found to be lesser similar to La_3InO. The $N(E_F)$ for La_3InN is found to be 2.55 states/eV/f.u., which is also lesser than both La_3In and La_3InO indicating the T_c to be lesser in comparison with both La_3In and La_3InO. This decrease in T_c in La_3InN when compared with La_3InO can further be understood from the phonon frequency which are discussed in the subsequent section. Our calculated $N(E_F)$ for La_3InN agree well with the reported value of 2.6 states/eV/f.u. [70].

More interestingly we have observed a FS topology change under compression in the case of La_3InO, whereas the topology is found to remain unaltered under compression in La_3InN. In the case of La_3InO we find three surfaces to appear under compression around $V/V_0 = 0.8$ at R point similar to La_3InN (Fig. 6.5 (a-c)), due to the upward movement of the band and an extra electron pocket appear along M-Γ direction in the last FS due to the downward shift of the band and the corresponding Fermi surface is shown in Fig. 6.5 (d). This observed difference between La_3InN and La_3InO is mainly due to the non-monotonic variation of $N(E_F)$ only in La_3InO as shown in Fig. 6.6, whereas we find the $N(E_F)$ to vary linearly with compression in the case of La_3InN. In addition we can observe the sudden increase in density of states at V/V_0=0.8 in La_3InO where we have also found three extra hole pocket (Fig. 6.5 (a-c)) and an additional electron sheet in the last surface to appear (Fig. 6.5 (d)). The non-monotonic behaviour of density of states in La_3InO might also reflect on the superconducting transition temperature, T_c in accordance with Makarov et. al [19], where authors have correlated theoretically the variation of $N(E_F)$ with T_c, and we will discuss the same in detail in next section. Overall we have seen the bands to move up for La_3InN under compression and in the case of La_3InO simultaneous upward and downward shifts of the bands are observed.

6.3.2 Superconductivity and vibrational properties

From the $N(E_F)$, we may calculate the Sommerfeld coefficient of specific heat, (γ) and the values are reported in Table-6.1. From the γ values one may expect T_c to be higher in La_3InO in comparison with La_3InN. From the Eliashberg function we have calculated the electron-phonon coupling constant, λ_{ep} and having calculated the λ_{ep} we estimate the T_c of both the compounds by using Allen-Dynes formula [43] and the values are reported in Table-6.1 along with the calculated $N(E_F)$. The dimensionless μ^*, the Coulomb pseudopotential used in our calculation for all the compounds is 0.1. The calculated averaged phonon frequency ω_{ln} for both the compounds along with La_3In is also reported in Table-6.1.

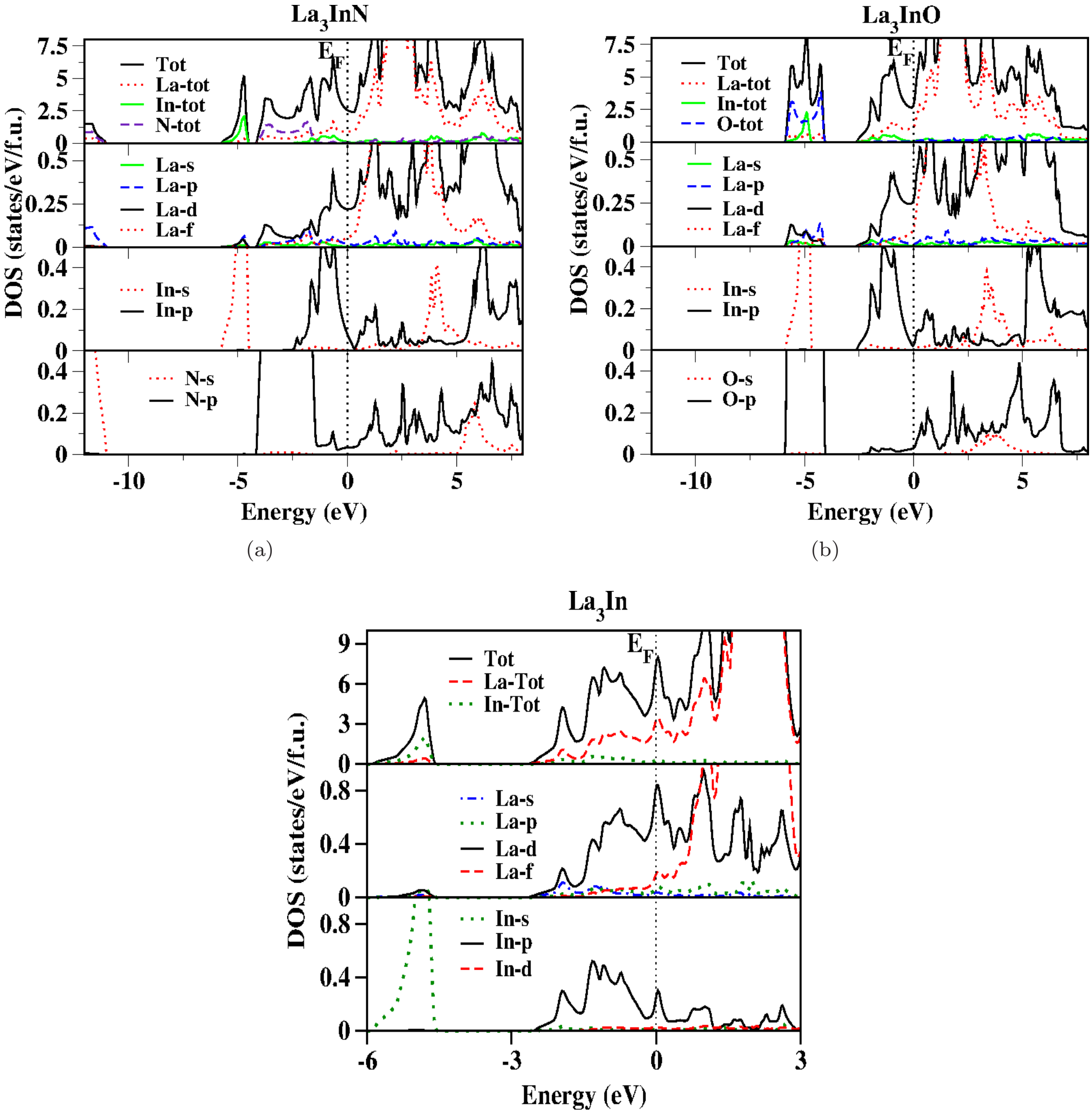

(a)

(b)

(c)

Figure 6.4: Total and partial density of states for (a) La$_3$InN, (b) La$_3$InO and (c) La$_3$In, at V/V$_0$=1.0.

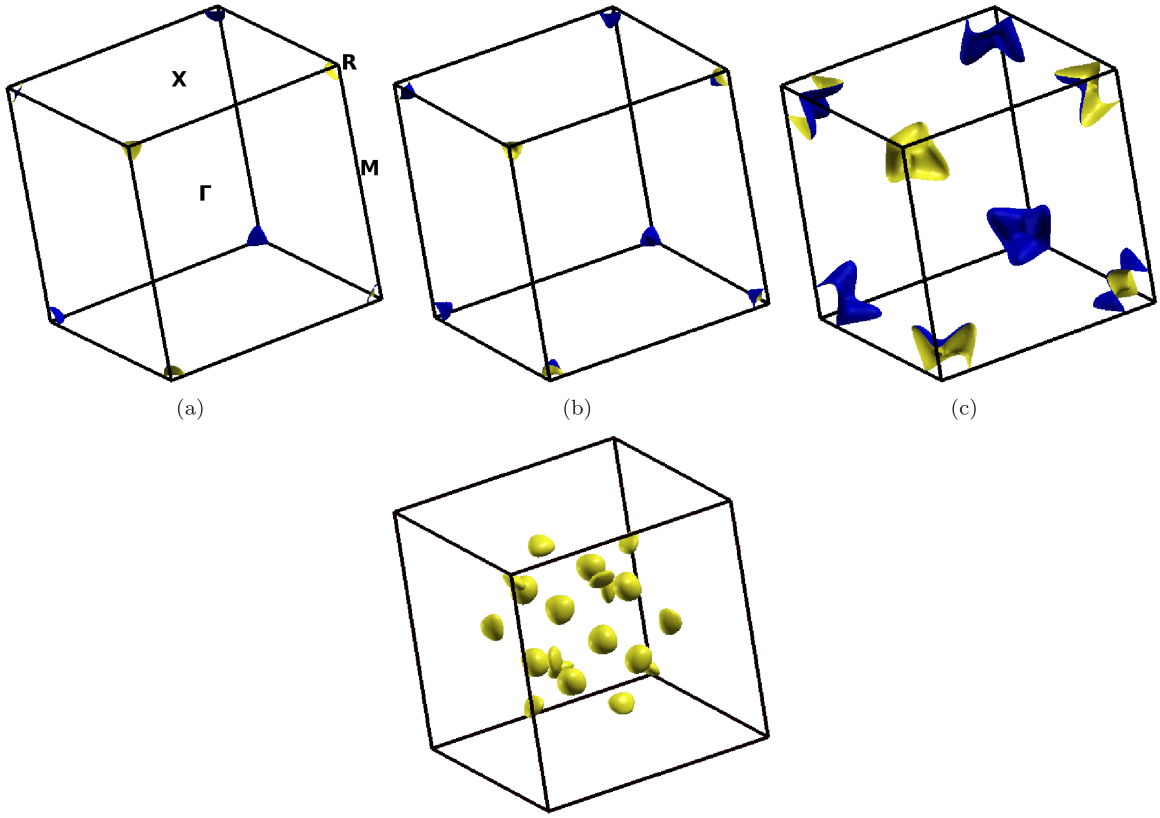

(a) (b) (c)

(d)

Figure 6.5: Fermi surface of La_3InO at V/V_0=0.8. The first three surface (a-c) topology is similar to the FS topology of La_3InN at ambient (Fig. 6.2(a-c)). (d) An extra electron sheet appears along M-Γ direction.

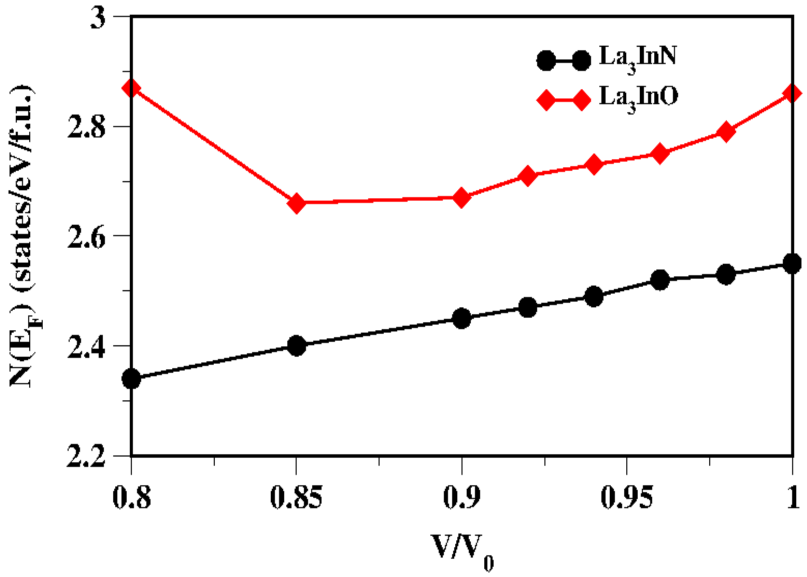

Figure 6.6: Variation of density of states at Fermi level, $N(E_F)$ under compression for La_3InZ (Z = N, O).

Table 6.1: Calculated density of states at the Fermi level, $N(E_F)$ (in states per eV per formula unit, evaluated at the experimental equilibrium volumes), together with derived Sommerfeld coefficient of specific heat, γ, averaged phonon frequency, ω_{ln}, electron phonon coupling constant, λ_{ep} and superconducting transition temperature, T_c for La_3InZ (Z = N, O) and La_3In.

Compounds		$N(E_F)$	γ (mJ/mole K^2)	$\omega_{ln}(cm^{-1})$	λ_{ep}	T_c (K)
La_3InN	This work	2.55	6.02	107.97	0.37	0.44
	Others[a]	2.6				-
La_3InO	This work	2.86	6.74	98.29	0.62	3.77
	Expt.					10[b]
La_3In	This work	7.8	18.40	62.7	0.97	6.36

a: Ref. [70] b: Ref. [68].

From our calculated values we find T_c of La_3InO to be higher than La_3InN with higher electron-phonon coupling constant, λ_{ep} and find this trend to agree well with the calculated $N(E_F)$. Our calculated value of T_c is comparatively lesser when compared to the experimental value [68] in the case of La_3InO and this might be due to the polycrystalline or non-stoichiometric nature of the sample [160, 166]. Unfortunately there are no other theoretical values available for comparing the results of these studied compounds, whereas the trend of our calculated T_c is same as in Ref. [68], where the authors have reported T_c to below 2 K for La_3InN and above 2 K in the case of La_3InO. Again when we compare La_3In with the presently studied compounds we find the calculated T_c value of La_3In (T_c = 6.36 K) to be higher in comparison with La_3InZ (Z = N, O), with higher electron-phonon coupling constant (λ_{ep} = 0.97), as evident from the reported values in Table-6.1 and it contradicts the experimental finding where the authors have reported the T_c of La_3In and La_3InO to be same [63, 68] and we try to justify the same from the calculated phonon dispersion relations as discussed below.

We have plotted the phonon-dispersion in Fig. 6.7 at ambient for both the studied compounds La_3InN and La_3InO along with La_3In. From the figure we can see all the phonon modes to have positive frequency in all high symmetry directions, which ultimately provides the confirmation towards the dynamical stability of these compounds. Again we find the phonon frequency to be higher in La_3InN than in La_3InO. The lower mass in the case of the La_3InN may be the reason for the phonon mode to be higher in frequency when compared with La_3InO.

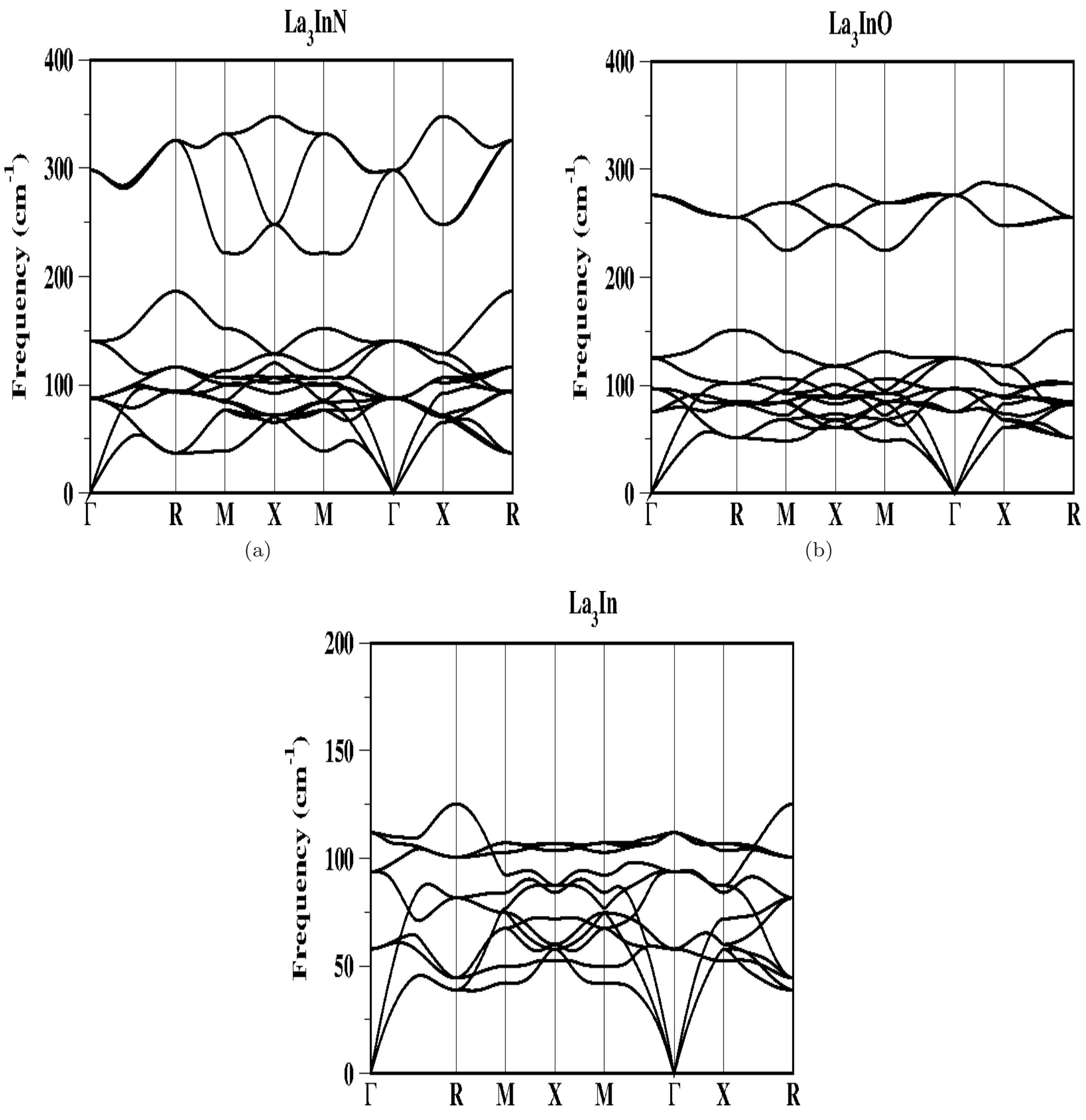

(a)

(b)

(c)

Figure 6.7: Phonon dispersion plots for (a) La$_3$InN, (b) La$_3$InO and (c) La$_3$In at V/V$_0$=1.0.

Table 6.2: Zone center phonon modes for La$_3$InZ (Z = N, O) and La$_3$In, as calculated with the experimental volume. All the modes are triply degenerate. The frequency are in cm^{-1}.

Parameters	T_{1u}	T_{1u}	T_{2u}	T_{1u}	T_{1u}
La$_3$InN	0	87.2	87.4	140.4	298.2
La$_3$InO	0	66.0	97.0	125.3	274.2
Parameters	T_{1u}	T_{2u}	$T1u$	T_{1u}	-
La$_3$In	0	57.8	94.8	112.0	

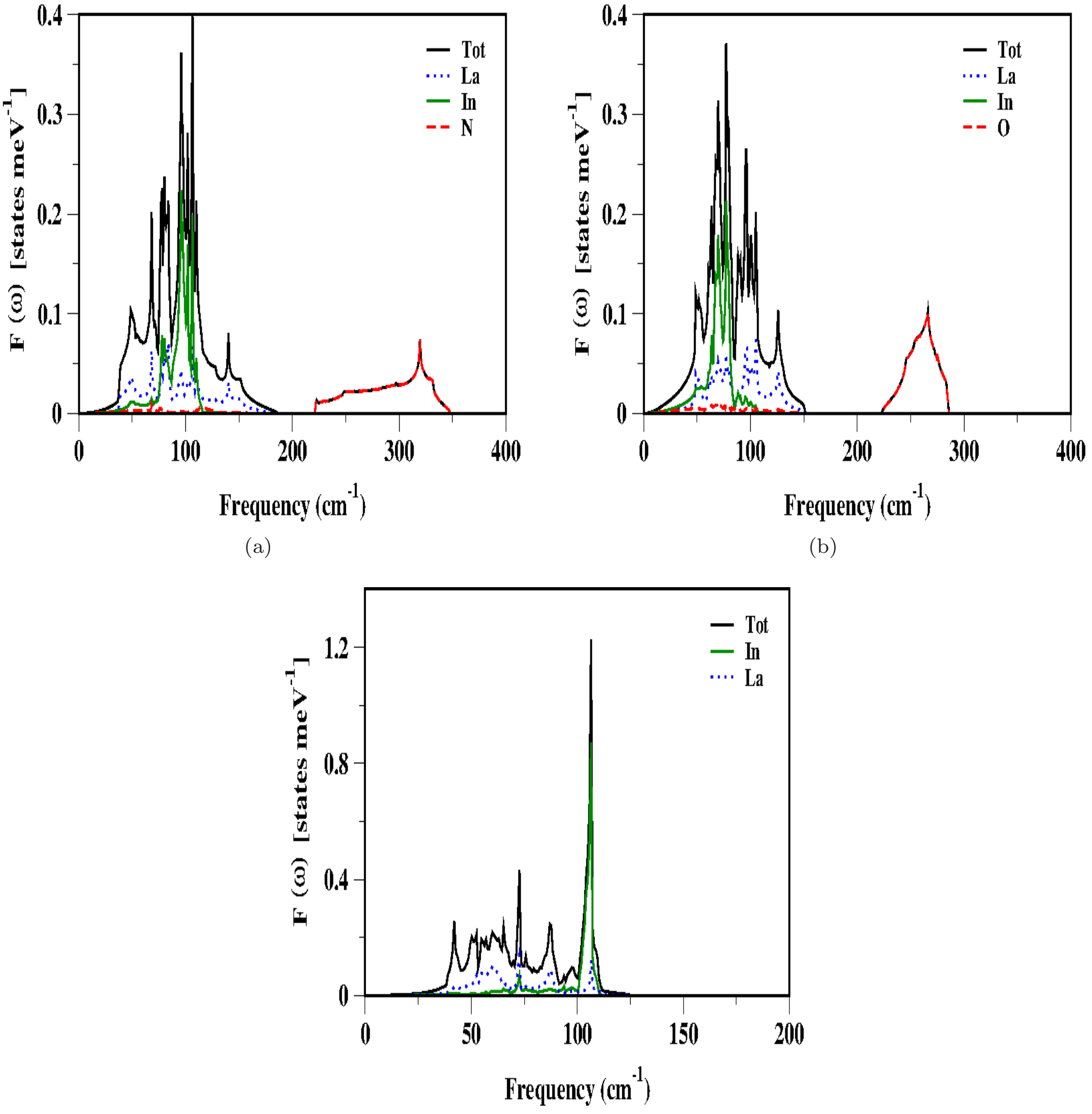

(a)

(b)

(c)

Figure 6.8: Phonon density of states, (F(ω)) for (a) La_3InN, (b) La_3InO and (c) La_3In at V/V_0=1.0.

If we compare La_3In and La_3InO, we find the phonon modes to soften in the case of La_3In in comparison with La_3InO. The hardening of the phonon modes in La_3InO might be reducing the electron-phonon coupling constant in the case of La_3InO in comparison with La_3In leading to the reduction in superconducting transition temperature of La_3InO. The hardening of the phonon modes are mainly due to the presence of the O atom and is well evident from the phonon density of states, (F(ω)) (PDOS) in Fig. 6.8, where we can see the contribution at higher frequency regions to arise mainly from the O(N) atom. In addition we have calculated the zone center phonon frequency for both La_3InN and La_3InO along with La_3In and the values are reported in Table-6.2. For a crystalline solid there are $3N$ number of modes, where N is the number of atoms in primitive cell and out of $3N$ modes, three are acoustic modes and $3N$-3 are optical modes. In our studied compounds La_3InZ (Z = N, O) and La_3In we have total 15 and 12 numbers of modes, respectively and all are triply degenerate at zone center. When we compare La_3InN with La_3InO, we could see all the phonon modes except the T_{2u} mode to soften at zone center in the case of La_3InO and is well evident from the Table-6.2. Altogether the hardening of the phonon modes in the presence of the Z (Z = N, O) atom in the body centered position of the cube play a role in decreasing the electron-phonon coupling constant eventually leading to a lower T_c in La_3InZ as compared to La_3In.

Apart from this we have also calculated the T_c under compression for La_3InO and find T_c to decrease initially and then increase as shown in Fig. 6.9 and agree well with the observed trend of our calculated $N(E_F)$ as shown in Fig. 6.6. More interestingly we can see $N(E_F)$ as well as T_c to vary non-monotonically and well support the FS topology change. Previously Huang et. al [81] have also found the same anomaly in T_c in the case of $LaSn_3$ and suspected a FS topology change. In our previous chapters-3, 4, 5 we have shown the same for a series of compounds AX_3 (A = La. Y; X = In, Tl, Pb, Sn), La_3X (X = In, Sn). Recently the correlation between FS topology change and variation of T_c was shown by Chia-Hui Lin et. al [167]. Overall in the case of La_3InO, we find all phonon modes to harden under compression in all high symmetry direction. In contrast to La_3InO we have seen T_c to increase in the case of La_3In under compression and also find the lower frequency modes in particular at R and M point to soften leading to the increase of T_c and it is well explained in chapter-5. The observed sudden increase in T_c under compression in La_3InO can be attributed to the appearance of new hole pocket as well as electron pocket at $V/V_0 = 0.8$ (Fig. 6.5, the pressure equivalent to this compression is 15 GPa.), leading to an increase in $N(E_F)$, as shown in Fig. 6.6.

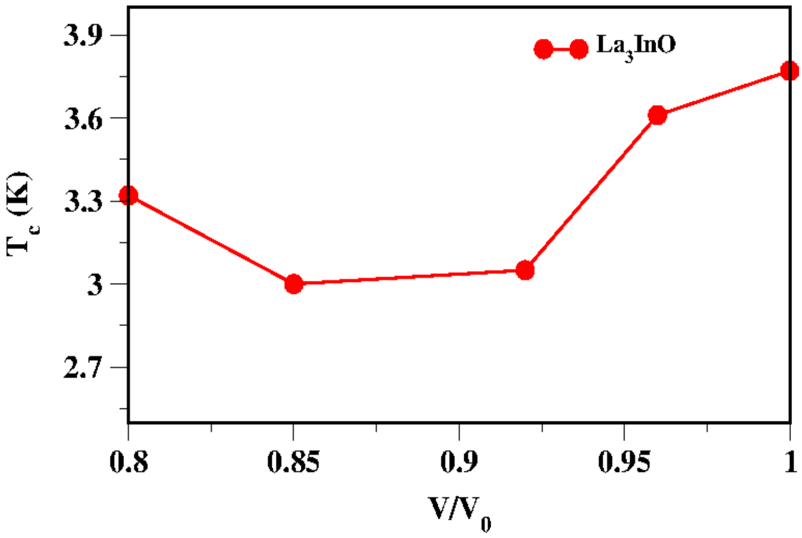

Figure 6.9: Superconducting transition temperature, T_c under compression for La$_3$InO.

6.3.3 Elastic constants and mechanical properties

For the cubic system there are three elastic constants C_{11}, C_{12} and C_{44} [123, 124]. These elastic constants give the information about the mechanical behaviour, stability and stiffness of the crystal. We have calculated these elastic constants and the related mechanical properties for all the studied compounds at the experimental equilibrium volumes and are listed in Table-6.3. There are no other experimental or theoretical results available for comparison. Both the studied compounds are found to be mechanically stable by satisfying the Born's [168] stability criteria $C_{11} > C_{12}$, $C_{44} > 0$, and $C_{11} + 2C_{12} > 0$.The calculated bulk modulus, B of La$_3$InZ compounds are reported in Table-6.3. Hill's [126] shear modulus G_H (which is the arithmetic mean of the Reuss [127] and Voigt [128] approximations), Young's modulus E, the Poisson ratio σ and several related elastic properties can be calculated from these elastic constants C_{11}, C_{12} and C_{44} and the formulas are given in chapter-3 in equation-(3.1-3.5). Ductile and brittle nature of the compound can be estimated from the Pugh ratio [138], ratio between the shear modulus and the bulk modulus G_H/B. According to Pugh, the value less than 0.57 indicates the ductile nature and the value greater than 0.57 is the indication of the brittle nature of the compound. From our calculated values as reported in the Table-6.3, we can identify La$_3$InN to be brittle and La$_3$InO is in the border line of ductile and brittle nature. The brittle and ductile nature of these compounds are also reported in Ref. [68] and agree well with our calculation. The positive/negative Cauchy pressure values ($C_p = C_{12} - C_{44} > 0$) is also used to clarify the ductile/brittle nature of the compounds and our calculated values again support our discussion. From the Table-6.3 we can see that the addition of N in La$_3$In makes the compound

Table 6.3: Elastic constants and derived quantities for La_3InZ (Z = N, O) and La_3In, as calculated with the experimental equilibrium volume. A is the anisotropy factor, $A = 2C_{44}/(C_{11} - C_{12})$, the degree of the elastic anisotropy, $A^* = 3(A-1)^2/[3(A-1)^2 + 25A)]$ (Ref. [149]), B is the Bulk modulus and $C_p = C_{12} - C_{44}$ is the Cauchy pressure.

Parameters	La_3InN	La_3InO	La_3In
C_{11} (GPa)	134.63	117.68	54.2
C_{12} (GPa)	38.14	38.50	31.8
C_{44} (GPa)	42.56	35.89	21.9
A	0.88	0.91	1.96
$A^*(\%)$	0.5	0.3	5.3
G_H (GPa)	44.75	37.33	16.7
B	70.30	51.96	39.3
E (GPa)	110.75	93.96	43.9
σ	0.24	0.26	0.31
G_H/B	0.64	0.58	0.42
C_p (GPa)	-4.41	2.61	9.9
v_m (km/s)	2.85	2.59	1.77
Θ_D (K)	283.64	258.94	163.9

brittle in nature, whereas the ductile nature of La_3In remains almost the same with the addition of O. This again well supports our phonon dispersion plots, where we find phonon frequencies of La_3InN to be higher in comparison with La_3InO and La_3In. Another important parameter of a material is the elastic anisotropy $A = 2C_{44}/(C_{11} - C_{12})$ (Ref. [149]). The value of A smaller or greater than unity measures the degree of elastic anisotropy of the material. The calculated values of A indicate both the La_3InZ (Z = N, O) compounds to be elastically anisotropic. To compare, the relative magnitude of the elastic anisotropy, A^* calculated in percent are tabulated in Table-6.3. It shows that anisotropy is more in O containing compound in comparison with the N containing compound.

In addition to this we have also calculated the Debye temperature of all La_3InZ (Z = N, O) compounds and are tabulated in Table-6.3. Debye temperature is a fundamental physical parameter which is closely related to many physical properties such as elastic constants, specific heat and melting temperature. Unfortunately, there are no other values available for comparison. Comparing the elastic properties of both La_3InN and La_3InO compounds, we find the elastic and the related mechanical behavior of the N, O containing compound to be different and our results agree well the experimental finding [68], where the authors also reported La_3InN to be brittle in nature and La_3InO as ductile.

6.4 Conclusion

In summary, our *ab initio* study of electronic structure calculations of La_3InZ (Z= N, O) conclude that, when Z atom is added to the body center of La_3In, the hybridizing effect between La 'd' and In 'p' orbital gets reduced in La_3InZ in comparison with La_3In. The Fermi surface topology change is observed under compression for La_3InO but not in La_3InN, which is attributed to the non-monotonic variation of the density of states in La_3InO and also gives rise to a non-linear variation of T_c. From the phonon dispersion plots we have shown both the compounds to be dynamically stable. From the calculated superconducting transition temperature we find a suppression of T_c in La_3InZ due to the addition of Z (N, O) atom in La_3In, which is mainly due to the hardening of the phonon modes. Again T_c is found to be less than 2 K for La_3InN and above 2 K in the case of La_3InO, which also agree well with the experimental trend. From the mechanical properties we find $La_3InN(O)$ to be brittle(ductile) in nature in agreement with the experimental reports.

Chapter 7

Skutterudites $LaRu_4X_{12}$ (X = P, As, Sb) under pressure

Ab initio results on the band structure, density of states and Fermi surface (FS) properties of $LaRu_4X_{12}$ (X = P, As, Sb) are presented at ambient pressure as well as under compression. The analysis of density of states reveals the major contribution at the Fermi level to be mainly from the Ru '*d*' and X '*p*' states. We have a complicated Fermi surface with both electron and hole character for all the three compounds which is derived mainly from the Ru '*d*' and X '*p*' states. There is also a simpler FS with hole character derived from the P 'p_z' orbital for $LaRu_4P_{12}$ and Ru 'd_{z^2}' orbital in the case of As and Sb containing compounds. More interestingly, Fermi surface nesting feature is observed only in the case of the $LaRu_4P_{12}$. Under compression, we observe the topology of the complicated FS sheet of $LaRu_4As_{12}$ to change around $V/V_0 = 0.85$, leading to a behaviour similar to that of a multiband superconductor and in addition we have two more hole pockets centered around Γ at $V/V_0 = 0.8$ for the same compound. Apart from this we find the hole pocket to vanish at $V/V_0 = 0.8$ in the case of $LaRu_4Sb_{12}$ and the opening of the complicated FS sheet gets reduced. The de Haas van Alphen (dHvA) calculation shows the number of extremal orbits in the complicated sheet to change in As and Sb containing compounds under compression, where we also observe the FS topology to change.

7.1 Introduction

Rare-earth filled skutterudites with the general formula RT_4X_{12}, have attracted much attention due to their various unique physical properties such as occurrence of a pressure-induced superconducting phase in $PrRu_4P_{12}$ [169], multiple ordered state in $SmRu_4P_{12}$ [170], magnetic field independent heavy fermion state in $SmOs_4P_{12}$ [171], metal-insulator transition in $PrFe_4P_{12}$ [172] and in $SmRu_4P_{12}$ [170], heavy-fermion superconductivity in $PrOs_4Sb_{12}$ [173, 174, 175] and highly promising thermoelectric properties in some others [176, 177, 178]. The interesting point is that most of the above properties of these compounds are certainly linked with the Fermi surface (FS) topology. It is to be noticed that the metal-insulator transition occurring in $PrRu_4P_{12}$ [72] is associated with FS nesting with 2π/a(1,0,0) as the nesting vector q. Numerous studies have been performed to explain Fermi surface topology of isostructural $LaRu_4P_{12}$ [72] and the authors have found FS nesting with $\vec{q}$ = 2π/a(1, 0, 0). From the above discussion, one can expect a similar metal-insulator transition in $LaRu_4P_{12}$. However, resistivity and specific-heat measurements show no such transition above the superconducting transition temperature (T_c) [77]. Our present calculations on $LaRu_4P_{12}$ also exclude such type of transition which is consistent with the available reports. Apart from this, recently, the experimental as well as theoretical calculation on superconductivity and the vibration properties of some As and P containing compouds of the form LaT_4X_{12} (T = Fe, Ru, Os; X = As, Sb) and LaT_4P_{12} (T = Fe, Ru) are reported [179, 85]. From these experimental study it was found that the T_c decreases under pressure in the case of $LaRu_4P_{12}$ and in our present calculation we try to correlate and predict this decreasing behaviour of T_c under pressure from the electronic structure calculation [85].

Fermi surface studies are also available for $LaOs_4Sb_{12}$ [180] and $LaOs_4P_{12}$ [181], but the authors have not found any nesting feature in $LaOs_4Sb_{12}$. Experimentally de Haas van Alphen (dHvA) studies are available for $LaFe_4P_{12}$ [74], $LaRu_4P_{12}$ [75] and $CeRu_4Sb_{12}$ [76], where the authors have found the FS topology of $CeRu_4Sb_{12}$ and $LaRu_4Sb_{12}$ to be different due to the presence of strong electron correlation in the former compound. One of the characteristic features of some of the filled skutterudites is multi-band superconductivity. Recently, Bochenek et. al [73] have reported multiple-gap superconducting behaviour in $LaRu_4As_{12}$ from the observed nonlinear magnetic-field dependence of the specific heat in the zero-temperature limit, a positive curvature of the upper critical field in the vicinity of T_c and a deviation of the electronic specific heat from the one-gap model. The origin of multiband effect was reported in $PrRu_4As_{12}$ [182, 183] by comparing it with the iso-structural compound $LaRu_4As_{12}$. Apart from these the position parameters u and v of the X atom also play a role in determining the electronic and various physical properties [184]. Recently Uchiumi et. al [77] have reported the superconducting transition temperature of $LaRu_4X_{12}$ with X = P, As, Sb to be 7.2, 10.3 and 2.8 K respectively. Among all the rare earth filled skutterudite compounds $LaRu_4As_{12}$ is having the highest superconducting transition temperature of 10.3 K [185, 77]. From the available literature on these skutterudites, it is quite evident that the FS topology studies on these compounds are mandatory and highly essential to have a complete understanding of the various physical properties of these compounds. So in the present study, we have analysed the FS topology of the $LaRu_4X_{12}$ with X = P, As, Sb at ambient as well as under compression. Though there are a few reports available for $LaRu_4P_{12}$ [186], at ambient, high pressure studies are lacking for all the compounds which are presented quite elaborately in this work. The rest of the chapter is organized as follows. The computational details regarding our calculations are presented in section-7.2, section-7.3 includes the results and discussion of results pertaining to ambient pressure and under compression. Finally, section-7.4 concludes the chapter.

7.2 Method of calculation

First-principles calculations were performed using the full-potential linearized augmented plane wave (FP-LAPW) method as implemented in the WIEN2*k* [101] code. For the exchange and correlation terms in the electron-electron interaction we have used the generalized gradient approximation (GGA) of Perdew-Burke-Ernzerhof (PBE) [98]. Muffin-tin radii are taken to be 2.5, 2.0, 1.75, 1.85 and 2.2 a.u for La, Ru, P, As and Sb atom respectively. A 30× 30× 30 Monkhorst-Pack grid [120] of k-points has been used for the self-consistent field and density of states calculations. To ensure accurate determination of the Fermi level, we have used a 44× 44 × 44 k-point grid for Fermi surface calculation. The three-dimensional Fermi surface plots were generated with the help of the XCrySDen molecular structure visualisation program [122]. In order to achieve convergence of energy eigen values, the wave functions in the interstitial region were expanded using plane waves with $R_{MT}K_{max}$ = 10 for X = As, Sb and $R_{MT}K_{max}$ = 9 for X = P, where R_{MT} is the Muffin tin radius and the K_{max} gives the magnitude of the largest K vector in the plane-wave expansion. In the interstitial region the charge density and the potential were expanded as a Fourier series with wave vectors up to G_{max} = 9, 12, 10 a.u^{-1} for X = P, As, Sb, respectively. The self-consistent calculations are considered to be converged when the total energy of the system is stable within 10^{-6} Ry. The calculations are carried out for the experimental lattice parameters. In the present study, the experimental volume of

Table 7.1: Calculated atomic position parameter u and v for $LaRu_4X_{12}$ with X = P, As, Sb

Compounds		u	v
$LaRu_4P_{12}$	present study	0.3577	0.1444
	Expt[a]	0.3591	0.1428
$LaRu_4As_{12}$	present study	0.3501	0.1503
	Expt[a]	0.3500	0.1470
$LaRu_4Sb_{12}$	present study	0.3418	0.1582
	Expt[a]	0.3400	0.1600

a: Ref. [187]

the system is represented by V_0. Experimental lattice parameters which we have used in our present calculation for $LaRu_4P_{12}$, $LaRu_4As_{12}$ and $LaRu_4Sb_{12}$ are 15.2333 a.u, 16.0812 a.u, and 17.5337 a.u respectively. Calculations were performed with and without spin-orbit coupling (SOC) effect and we have not noticed any pronounced SOC effect in the vicinity of the Fermi level and hence proceeded with our subsequent studies excluding the SOC effect. The de Haas van Alphen effect is calculated from the SKEAF programme [106].

7.3 Results and discussions

7.3.1 Ground-state properties

The filled skutterudites of the form RT_4X_{12} have body centred cubic structure with space group $Im\bar{3}$ (no. 204), where R is a rare-earth element, T is a transition element and X is a pnictogen. The crystal structure of the skutterudite is given in Fig. 7.1 (a). The atomic position for R (R = La) is (0.0, 0.0, 0.0), T (T = Ru) occupies the position (0.25, 0.25, 0.25) and X (X = P, As, Sb) is present at (0.0, u, v). We have relaxed the system to get the optimized value of (u, v) for all the investigated $LaRu_4X_{12}$ compounds. The experimental and calculated theoretical u and v positional parameters for X = P, As, Sb are tabulated in Table-7.1. Our calculated values agree well with the experiment. The rest of the calculations are performed with the experimental lattice parameter along with the theoretical optimized atomic positions.

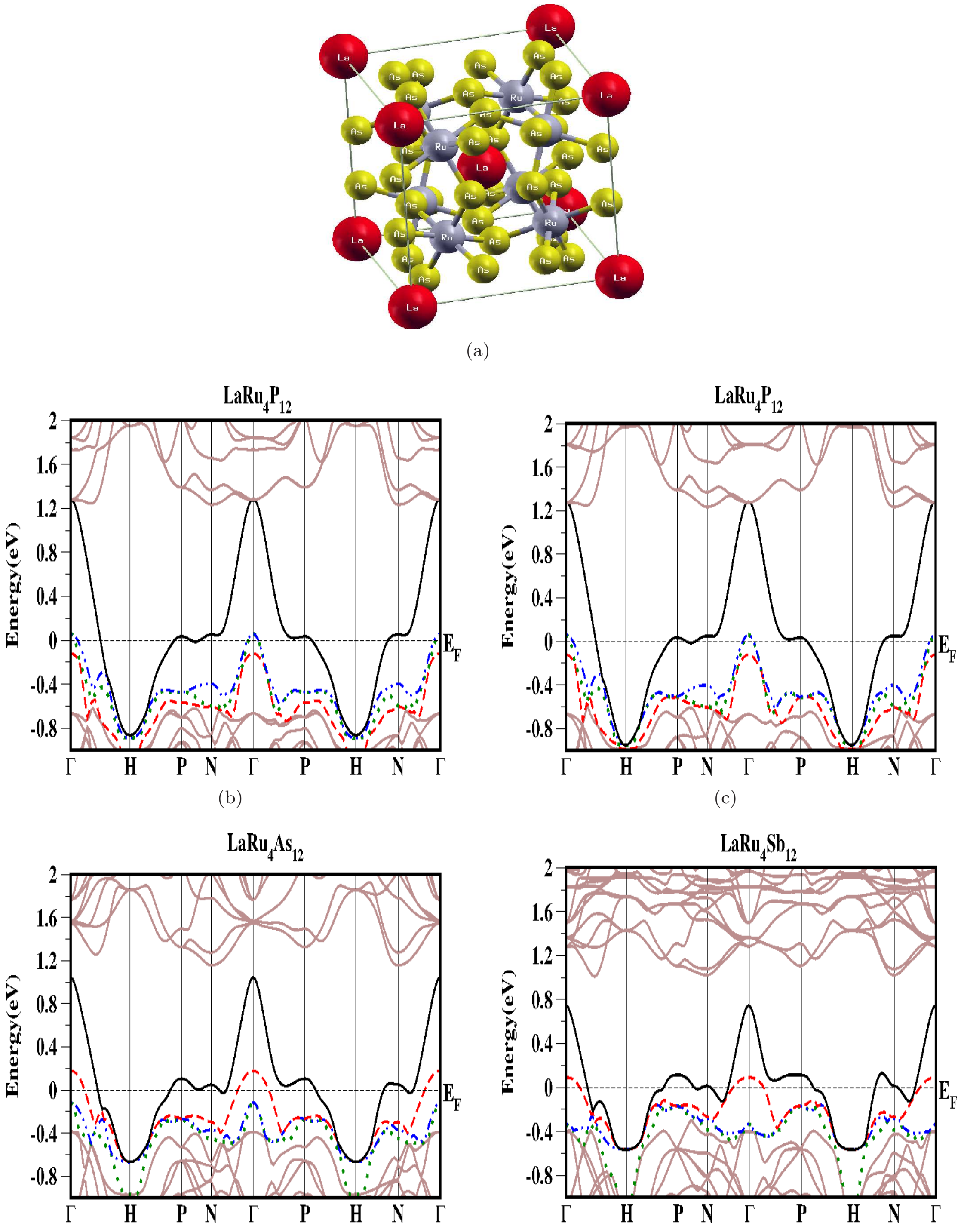

(a)

(b)

(c)

(d)

(e)

Figure 7.1: Crystal structure of $LaRu_4As_{12}$. Band structure of (b) $LaRu_4P_{12}$ with spin-orbit coupling (SOC) and (c, d, e) for $LaRu_4X_{12}$ with X = P, As, Sb at $V/V_0 = 1.0$ without spin-orbit coupling (SOC). SOC effect in not seen in the vicinity of the Fermi level. The color code used for the plots is for the identification of bands crossing at the Fermi level.

7.3.2 Band structure, density of states and Fermi surface

The band structure calculations were performed with and without spin-orbit coupling for all the three studied compounds $LaRu_4X_{12}$ (X = P, As, Sb) and found the vicinity of the Fermi level to be unaltered and rest of the calculations were carried out without spin-orbit coupling and the corresponding band structure is plotted in Fig. 7.1 along the high symmetry directions. Our calculated band structures agree well with the other available studies [188, 72]. From the band structure plots it is evident that, for $LaRu_4P_{12}$, three bands cross the E_F, whereas in other two compounds only two bands cross the E_F at ambient pressure. For all the three compounds there is a relatively more dispersive conduction band (the band shown in black color in Fig. 7.1) which is of mixed orbital character at various points in the Brillouin zone. To further elucidate the nature of the bands we have plotted *fat bands* for all the compounds in Figs. 7.2-7.4. It can be seen from the figure, that the states in this conduction band are mainly of X 'p_z' character near the Γ point, hybridized X 'p_z', 'p_y' and Ru '$d_{x^2-y^2}$', 'd_{xy}' character mainly dominates near the N point and X 'p_y', 'p_z' with admixture of the Ru 'd_{z^2}' near P point, whereas the occupied states in this band near the H point have an admixture of the Ru '$d_{x^2-y^2}$', 'd_{xy}' and Ru 'd_{xz}', 'd_{yz}' states. Apart from this we have two more sets of bands for these compounds, one is the non-degenerate band (red color band as in Fig. 7.1) mainly derived from the Ru 'd_{z^2}' at Γ point and crossing the E_F in the case of As and Sb containing compounds and possessing hole character, whereas it is below the E_F and completely filled in the case of $LaRu_4P_{12}$. The other set of doubly degenerate bands (blue and green color band in Fig. 7.1) is of X 'p_z' (X = P, As, Sb) character and is again evident from the Figs. 7.2-7.4 and it crosses the E_F only in the case of $LaRu_4P_{12}$ with hole character at the same Γ point, but in the case of As and Sb containing compounds it is below the E_F and completely filled. In addition, to support our discussion we have also calculated the l and m projected density of states as shown in Fig. 7.5.

We have also analysed the contribution at the Fermi level from the different atoms through the partial density of states for these compounds as shown in Fig. 7.5. The density of states at the Fermi level is dominated by the Ru 'd' with admixture of the X 'p' (mainly 'p_y, p_z') orbitals. From the calculated total density of states we find the highest peak at E_F in the case of $LaRu_4As_{12}$, followed by $LaRu_4Sb_{12}$ and $LaRu_4P_{12}$, with density of states at the Fermi level ($N(E_F)$) being 13.56, 11.16, 7.92 states/eV/f.u, respectively which alternatively give rise to the specific heat coefficient, γ, to be 31.96, 26.30, 18.67 mJ/mol K^2, respectively. Our calculated density of states for $LaRu_4P_{12}$ is in excellent agreement with the experimentally reported value of 7.14 states/eV/f.u (0.42 states/eV/atom)

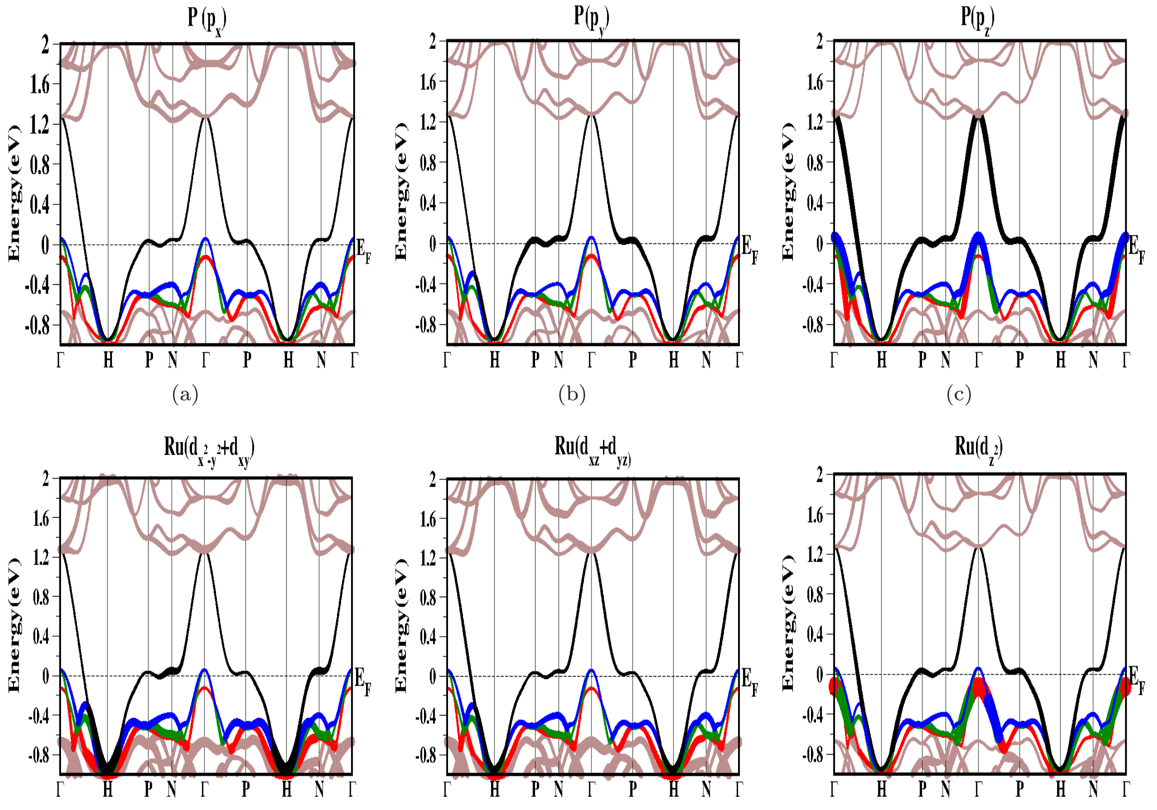

(a) (b) (c)

(d) (e) (f)

Figure 7.2: Fat band of $LaRu_4P_{12}$ at V/V_0= 1.0. The color code used for the plots is for the identification of bands crossing at the Fermi level. The width of the band indicates the weight of each orbital contribution.

[77]. We observe the computed total density of states as well as γ to be higher in $LaRu_4Sb_{12}$ as compared to $LaRu_4P_{12}$ which is suggestive of a larger electron-phonon coupling constant and hence a higher superconducting transition temperature T_c in the case of $LaRu_4Sb_{12}$ in comparison with $LaRu_4P_{12}$. However the trend is reverse for the reported superconducting transition temperature. The experimentally reported values of T_c of $LaRu_4Sb_{12}$ is around 2.8 K [77] which is significantly lower in comparison with 7.2 K of $LaRu_4P_{12}$ [189].

To analyze in more detail the origin of the superconductivity we have calculated the density of states at the Fermi level due to each band that crosses the E_F for all the compounds. From this analysis we observe an unmistakable correlation between the calculated values of $N(E_F)$ corresponding to the more dispersive band (the black color band in Fig. 7.1) and the trend in the values of T_c of all the three compounds investigated here. The calculated value of $N(E_F)_{blackcolorband}$ is found to be 5.56, 8.91 and 7.26 states/eV/f.u for P, As and Sb containing compounds respectively and seems to contribute nearly 65-70 % of the total $N(E_F)$. In the case of As and Sb containing compounds the

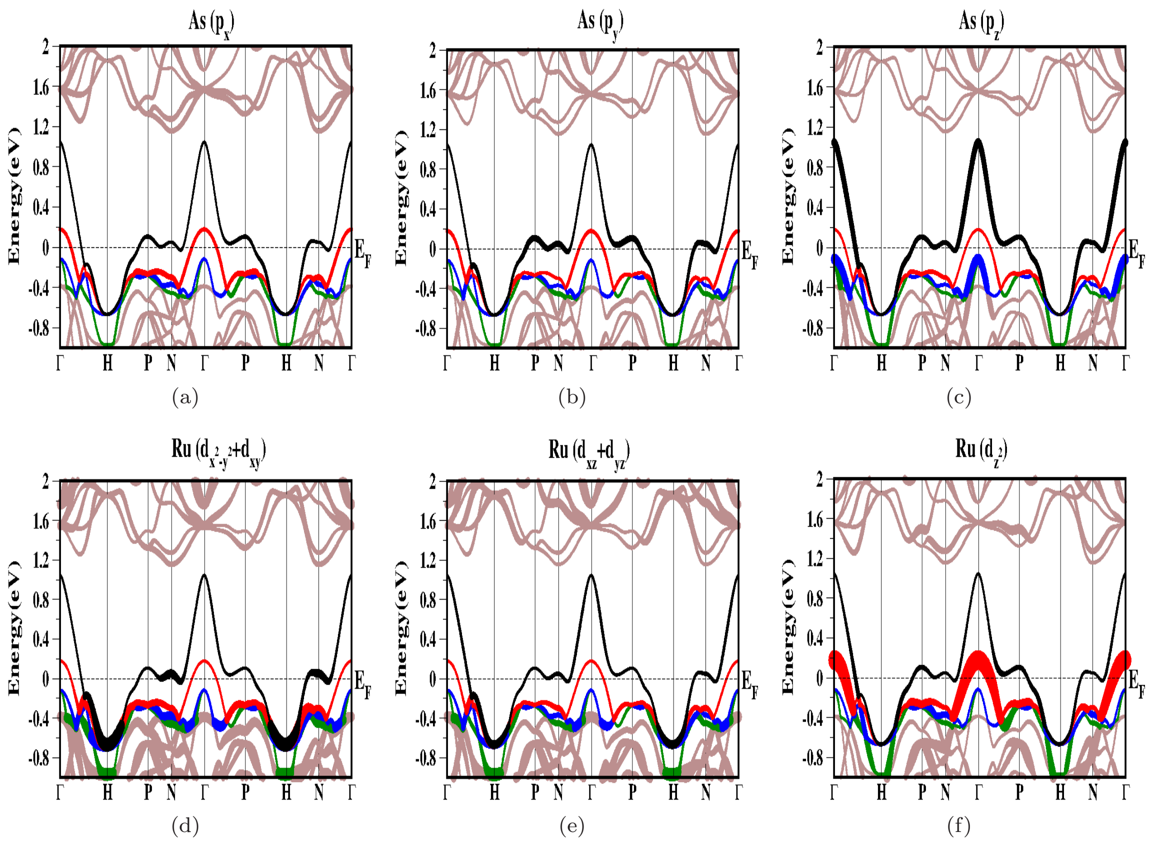

(a) (b) (c)

(d) (e) (f)

Figure 7.3: Fat band of LaRu$_4$As$_{12}$ at V/V$_0$= 1.0. The color code used for the plots is for the identification of bands crossing at the Fermi level. The width of the band indicates the weight of each orbital contribution.

contribution due to the non-degenerate (red color) band (Fig. 7.1) may also play a role in the occurrence of superconductivity as we find the $N(E_F)$ due to this band to be 0.4 and 0.66 states/eV/f.u, respectively and these two compounds might behave like a two band superconductor. On the other hand, the contribution from the doubly degenerate bands (blue and green band) is found to be 0.08 and 0.03 states/eV/f.u, respectively only in the case of LaRu$_4$P$_{12}$ which is negligible in comparison with the black color band in this compound, and hence this compound might behave as a single band superconductor. At the same time we also find the $N(E_F)$ for the black color band in the case of LaRu$_4$As$_{12}$ to be highest, and the experimentally reported values of T_c of this compound to be the highest [77]. This is in agreement with the conjecture that superconductivity arises primarily from this band, of hybridized X 'p' and Ru 'd' orbital character, in all these compounds.

Apart from this, we have studied the Fermi surface for all the compounds and find two hole pockets at Γ point in the case of LaRu$_4$P$_{12}$, as presented in Fig. 7.6 (a,b) and are mainly of P 'p_z' orbital character whereas only one hole pocket is visualised at Γ point for LaRu$_4$As$_{12}$ (Fig. 7.7 (a))

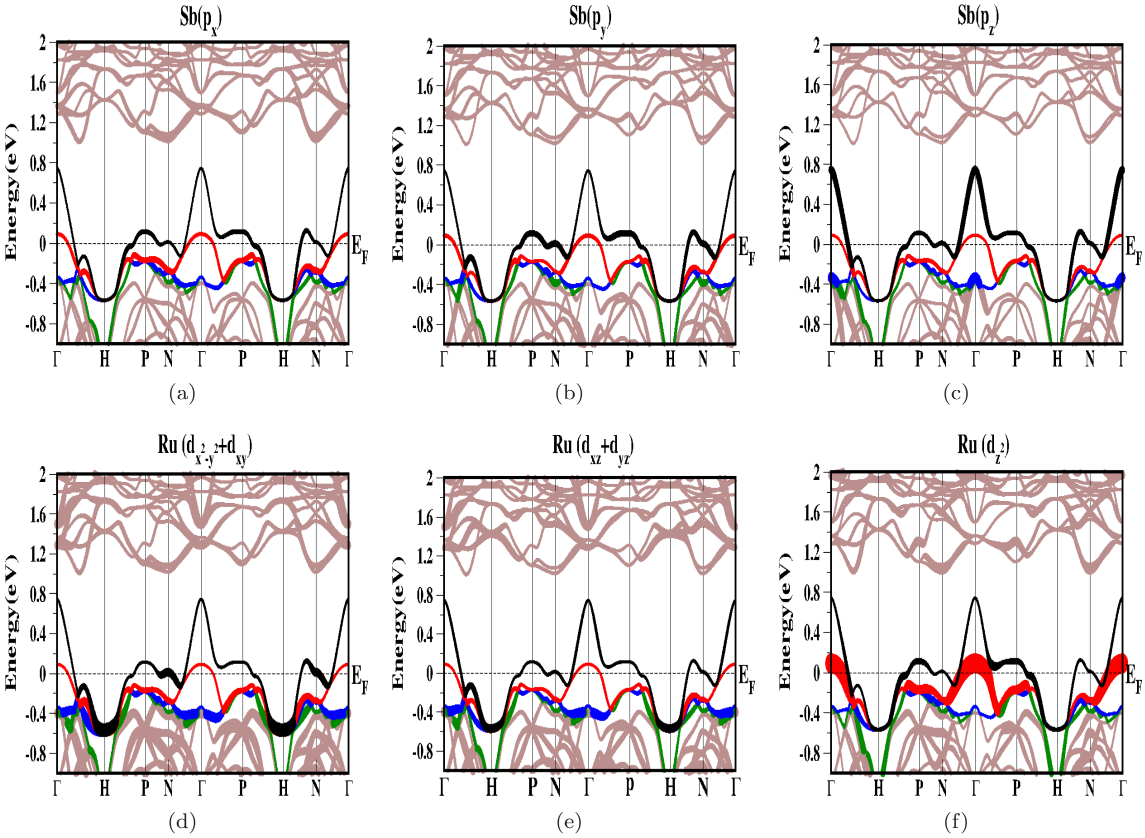

(a) (b) (c)

(d) (e) (f)

Figure 7.4: Fat band of $LaRu_4Sb_{12}$ at V/V_0= 1.0. The color code used for the plots is for the identification of bands crossing at the Fermi level. The width of the band indicates the weight of each orbital contribution.

and $LaRu_4Sb_{12}$ (Fig. 7.7 (c)) and is mainly of Ru 'd_{z^2}' orbital character as discussed above. When we compare the hole pockets of all the three compounds, we can see a completely spherical surface in the case of As and Sb containing compounds, which mainly derive from Ru 'd_{z^2}' and the hole surface of P containing compound is slightly elongated and is derived from the P 'p_z' orbital. Our calculated Fermi surfaces compare well with the previous study [72]. In addition to this, we have a complicated FS sheet due to the other band (see solid black color band in Fig. 7.1) which is more dispersive and cross the E_F at several high symmetry points for all the compounds, but the topology of this complicated surface is not the same for all the compounds due to the hybridisation of X (X = P, As, Sb) with Ru 'd' orbital and is confirmed from the fat bands presented earlier (Fig. 7.2-7.4). In the case of the $LaRu_4P_{12}$, the complicated FS (Fig. 7.6 (c)) consists of a open hole pocket around P point in the FS and it connects to the remaining surface, resulting in the nesting property along PN direction with nesting vector q to be (1, 0, 0), whereas the same nesting property is not expected in the case of the $LaRu_4As_{12}$ and $LaRu_4Sb_{12}$, as we have not seen the same open hole sheet around

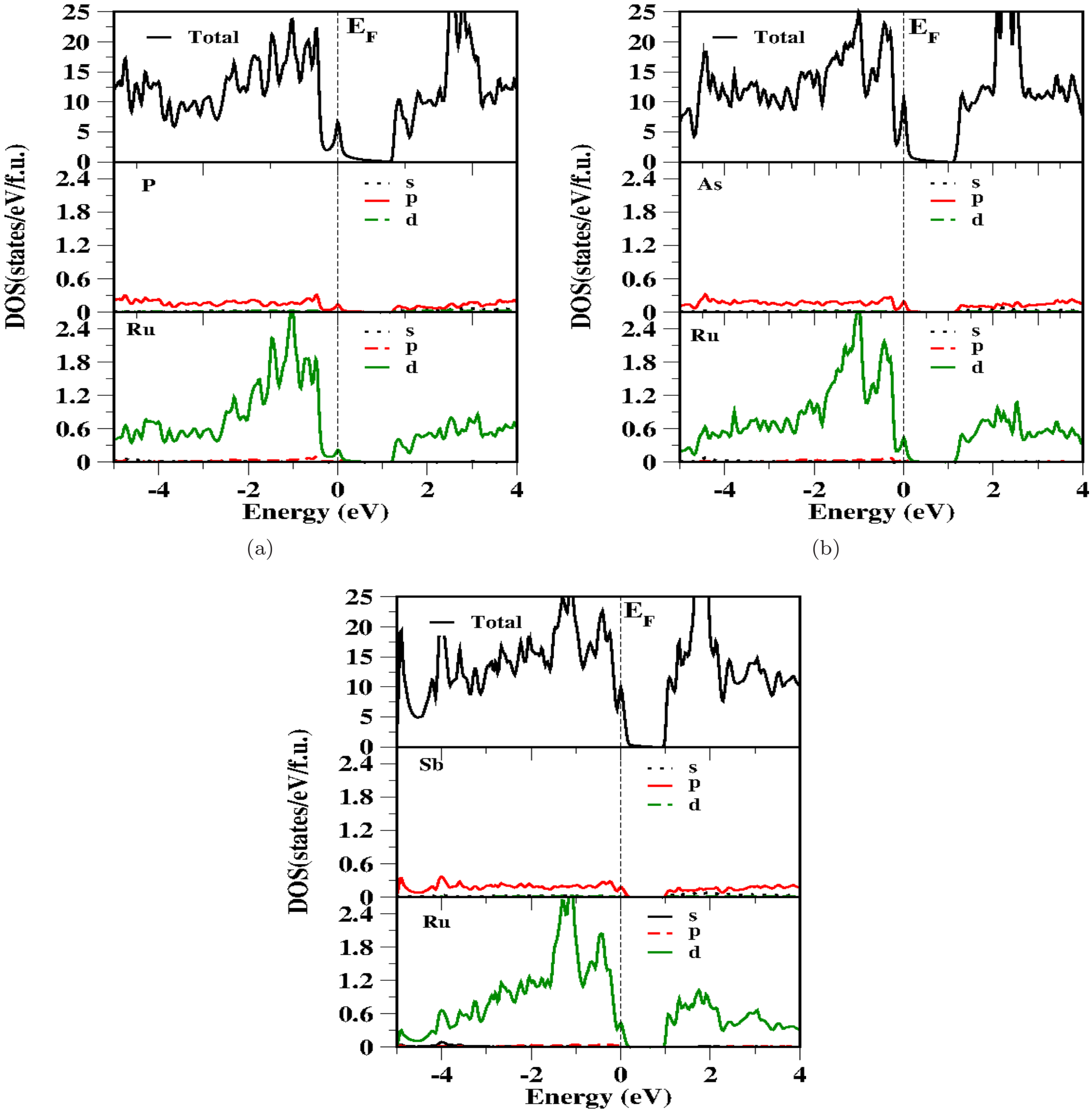

(a)

(b)

(c)

Figure 7.5: Density of states for (a) $LaRu_4P_{12}$, (b) $LaRu_4As_{12}$ and (c) $LaRu_4Sb_{12}$ at $V/V_0 = 1.0$. The orbital contribution from different atoms are represented by various colors and symbols.

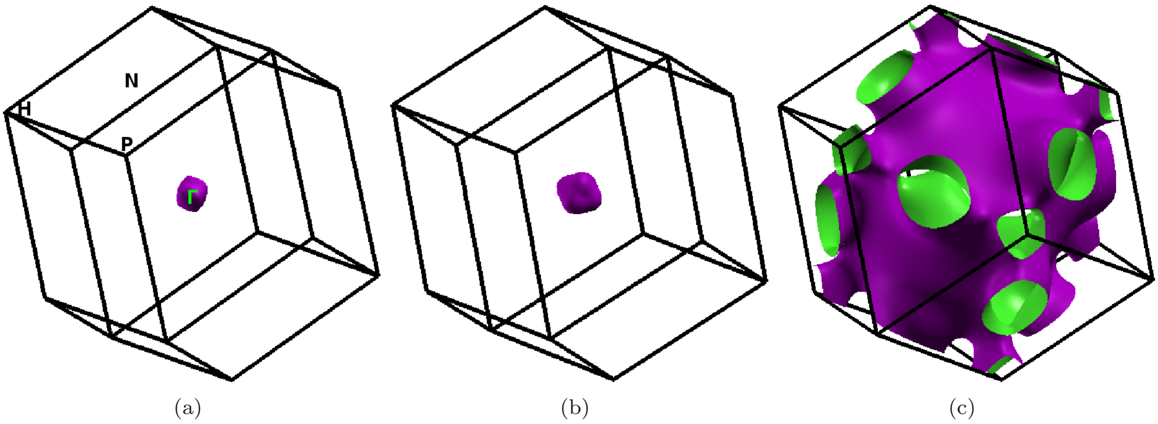

(a) (b) (c)

Figure 7.6: Fermi surface of $LaRu_4P_{12}$ at V/V_0= 1.0. (a, b) are the hole surfaces centered at Γ, arising from the doubly degenerate band (blue and green color) as shown in Fig. 7.1, (c) is the complicated surface arising from the black color band as shown in Fig, 7.1.

P point in the FS. Again the presence of the nearly flat band along *PN* direction in the case of $LaRu_4P_{12}$ support the observed nesting feature in P containing compounds. One more interesting feature in the complicated FS of these investigated compounds is the open orbit (especially at *P* and *N* points) FS in the case of $LaRu_4P_{12}$, which is completely different from the other compounds, where we find the FS sheet to be connected around *P* and *N* point just below the surface of the Brillouin zone, resulting in multiple opening in the sheet and is evident from the Fig. 7.6 (c) and Fig. 7.7 (b, d).

7.3.3 Effect under compression

Under compression, we observe an opposite movement of the non-degenerate and doubly degenerate bands irrespective of their position at the Γ point and the band structure under compression at V/V_0 = 0.8 is shown in Fig. 7.8. The non-degenerate band (mainly derived from the Ru 'd_{z^2}' orbital) shifts down and the degenerate bands (mainly derived from the X 'p_z' orbital) shift up under compression. In other words, we can say that the non-degenerate band gets populated and the doubly degenerated bands get depopulated under compression, resulting in the electron concentration of the Ru 'd_{z^2}' orbital to increase and the same electron concentration in the X 'p_z' orbital decreases. Due to this, in $LaRu_4P_{12}$ the size of the two hole pockets increase under compression but the topology remain the same as evident from the band structure plots in Fig. 7.8 (a) and in other two compounds the hole pockets get reduced in size and finally at V/V_0=0.80 the hole pocket vanishes only in the case of $LaRu_4Sb_{12}$. In the case of $LaRu_4As_{12}$, under compression we observe two extra hole pockets at Γ point (Fig. 7.9 (a, b)) due to the upward movement of the doubly degenerate bands, but not in the

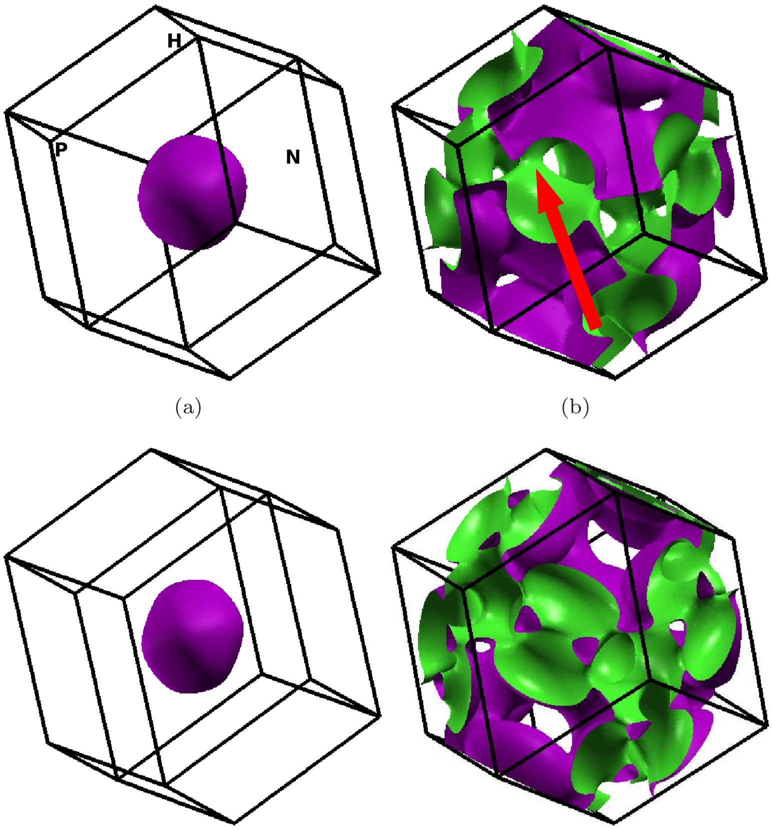

(a) (b)

(c) (d)

Figure 7.7: Fermi surface of (a, b) for $LaRu_4As_{12}$ and (c, d) for $LaRu_4Sb_{12}$ at $V/V_0 = 1.0$. (a, c) are the hole surface centered at Γ, arising from doubly degenerate band (blue and green color) as shown in Fig. 7.1, (b, d) are the complicated surface arising from the black color band as shown in Fig, 7.1.

case of $LaRu_4Sb_{12}$ due to the positioning of the band more deeper in energy and is well evident from the Fig. 7.1 (e) and 7.8 (c). The main interesting feature in $LaRu_4As_{12}$ is the FS topology change under compression in the complicated surface, where we find the interconnected sheets to separate and the FS contains multiple sheets centered at H point in the Brillouin zone and is well evident from arrow mark in the FS figure in Fig. 7.7 (b) and 7.9 (d). So the appearance of new pocket may apparently project $LaRu_4As_{12}$ to behave like a multiband superconductor under compression. But the topology of the complex surface of $LaRu_4P_{12}$ remains unchanged under compression.

Apart from this we find the $N(E_F)$ due to the black color band to decrease for all the investigated compounds under compression, but the rate of decrease is less in P and Sb containing compounds in comparison to the As containing compound and the values are 3.74, 4.7 and 5.4 states/eV/f.u. for P, As, Sb containing compounds, respectively. This observed drastic decrease in $N(E_F)$ in the case of $LaRu_4As_{12}$ may cause reduction in T_c under compression and the superconducting transition

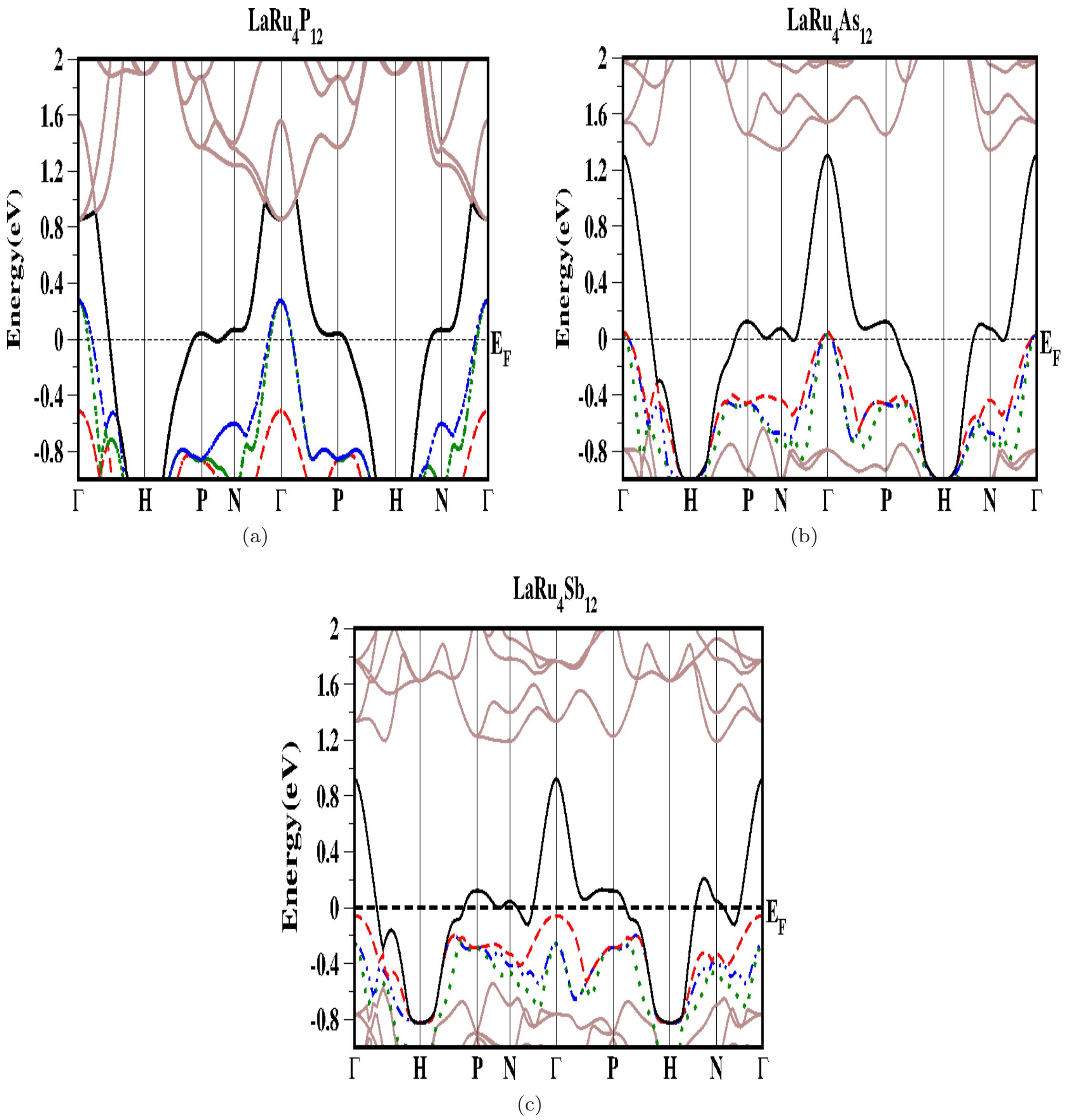

(a) (b)

(c)

Figure 7.8: Band structure of $LaRu_4X_{12}$ with X = P, As, Sb at V/V_0= 0.8. Color code used for the plots is similar at ambient and compressed volume to identify the changes in band structure easily under compression.

temperature might be in the same range as of the P and Sb containing compounds. This observed change in the case of As containing compound among these investigated compounds may be due to the observed FS topology change in the complicated sheet, which is mainly derived from the black color band.

In addition, we have calculated the dHvA frequency for all the compounds at ambient as well as under compression and the character of the dHvA orbits are tabulated in Table-7.2-7.5. In all, our study revealed a number of frequency branches for the complicated Fermi surface of the compounds studied and some of the branches are also having multiple copies of orbits at ambient pressure as well as under compression. The dHvA frequency is found to be higher in $LaRu_4As_{12}$ than $LaRu_4Sb_{12}$ for the first band, which is derived from the Ru d_z^2 orbital in both the compounds. More interestingly we observe the number of dHvA frequency branches to be reduced in the As and Sb containing compounds under compression, where we have also found the Fermi surface topology to change. But the number of frequency branches are found to be same for $LaRu_4P_{12}$ under compression and we also have not found any Fermi surface topology change till higher compression and is clearly evident from our calculated values as reported in Table-7.2. In the case of $LaRu_4As_{12}$ we have nine different branches at ambient pressure with different frequency and the values are reported in Table-7.3. At compression around $V/V_0 = 0.8$ we have seen all the orbits to disappear for this compound except two orbits positioned at (0.5 0.5 0.5) and (0.51 0.48 0.46) which are having frequency 7.03 and 7.19 kT respectively at ambient. Similarly in the case of $LaRu_4Sb_{12}$ (Table-7.4 and 7.5) we have seen few branches to disappear and a few new branches to appear under compression at $V/V_0= 0.8$. We find the branches with frequencies 0.496, 0.596, 1.12, 1.2, 1.397, 1.399, 5.357, 5.4 and 5.69 kT at ambient pressure to disappear under compression and simultaneously the branches with frequencies 0.0138, 1.40, 3.84 and 5.24 kT are found to appear at $V/V_0 = 0.8$ and well support the FS topology change. Overall the number of frequency branches is found to be decreased under compression in the case of As and Sb containing compounds.

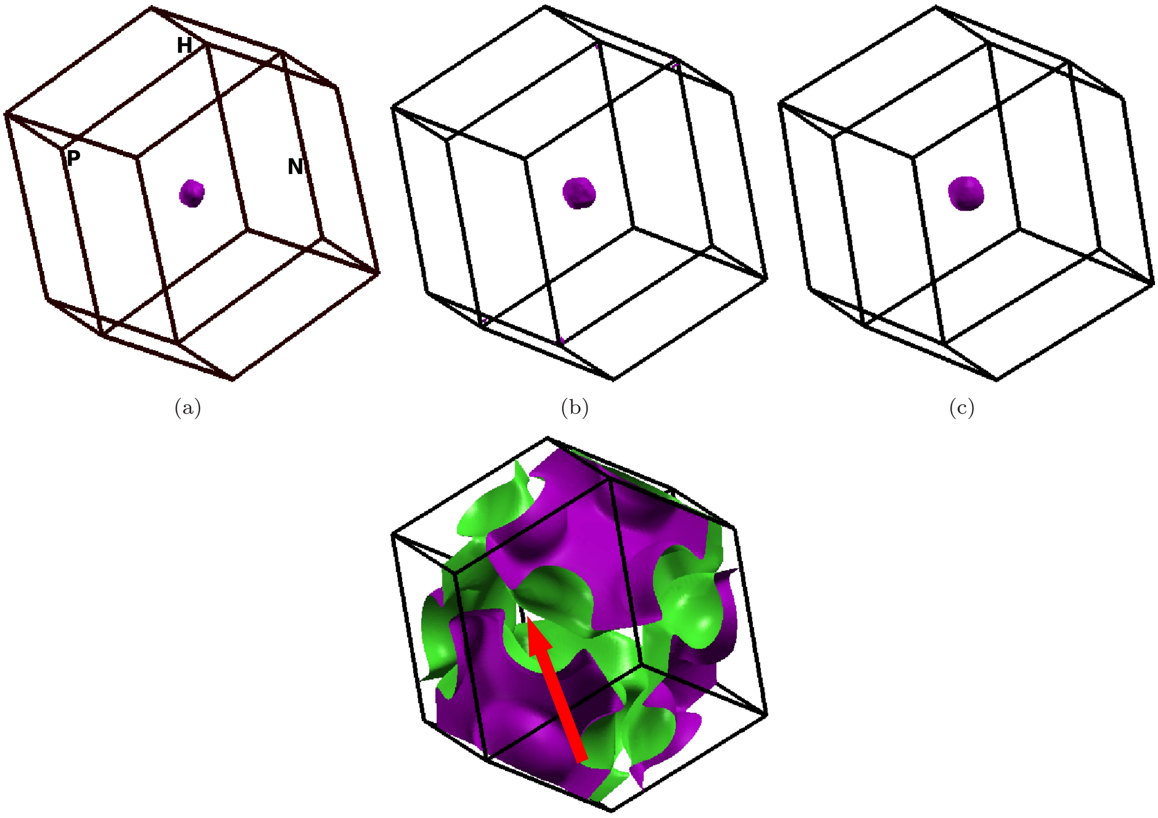

(a) (b) (c)

(d)

Figure 7.9: Fermi surface of $LaRu_4As_{12}$ at $V/V_0 = 0.8$. (a, b) are the two new hole pockets which appear at Γ under compression due to the upward movement of the doubly degenerate band (green and blue color) as shown in Fig. 7.8. The arrow mark indicates the observed change at $V/V_0 = 0.8$ with respect to $V/V_0 = 1.0$ (Fig. 7.7b).

Table 7.2: dHvA orbits for $LaRu_4P_{12}$ at $V/V_0 = 1.0$ and 0.8. The ‘e’ and ‘h’ represents the electron and hole character of the orbit. Frequency in kilo tesla (kT)

Band number	V/V_0	F(kT)	m^*(m)	Number of orbits	Type
1	1.0	0.119	0.229	1	h
	0.8	0.61	0.27	1	h
2	1.0	0.2	0.401	1	h
	0.8	0.86	0.395	1	h
3	1.0	0.163	1.668	2	e
		0.59	1.42	1	h
		1.29	5.15	2	h
		6.5	4.95	2	h
	0.8	0.134	1.288	2	e
		0.64	1.12	1	h
		0.135	1.29	2	e
		1.55	3.67	2	h

Table 7.3: dHvA orbits for $LaRu_4As_{12}$ at $V/V_0 = 1.0$ and 0.8. The 'e' and 'h' represents the electron and hole character of the orbit. Frequency in kilo tesla (kT)

Band number	V/V_0	F(kT)	m^*(m)	Number of orbits	Type
1	1.0	1.15	0.756	1	h
	0.8	0.145	0.478	1	h
2	1.0	0.0387	1.2	2	e
		0.0394	1.18	2	e
		0.043	1.31	2	e
		0.044	1.27	2	e
		0.692	1.41	1	h
		0.693	1.43	1	h
		6.84	5.06	2	e
		7.03	4.32	1	e
		7.19	5.26	2	e
	0.8	8.16	3.59	1	e
		8.17	3.76	1	e
3	0.8	0.078	0.206	1	h
4	0.8	0.117	0.454	1	h

Table 7.4: dHvA orbits for $LaRu_4Sb_{12}$ at $V/V_0 = 1.0$. The 'e' and 'h' represents the electron and hole character of the orbit. Frequency in kilo tesla (kT)

Band number	V/V_0	F(kT)	m^*(m)	Number of orbits	Type
1	1.0	0.952	0.993	1	h
2	1.0	0.057	0.55	2	e
		0.0825	0.738	1	h
		0.0842	0.742	1	h
		0.273	0.796	2	e
		0.496	0.54	4	h
		0.596	1.1	2	e
		1.013	1.13	2	h
		1.12	2.15	4	h
		1.2	1.3	1	e
		1.2	1.2	1	e
		1.397	2.93	2	h
		1.39	2.94	2	h
		5.24	4.01	1	h
		5.35	4.98	1	e
		5.356	5.33	1	e
		5.357	4.78	1	e
		5.4	5.04	2	e
		5.69	3.85	2	e

Table 7.5: dHvA orbits for $LaRu_4Sb_{12}$ at $V/V_0 = 0.8$. The 'e' and 'h' represents the electron and hole character of the orbit. Frequency in kilo tesla (kT)

Band number	V/V_0	$F(kT)$	m^*(m)	Number of orbits	Type
1	0.8	-	-	-	-
	0.8	0.0136	0.367	2	e
		0.0138	0.368	2	e
		0.233	0.696	2	e
		0.268	1.02	1	h
		0.272	1.03	1	h
		0.627	1.44	2	e
		1.40	1.51	1	e
		1.43	9.16	2	h
		3.84	4.85	2	h
		5.24	5.6	2	h
		6.19	3.69	1	e
		6.20	3.62	1	e
		6.21	3.88	1	e
		6.34	3.79	1	e

7.4 Conclusion

The band structure, density of states and Fermi surface have been investigated for the filled skutterudites compounds $\mathrm{LaRu_4X_{12}}$ with X = P, As, Sb. The states at the Fermi level are found to be dominated by the Ru '*d*' with the admixture of X '*p*' orbitals. We find three FS for the P containing compounds and two FS for the As and Sb containing compounds. Among these surfaces the hole pocket centered at Γ is mainly derived from the P 'p_z' orbital in the case of $\mathrm{LaRu_4P_{12}}$, and the same hole surface for $\mathrm{LaRu_4As_{12}}$ and $\mathrm{LaRu_4Sb_{12}}$ is found to be mainly from the Ru 'd_{z^2}'. Among all these three compounds the nesting feature is expected only in $\mathrm{LaRu_4P_{12}}$ and a drastic Fermi surface topology change is observed in the complicated sheet under compression in $\mathrm{LaRu_4As_{12}}$. From the FS change we predict $\mathrm{LaRu_4As_{12}}$ to be a multi band superconductor. In addition, from the dHvA calculation we find the number of extremal orbits to vary for the complicated FS sheet band in the case of As and Sb containing compounds under compression, where we have also seen the FS topology to change, whereas no such change is observed for P containing compound at ambient pressure as well as under compression.

Chapter 8

Conclusions

Studying electronic properties of the material in microscopic scale is paid more attention in condensed matter physics. Density Functional Theory (DFT) is used to solve quantum many body problem and is extensively used for calculating different material properties. In this present work we have used DFT to calculate Fermi surface (FS) properties of Cu_3Au-type and some La based skutterudite compounds and try to relate the FS topology change with other properties such as elastic constants, density of states at the Fermi level and superconducting transition temperature under pressure.

The introduction chapter explains the importance of the FS topology in different metallic systems, present a short introduction to superconductors and gives a brief idea about the materials which we have chosen in our present work. In the second chapter we have given an over view of the DFT along with a short introduction to the linearized augmented plane wave method, pseudopotential method which are two different electronic structure calculation method as implemented in the WIEN2*k* and Quantum Espresso codes, respectively. In our present thesis we have used WIEN2*k* code to calculate the electronic properties, FS topology, mechanical properties and to analyze the superconducting properties of all the chosen compounds, we have used Quantum Espresso package.

In chapter 3-7, the results and discussions are elaborated for the chosen series of compounds AX_3 (A = La, Y; X = In, Tl, Sn, Pb), La_3X (X = In, Tl, Sn), La_3InZ (Z = N, O) and $LaRu_4X_{12}$ (X = P, As, Sb). In chapter-3, we have presented a complete study on the electronic structure, Fermi surface topology, elastic constants of LaX_3 and YX_3 at ambient as well as under compression. We have shown the importance of spin-orbit coupling (SOC) in the electronic structure of the isoelectronic and isostructural $LaSn_3$ and YSn_3 compounds, where we find the electronic structure to change at the vicinity of the Fermi level in these two compounds leading to the FS topology change, whereas the same is not seen if SOC is not included. At the same time we have not found any change among LaX_3 and YX_3 with the inclusion of SOC for X = In, Tl, Pb. Secondly we find La '4*f*' orbital hybridization to be more pronounced instead of La '*d*' orbital at the vicinity of the Fermi level in the case of $LaSn_3$ though no '*f*' electron is present in both La and Y, but the A '*d*' orbital is dominating in the other AX_3 compounds with A = La, Y and X = In, Tl Pb leading to the expectation that the other properties might be the same for these compounds. Surprisingly the pressure effect on FS topology show the topology to change under compression for all the compounds except for YSn_3 and YPb_3. The difference in behaviour between YSn_3 and $LaSn_3$ could be mainly due to the SOC and the dominating nature of La '4*f*' hybridization, whereas the different behaviour of $LaPb_3$ and YPb_3 was explained from the presence of C_{44} elastic softening under pressure only in the case of the $LaPb_3$, which might be leading to the FS topology change in $LaPb_3$.

In the chapter-4 we have presented a comparative study of LaX_3 and La_3X compounds with X = In, Tl, Sn, and have shown a strong interaction to exist in La_3X compounds in comparison with the LaX_3 compounds. The different bonding nature among these two series of compounds is attributed to the different La '*d*' orbital spliting due to the local tetragonal and octahedral site symmetry of La in La_3X and LaX_3, respectively. From the analysis of the density of states we find the density of the states to be higher in La_3X compounds than LaX_3 compounds, which ultimately gives the indication for the superconducting transition temperature, T_c to higher in the former compounds and it is verified in chapter-5. Apart from this FS topology change is observed in all the La_3X compounds under pressure and might be further reflected on the T_c variation. FS topology change is observed in all FS sheet for all compounds of La_3X (X = In, Tl, Sn) series, whereas FS topology change is observed only in complicated sheet in LaX_3 series, indicating the strong hybridizing effect between La '*d*' and X '*p*' orbital in the former series.

To correlate the FS topology change with the variation of T_c under pressure, in chapter-5 the superconductivity of all AX_3 (A = La, Y; X = In, Tl, Sn) and La_3X (X = In, Sn) compounds are calculated under pressure and T_c is found to vary non-monotonically under pressure for the compounds where we have observed FS topology change. In addition, we observe a increase of T_c under pressure for La_3X compounds due to the softening of lower frequency modes especially at R and M points and a decrease of T_c is observed for AX_3 compounds due to the continuous hardening of all the modes in all high symmetry directions. We observed the mechanical properties to be the same for both the series of compounds despite the electronic properties being different. A dynamical instability is found only in La_3In under pressure due to the continuous softening of the lower frequency branches in particular at M and R high symmetry points in the Brillouin zone.

Apart from this in chapter-6 we have calculated the FS topology of La_3InZ compounds and compared the same with La_3In. The addition of the Z atom in the body center of the La_3In form La_3InZ compounds retaining the crystal structure to be the same. We find the FS topology to change under compression only in the case of La_3InO but not in La_3InN and is also reflecting on the density of states at the Fermi level and T_c. We find a non-linear variation of the density of states ($N(E_F)$) under compression in La_3InO and the variation of $N(E_F)$ is linearly decreasing in the case of La_3InN. A sudden increase of $N(E_F)$ is attributed to the appearance of three new hole pockets at R and an additional electron sheet along M-Γ direction. In addition the superconductivity calculation show T_c to be more than 2 K for La_3InO and it was found to be less than 2 K for La_3InN and it is due to the hardening of the frequency modes corresponding to the Z atoms contribution and is confirmed from the phonon density of states. From the comparative study of La_3In and La_3InZ we found the strong interaction to exist among La and In in La_3In in comparison with La_3InZ, leading to a higher T_c in La_3In. More interestingly from the mechanical properties, it was found that La_3InO is ductile in nature whereas La_3InN is brittle and is further confirmed from the Cauchy's pressure and Pugh's ratio.

In chapter-7 we have calculated the FS topology of $LaRu_4X_{12}$ (X = P, As, Sb) at ambient as well as under compression and find the topology to change in the case of the $LaRu_4As_{12}$ and behave like multiband superconductor. A FS nesting feature is observed in $LaRu_4P_{12}$. In addition the variation of T_c with different X atom is analyzed from the band structure calculation and we show a more dispersive band to contribute maximum towards the T_c. From our calculated de Haas van Affect (dHvA) calculation we find the number of extremal orbits to change under compression for the compounds where we have observed the FS topology change.

Overall from the present work we predict that FS topology change may induce a non-monotonic variation of T_c under pressure. Apart from these Cu_3Au-type compounds, we have also analyzed the Fermi surface topology of the La based skutterudite $LaRu_4X_{12}$ (X = P, As, Sb) at ambient as well as under compression. As mentioned and discussed above, skutterudites are quite interesting and have promising application. Though it would be computationally quite expensive, it would be worthy to analyze the complete phonon dispersion of these compounds at ambient and under pressure, which might give us a complete insight about the electron-phonon coupling and the T_c of these compounds under pressure, which would be taken up as a future work.

References

[1] D. Shoenberg. Magnetic Oscillations. Cambridge Univ. Press, Cambridge, 1984.

[2] L. Onsager. Interpretation of the de Haas-van Alphen effect. *Phil. Mag.* 43, (1952) 1006-1008.

[3] D. J. Scalapino and E. Loh, Jr., J. E. Hirsch. Fermi-surface instabilities and superconducting d-wave pairing. *Phys. Rev. B* 35, (1987) 6694-6698.

[4] Swetarekha Ram, Mudavath Rahul Chauhan, Kunal Agarwal and V. Kanchana. Ab initio study of Heusler alloys Co_2XY (X = Cr, Mn, Fe; Y = Al, Ga) under high pressure. *Phil. Mag. Lett.* 91, (2011) 545-553 .

[5] Swetarekha Ram and V. Kanchana. Fermi surface studies of Co-based Heusler alloys: Ab-initio study. *AIP Conf. Proc.* 1512, (2013) 1102-1103.

[6] S. B. Dugdale, M. A. Alam, I. Wilkinson, R. J. Hughes, I. R. Fisher, P. C. Canfield, T. Jarlborg and G. Santi. Nesting properties and anisotropy of the Fermi surface of $LuNi_2B_2C$. *Phys. Rev. Lett.* 83, (1999) 4824-4827.

[7] J. Y. Rhee, X. Wang and B. N. Harmon. Generalized susceptibility and magnetic ordering in rare-earth nickel boride carbides. *Phys. Rev. B* 51, (1995) 15585-15587.

[8] H. Shishido, R. Settai, H. Harima and Y. Ōnuki. A drastic change of the Fermi surface at a critical pressure in $CeRhIn_5$: dHvA study under pressure. *J. Phys. Soc. Jpn.* 74, (2005) 1103-1106.

[9] Y. Haga, M. Nakashima, R. Settai, S. Ikeda, T. Okubo, S. Araki, T. C. Kobayashi, N. Tateiwa and Y. Ōnuki. A change of the Fermi surface across the metamagnetic transition under pressure in UGe_2. *J. Phys.: Condens. Matter* 14, (2002) L125-L135.

[10] R. Settai, M. Nakashima, S. Araki, Y. Haga, T. C. Kobayashi, N. Tateiwa, H. Yamagami and Y. Ōnuki. A change of the Fermi surface in UGe_2 across the critical pressure. *J. Phys.: Condens. Matter* 14, (2002) L29-L36.

[11] H. Rosner, D. Koudela, U. Schwarz, A. Handstein, M. Hanfland, I. Opahle, K. Koepernik, M. D. Kuzmin, K.-H. Müller, J. A. Mydosh and M. Richter. Magneto-elastic lattice collapse in YCo_5 *Nature Phys.* 2, (2006) 469-472.

[12] F. Chen, Z. J. Huang, R. L. Meng, Y. Y. Sun, and C. W. Chu. Possible existence of a Van Hove singularity near the Fermi surface of $HgBa_2CaCu_2O_{6+\delta}$. *Phys. Rev. B* 48, (1993) 16047-16050.

[13] A. I. Coldea, C. M. J. Andrew, J. G. Analytis, R. D. McDonald, A. F. Bangura, J. -H. Chu, I. R. Fisher, and A. Carrington. Topological change of the Fermi surface in ternary iron pnictides with reduced c/a ratio: A de Haas van Alphen study of $CaFe_2P_2$. *Phys. Rev. Lett.* 103, (2009) 026404-026407.

[14] Y. -Z Zhang, H. C. Kandpal, I. Opahle, H. O. Jeschke, and R. Valenti. Microscopic origin of pressure-induced phase transitions in the iron pnictide superconductors AFe_2As_2: An ab initio molecular dynamics study *Phys. Rev. B* 80, (2009) 094530-1-094530-6.

[15] E. Hassinger, G. Gredat, F. Valade, S. Renéde Cotret, A. Juneau-Fecteau, J. -Ph. Reid, H. Kim, M. A. Tanatar, R. Prozorov, B. Shen, H. -H. Wen, N. Doiron-Leyraud, and Louis Taillefer. Pressure-induced Fermi surface reconstruction in the iron-arsenide superconductor $Ba_{1x}K_xFe_2As_2$: Evidence of a phase transition inside the antiferromagnetic phase. *Phys. Rev. B* 86, (2012) 140502-1-140506-5(R).

[16] L. D. Jennings and C. A. Swenson. Effects of pressure on the superconducting transition temperatures of Sn, In, Ta, Tl, and Hg. *Phys. Rev.* 112, (1958) 31-43.

[17] J. Hatton. Effect of pressure on superconducting transitions and on electrical resistance at low temperatures. *Phys. Rev.* 103, (1956) 1167-1172.

[18] C. W. Chu, T. F. Smith and W. E. Gardner. Superconductivity of rhenium and some rhenium-osmium alloys at high pressure *Phys. Rev. Lett.* 20, (1968) 198-201.

[19] V. I. Makarov and V. G. Bar'yakhtar. Anomalies in the superconducting transition temperature under pressure. Zh. Eksperim. i Teor. Fiz. 48, (1965) 1717-1722; [English transl.: Sov. Phys. JETP **21**, 1151-1154 (1965)].

[20] I. M. Lifshitz. Anomalies of electron characteristics of a metal in the high pressure region, *Sov. Phys. JETP* 11, (1960) 1130-1135.

[21] C. W. Chu, T. F. Smith and W. E. Gardner. Study of Fermi surface topology changes in rhenium and dilute Re solid solutions from T$_c$ measurements at high pressure. *Phys. Rev. B* 1, (1970) 214-221.

[22] V. V. Struzhkin, Y. A. Timofeev, R. J. Hemley and H. K. Mao. Superconducting T_c and electron-phonon coupling in Nb to 132 GPa: magnetic susceptibility at megabar pressures *Phys. Rev. Lett.* 79, (1997) 4262-4265.

[23] G. Vaitheeswaran, I. B. Shameen Banu, M. Rajagopalan. Theoretical calculation of superconducting transition temperature in vanadium under pressure *Solid State Commun.* 116, (2000) 401-404.

[24] A. Landa, J. Klepeis, P. Söderlind, I. Naumov, O. Velikokhatnyi, L. Vitos, A. Ruban. Fermi surface nesting and pre-martensitic softening in V and Nb at high pressures. *J. Phys.: Condens. Matter* 18, (2006) 5079-5085.

[25] A. Ciechan, M. J. Winiarski, M. Samsel-Czekaa. The pressure effects on electronic structure of iron chalcogenide superconductors FeSe$_{1-x}$Te$_x$, arXiv: 1111.3523.

[26] R. Z. Bachrach. Synchrotron radiation research, advances in surface and interface science. Vol. 1, (Plenum Press, New York, 1992).

[27] J. Braun. The theory of angle-resolved ultraviolet photoemission and its applications to ordered materials *Rep. Prog. Phys.* 59, (1996) 1267-1338.

[28] C. R. Brundle, and A. D. Baker. Electron Spectroscopy: Theory, Techniques, and Applications. Vol. 1, (Academic Press, New York, 1977).

[29] C. Kittel. Introduction to Solid State Physics, Sixth edition, (John Wiley and SonsInc., New York, 1986).

[30] L. W. Schubnikov, W. J. de Haas. Proceedings of the Royal Netherlands Academy of Arts and Science 33, (1930) 130.

[31] L. W. Schubnikov, W. J. de Haas. Proceedings of the Royal Netherlands Academy of Arts and Science 33, (1930) 163.

[32] H. K. Onnes. Further experiments with liquid helium. G. On the electrical resistance of pure metals, etc. VI. On the sudden change in the rate at which the resistance of mercury disappears. Comm. Phys. Lab. Univ. Leiden, No. 124c, (1911).

[33] G. J. Sizoo and H. K. Onnes. Further experiments with liquid helium. commun. Phys. Lab. Univ. Leiden, No. 180b (1925).

[34] J. Bardeen, L. N. Cooper and J. R. Schrieffer. Theory of superconductivity. *Phys. Rev.* 108, (1957) 1175-1204.

[35] B. T. Matthias, T. H. Geballe, S. Geller, E. Corenzwit. Superconductivity of Nb_3Sn *Phys. Rev.* 95, (1954) 1435-1435.

[36] B. T. Matthias, T. H. Geballe, R. H. Willens, E. Corenzwit, G. W. Hull. Superconductivity of Nb_3Ge *Phys. Rev.* 139, (1965) A1501-A1503.

[37] J. Nagamatsu, N. Nakagawa, T. Muranaka, Y. Zenaitani and J. Akimitsu. Superconductivity at 39 K in magnesium diboride *Nature* 410, (2001) 63-64.

[38] Hume-Rothery, W.: J. Inst. Metals 35 (1925) 209-212.

[39] E. Zintl. Intermetallische Verbindungen, *Angewandte Chemie* 52.1 (1939) 1-6.

[40] Laves, F.: Kristallographie der Legierungen. Naturwissenschaf-ten 27 (1939) 6573.

[41] S. Sankaralingam, S. Mathi Jaya, R. Asokamani. Studies on the electronic structure and superconducting behavior of the intermetallic compounds ABi_2 (A = K, Rb, Cs). *J. of Low Temp. Phys.* 88, (1992) 1-14.

[42] N. W. Ashcroft. Superconductivity: Putting the squeeze on lithium. Nature 419, (2002) 569-572.

[43] P. B. Allen and M. L. Cohen. Pseudopotential calculation of the mass enhancement and superconducting transition temperature of simple metals *Phys. Rev.* 187, (1969) 525-538.

[44] K. M. Lang, A. Mizel, J. Mortara, E. Hudson, J. Hone, M. L. Cohen, A. Zettl and J. C. Davis. Search for superconductivity in lithium. *J. Low. Temp. Phys.* 114, (1999) 445-454.

[45] N. E. Christensen and D. L. Novikov. Predicted superconductive properties of lithium under pressure *Phys. Rev. Lett.* 86, (2001) 1861-1864.

[46] G. M. Eliashberg, Soviet Phys.-JEPT 11, 696 (1960); 12, 1000 (1961). ——G. M. Eliashberg. Temperature Greens function for electrons in a superconductor. *Sov. Phy. JETP* 12, (1960) 1000-1002.

[47] W. L. McMillan. Transition temperature of strong-coupled superconductors. *Phys. Rev.* 167, (1968) 331-344.

[48] P. B. Allen and R. C. Dynes. Superconductivity at very strong coupling *J. Phys. C: Solid State Phys.* 8, (1975) L158-L163.

[49] A. M. Toxen, R. J. Gambino and L. B. Welsh. Microscopic and Macroscopic Electronic Properties of the $AuCu_3$-Type Alloys: The $LaSn_3$-$LaIn_3$ Pseudobinary Alloy System *Phys. Rev. B* 8 (1973) 90-97.

[50] A. J. Arko and D. D. Koelling. de Haas-van Alphen effect and the band structure of UGe_3. *Phys. Rev. B* 17, (1978) 3104-3114.

[51] D. Dr̈kop, E. Braun. B. Politt, H. Schmidt, B. Roden and D. Wohlleben. Antiferromagnetic order and $4f$-instability of $CePb_3$. *Z. Phys. B- condens. Matt.* 63, (1986) 55-61.

[52] A. L. Cornelius, A. J. Arko, J. L. Sarrao, J. D. Thompson, M. F. Hundley, C. H. Booth, N. Harrison and P. M. Oppeneer. Electronic properties of UX_3(X=Ga, Al, and Sn) compounds in high magnetic fields: Transport, specific heat, magnetization, and quantum oscillations. *Phys. Rev. B* 59, (1999) 14473-14483.

[53] Z. Kletowski. High-field de Haasvan Alphen effect in $GdIn_3$. Phys. stat. sol. (a) 196 (2003) 356-358.

[54] H. Kitazawa, Q. Z. Gao, H. Shida, T. suzuki, A. Hasegawa and T. Kasuya. de Haas-van Alphen effects of $PrIn_3$ and $LaIn_3$ *J. Magn. Magn. Mat.* 52, (1985) 286-288.

[55] K. Betsuyaku, H. Harima. Electronic structure and electric field gradient of RIn_3 and $RTIn_5$ (R=La and Ce, T= Co, Rh and Ir). *J. Magn. Magn. mat.* 272-276, (2004) 187-188.

[56] T. Kawae, M. Shimogai, M. Mito, K. Takeda, H. Ishii and T. Kitai. La impurity effects on quadrupolar ordering in $PrPb_3$. *Phys. Rev. B* 65, (2001) 012409-1-012409-4.

[57] T. Kawae, T. Yamamoto, K. Yurue, M. Mito, K. Takeda and T. Kitai. Specific heat and electrical resistivity measurements in $Pr_{0.03}La_{0.97}Pb_3$. *Physica B* 329-333, (2003) 493-494.

[58] L. B. Welsh, A. M. Toxen and R. J. Gambino. Magnetic Properties of $LaSn_3$. *Phys. Rev. B* 4, (1971) 2921-2931.

[59] F. Borsa, R. G. Barnes and R. A. Reese. Nuclear magnetic resonance and M$\acute{'}$ossbauer effect study of Sn^{119} in rare earth-tin intermetallic compounds *Phys. Status Solidi (b)* 19, (1967) 359-371.

[60] L. B. Welsh, A. M. Toxen and R. J. Gambino. Nuclear magnetic resonance in the LaX_3 intermetallic compounds *Phys. Rev. B* 6, (1972) 1677-1685.

[61] E. E. Havinga, H. Damsma and M. H. Van Maaren. Oscillatory dependence of superconductive critical temperature on number of valency electrons in Cu_3Au-type alloys. *J. Phys. Chem. Solids* 31, (1970) 2653-2662.

[62] L. B. Welsh and J. B. Darby. NMR in $CeSn_xIn_{3-x}$ Alloys *AIP conf. Proc.* 10 (1973) 1325-1326.

[63] F. Heiniger, E. Bucher, J. P. Maita and P. Descouts. Superconducting and other electronic properties of La_3In, La_3Tl, and some related phases *Phys. Rev. B* 8, (1973) 3194-3205.

[64] Handbook of superconductivity edited by Charles P. Poole. Jr., (2000) (Academic press, London, UK)

[65] C. S. Garde, J. Ray and G. Chandra. Resistivity and thermopower studies on La_3X (X= Al, Sn, In, Ru, Ir, Co, Ni, Ge, Ga) systems. *J. Alloys and Comp.* 198, (1993) 165-172.

[66] P. Descouts, B. Perrin, A. Dupanloup and A. Treyvaud. Nuclear magnetic resonance study of La_3X compounds and related phases. *J. Phys. Chem. Solids* 39, (1978) 161-166.

[67] T. F. Smith and H. L. Luo. Superconductivity of lanthanum and lanthanum compounds at zero and high pressure. *J. Phys. Chem. Solids* 28, (1967) 569-576.

[68] J.-T. Zhao, Zhen-Chao Dong, J. T. Vaughey, J. E. Ostenson, D. J. Corbett. Synthesis, structures and properties of cubic R_3In and R_3InZ phases (R = Y, La; Z = B, C, N, O): The effect of interstitial Z on the superconductivity of La_3In. *J. of Alloys and Comp.* 230, (1995) 1-12.

[69] P. Ravindran and R. Asokamani. Suppression of superconductivity by carbon addition to La_3X (X identical to Al, Ga, In or Tl). *J. Phys.: Condens. Matter* 7, (1995) 5567-5577.

[70] M. Kirchner, W. Schnelle, F. R. Wagner and R. Niewa. Preparation, crystal structure and physical properties of ternary compounds (R_3N)In, R=rare-earth metal. *Solid State Science* 5, (2003) 1247-1257.

[71] I. Shirotani, T. Uchiumi, K. Ohno, and C. Sekine, Y. Nakazawa and K. Kanoda, S. Todo and T. Yagi. Superconductivity of filled skutterudites $LaRu_4As_{12}$ and $PrRu_4As_{12}$. *Phys. Rev. B* 56, (1997) 7866-7869.

[72] S. R. Saha, H. Sugawara, Y. Aoki, H. Sato, Y. Inada, H. Shishido, R. Settai, Y. Ōnuki, and H. Harima. Fermi surface of $LaRu_4P_{12}$: A clue to the origin of the metal-insulator transition in $PrRu_4P_{12}$. *Phys. Rev. B* 71, (2005) 132502-1-132502-4.

[73] L. Bochenek, R. Wawryk, Z. Henkie, and T. Cichorek. Evidence for multiple superconducting gaps in the filled skutterudite compound $LaRu_4As_{12}$. *Phys. Rev. B* 86, (2012) 060511-060515(R).

[74] H. Sugawara, Y. Abe, Y. Aoki, H. Sato, M. Hedo, R. Settai, Y. Ōnuki and H. Harima. The Fermi surface in filled skutterudite RFe_4P_{12} (R=La and Nd). *J. Phys. Soc. Jpn.* 69, (2000) 2938-2946.

[75] S. R Saha, H. Sugawara, R. Sakai, Y. Aoki, H. Sato, Y. Inada, H. Shishido, R. Settai, Y. Önuki, H. Harima. de Haasvan Alphen effect in $LaRu_4P_{12}$. *Physica B* 328, (2003) 6870.

[76] H. Sugawara, K. Abe, T. D. Matsuda, Y. Aoki, H. Sato, R. Settai, Y. Önuki. de Haas-van Alphen effect in the filled skutterudite $CeRu_4Sb_{12}$. *Physica B* 312-313, (2002) 264-266.

[77] T. Uchiumi, I. Shirotani, C. Sekine, S. Todo, T. Yagi, Y. Nakazawa, K. Kanoda. Superconductivity of $LaRu_4X_{12}$ (X=P, As and Sb) with skutterudite structure. *J. of Phys. and Chem. of Solids* 60, (1999) 689-695.

[78] E. E. Havinga. W-like dependence of critical temperature on number of valence electrons in non-transition metal Cu_3Au-type alloys. *Phys. Lett.* 28A, (1968) 350-351.

[79] B. T. Matthias. Empirical relation between superconductivity and the number of valence electrons per atom *Phys. Rev.* 97, (1955) 74-76.

[80] K. Kawashima, M. Maruyama, M. Fukuma, and J. Akimitsu. Superconducting state in YSn_3 with a $AuCu_3$-type structure. *Phys. Rev. B* 82, (2010) 094517-1094517-5.

[81] S. Huang, C. W. Chu, F. Y. Fradin and L. B. Welsh. Anomalous T_c-behavior of $LaSn_3$ under pressure. *Solid State Commun.* 16, (1975) 409-412.

[82] E. E. Havinga, H. Damsma and M. H. Van Maaren. Oscillatory dependence of superconductive critical temperature on number of valency electrons in Cu_3Au-type alloys. *J. Phys. Chem. Solids* 31, (1970) 2653-2662.

[83] L. B. welsh, C. L. Wiley, F. Y. Fradin. Gd and Ce impurities in the LaX_3 compounds (X= In, Sn, Pb): A nuclear-magnetic-resonance study. *Phys. Rev. B* 11, (1975) 4156-4167.

[84] T. F. Smith and H. L. Luo. Superconductivity of lanthanum and lanthanum compounds at zero and high pressure. *J. Phys. Chem. Solids* 28, (1967) 569-576.

[85] Y. Kawamura, T. Kawaai, J. Hayashi, C. Sekine, H. Gotou, J. Cheng, K. Matsubayashi, and Y. Uwatoko. Pressure effect on the structure and superconducting transition temperature of filled skutterudites LaT_4P_{12} (T=Fe, Ru). *J. Phys. Soc. Jpn.* 82, (2013) 114702-114705.

[86] P. Hohenberg and W. Kohn. In homogeneous electron gas. *Phys. Rev.*, 136, (1964) B864-B871.

[87] W. Kohn and L. Sham. Self-Consistent Equations Including Exchange and Correlation Effects. *Phys. Rev.* 140, (1965) A1133-A1138.

[88] R. G. Parr and W. Yang. *Density Functional Theory of Atoms and Molecules.* Oxford University, Oxford, 1989.

[89] W. Kohn. Nobel Lecture: Electronic structure of matterwave functions and density functionals. *Rev. Mod. Phys.* 71, (1998) 1253-1266.

[90] R. O. Jones and O. Gunnarsson. The density functional formalism, its applications and prospects. *Rev. Mod. Phys.* 61, (1989) 689-746.

[91] W. Koch and M. C. Holthausen, *A Chemists Guide to Density Functional Theory,* WILEY VCH (2001).

[92] M. R. Dreizler and E. K. U. Gross. *Density Functional Theory : An Approach to the Quantum Many-Body Problem* (Springer, Berlin, 1990).

[93] L. H. Thomas. The calculation of atomic fields. *Proc. Camb. Phil. Soc.* 23, (1927) 542-548.

[94] E. Fermi. A Statistical Method for the determination of some properties of the atom. *Rend. Accad. Naz. Linceiz* 6, (1927) 602-607.

[95] J. P. Perdew and A. Zunger. Self-interaction correction to density-functional approximations for many-electron systems. *Phys. Rev. B* 23, (1981) 5048-5079.

[96] J. P. Perdew and Y. Wang. Accurate and simple analytic representation of the electron-gas correlation energy. *Phys. Rev. B* 45, (1992) 13244-13249.

[97] J. P. Perdew and Y. Wang. Accurate and simple density functional for the electronic exchange energy: Generalized gradient approximation. *Phys. Rev. B* 33, (1986) 8800-8802.

[98] J. P. Perdew, K. Burke, M. Ernzerhof. Generalized Gradient Approximation Made Simple. *Phys. Rev. Lett.* 77, (1996) 3865-3868.

[99] A. D. Becke. Density-functional exchange-energy approximation with correct asymptotic behavior. *Phys. Rev. A* 38, (1988) 3098-3100.

[100] C. Lee, W. Yang, R. G. Parr. Development of the Colle-Salvetti correlation-energy formula into a functional of the electron density. *Phys. Rev. B* 37, (1988) 785-789.

[101] P. Blaha, K. Schwarz, G. K. H. Madsen, D. Kvasnicka and J. Luitz, WIEN2K, An augmented plane wave + local orbitals program for calculating crystal properties (Karlheinz Schwarz, Techn. Universität Wien, Austria), 2001.

[102] Hand book of Nano physics, Principles amd Methods, Edited by Klaus D. Sattler. CRC press, Taylor and Francis Group, 2011.

[103] P. Giannozzi, S. Baroni, N. Bonini, M. Calandra, R. Car, C. Cavazzoni, D. Ceresoli, G. L. Chiarotti, M. Cococcioni, I. Dabo, et al. QUANTUM ESPRESSO: a modular and open-source software project for quantum simulations of materials. *J. Phys.: Condens. Matter* 21, (2009) 395502-1-395502-19.

[104] S. Baroni, S. de Gironcoli, A. Dal Corso, and P. Giannozzi. Phonons and related crystal properties from density-functional perturbation theory. *Rev. Mod. Phys.* 73, (2001) 515-562.

[105] D. Vanderbilt. Soft self-consistent pseudopotentials in a generalized eigenvalue formalism. *Phys. Rev. B* 41, (1990) 7892-7895.

[106] P. M. C. Rourke and S. R. Julian. Numerical extraction of de Haas-van Alphen frequencies from calculated band energies. *Comput. Phys. Commun.* 183, (2012) 324-332.

[107] A. M. Toxen and R. J. Gambino. Evidence for a localized magnetic moment in lanthanum intermetallic compounds. *Phys. Lett. A* 28, (1968) 214-215.

[108] A. M. Toxen, R. J. Gambino and B. J. C. van der Hoever, Jr., in *Proccedings of the Twelfth International Low-temperature conference*, edited by E. Kauda (Academy of Japan, Kyoto, 1971), p. 351.

[109] W. D. Grobman. Transport properties and the electronic Structure of $\mathrm{LaSn}_{3-x}\mathrm{In}_x$. *Phys. Rev. B* 5, (1972) 2924-2931.

[110] G. K. Shenoy, B. D. Dunlap, G. M. Kalvius, A. M. Toxen and R. J. Gambino. Magnetic and Structural Properties of Some Rare-Earth-Sn_3 Compounds. *J. Appl. Phys.* 41, (1970) 1317-1318.

[111] A. P. Murani. Magnetic spectral response in the intermetallic compound CeSn_3. *Phys. Rev. B* 28, (1983) 2308-2311.

[112] E. M. Bittar, C. Adriano, C. Giles, C. Rettori, Z. Fisk and P. G. Pagliuso. Electron spin resonance study of the $\mathrm{LaIn}_{3x}\mathrm{Sn}_x$ superconducting system. *J. Phys.: Condens. Matter* 23, (2011) 455701-455705.

[113] F. Canepa, G. A. Costa and G. L. Olcese. Thermodynamics and magnetic properties of LaPb_3 and CePb_3. *Solid State Commun.* 45, (1983) 725-728

[114] S. D. Johnson, J. R. Young, R. J. Zieve and J. C. Cooley. Superconductivity in single-crystal YIn_3. *Solid State Commun.* 152, (2012) 513-515

[115] A. Hasegawa. Band Theory of the Intermetallic Compound LaSn_3. *J. Phys. Soc. Jpn.* 50, (1981) 3313-3320.

[116] R. M. Boulet, J. -P. Jan and H. L. Skriver. De Haas-van Alphen effect and LMTO band structure of LaSn_3. *J. Phys. F: Met. Phys.* 12, (1982) 293-301.

[117] A. Hasegawa and H. Yamagami. Effect of the Spin-Orbit Interaction on the Fermi Surface of LaSn_3. *J. Phys. Soc. Jpn.* 60, (1991) 1654-1665.

[118] S. B. Dugdale. First-principles study of electron-phonon superconductivity in YSn_3. *Phys. Rev. B* 83, (2011) 012502-1-012502-4.

[119] O. K. Andersen. Linear methods in band theory. *Phys. Rev. B* 12, (1975) 3060-3083.

[120] H. J. Monkhorst and J. D. Pack. Special points for Brillonin-zone integrations. *Phys. Rev. B* 13, (1976) 5188-5192.

[121] F. Birch. Finite elastic strain of cubic crystals. *Phys. Rev.* 71, (1947) 809-824.

[122] A. Kokalj. Computer graphics and graphical user interfaces as tools in simulations of matter at the atomic scale. *Comput. Mater. Sci.* 28, (2003) 155-168.

[123] J. F. Nye, Physical Properties of Crystals: Their Representation by Tensors and Matrices, (Oxford University Press, Oxford, 1985).

[124] M. Mattesini, R. Ahuja, and B. Johansson. Cubic Hf_3N_4 and Zr_3N_4: A class of hard materials. *Phys. Rev. B* 68, (2003) 184108-1-184108-5.

[125] M. Mattesini, J. M. Soler, and F. Ynduráin. Ab initio study of metal-organic framework-5 Zn4O(1,4-benzenedicarboxylate)3: An assessment of mechanical and spectroscopic properties. *Phys. Rev. B* 73, (2006) 094111-1-094111-8.

[126] R. Hill. The Elastic Behaviour of a Crystalline Aggregate. *Proc. Phys. Soc. London* 65, (1952) 349-354.

[127] A. Reuss. Calculation of the yield strength of mixed crystals due to plasticity and condition for single crystals. Z. Angew. Math. Phys. 9, (1929) 49-58.

[128] W. Voigt. About the relationship between the two Elastic constant isotropic body. Ann. Phys. (Leipzig) 38, (1889) 573-578.

[129] R. J. Gambino, N. R. Stemple and A. M. Toxen. Superconductivity of lanthanum intermetallic compounds with the Cu_3Au structure. *J. Phys. Chem. Solids* 29, (1968) 295-302.

[130] A. Landelli and A. Palenzona. Handbook on the Physics and Chemistry of Rare Earths. 2, (Amsterdam, North-Holland (1979)).

[131] C. Stassis, J. Zarestky, C -K. Loong, O. D. McMasters and R. M. Nicklow. Lattice dynamics of $LaSn_3$. Phys. Rev. B 23, (1981) 2227-2234.

[132] T. Shao-ping, Z. Kai-ming and X. Xi-de. The electronic structures of $LaSn_3$ and $LaIn_3$ *J. Phys.: Condens. Matter* 1, (1989) 2677-2682.

[133] D. Hackenbracht and J. Kübler. Cohesive and superconducting properties of La-In compounds from electronic-structure calculations. *Z. für Phys. B Cond. mat.* 35, (1979) 27-33.

[134] G. P. Schwartz and D. A. Shirley. Rare-earth valence-state studies of the series RIn_3 and RSn_3 derived from quadrupole coupling constants. *Hyperfine Interactions* 3, (1977) 67-76.

[135] W. B. Pearson. Hand Book of Lattice Spacings and Structures of Metals and Alloys. Vol. 2, (1967) (Pergamon Press, Oxford)

[136] V. B. Pluzhnikov, A. Czopnik and I. V. Svechkarev. de Haas-van Alphen effect in $ScGa_3$, $LuGa_3$ and YIn_3. *Physica B* 212, (1995) 375-378.

[137] E. E. Havinga. Oscillatory dependence of electronic properties of alloys with Cu_3Au-type structure; band structure calculations. *Solid State Commun.* 11, (1972) 1249-1252.

[138] S. F. Pugh. Relations between the elastic moduli and the plastic properties of polycrystalline pure metals. *Philos. Mag.* 45, (1954) 823-843.

[139] J. Haines, J. M. Leger and G. Bocquillon. Synthesis and design of superhard materials. *Ann. Rev. Mater. Res.* 31, (2001) 1-23.

[140] M. A. Dudek and N. Chawla. Nanoindentation of rare earthSn intermetallics in Pb-free solders. *Intermetallics* 18, (2010) 1016-1020.

[141] E. Bucher, K. Andres, J. P. Maita and G. W. Hull; Jr. Superconductors with Magnetic Impurities in a Singlet Ground State. Helv. Phys. Acta 41, (1968) 723-730.

[142] Z. Kletowski, R. Fabrowski, P. Slawiński and Z. Henkie. Resistance of some $REMe_3$ compounds, RE = La and Lu, Me = Sn, Pb, In, and Ga. *J. Mag. Mag. Materials* 166, (1997) 361-364

[143] S. Nasu, A. M. Van Diepen, H. H. Neumann and R. S. Craig. Specific heats of $LaIn_3$, $CeIn_3$ and $PrIn_3$ at temperatures between 15 and 42 K. *J. Phys. Chem. Solids* 32, (1971) 2773-2777.

[144] B. T. Matthias, V. B. Compton E. Corenzwit. Some new superconducting compounds. *J. Phys. Chem. Solids* 19, (1961) 130-133.

[145] E. Bucher, J. P. Maita, A. S. Cooper. Induced-Moment Systems: Paramagnetic Region of La_3Tl-Pr_3Tl. *Phys. Rev. B* 6, (1972) 2709-2716.

[146] A. Pasturel, C. Colinet, P. Hicter. Strong chemical interactions in disordered alloys. *Physica B+C* 132, (1985) 177-180.

[147] C. D. Gelatt, Jr., A. R. Williams, and V. L. Moruzzi. Theory of bonding of transition metals to nontransition metals. *Phys. Rev. B* 27, (1983) 2005-2013.

[148] W. Lin, A. J. Freeman. Cohesive properties and electronic structure of Heusler $L2_1$-phase compounds Ni_2XAl (X=Ti, V, Zr, Nb, Hf, and Ta). *Phys. Rev. B* 45, (1992) 61-68.

[149] D. H. Chung, W. R. Buessem. The Elastic Anisotropy of Crystals. *J. Appl. Phys.* 38, (1967) 2010-2012.

[150] K. A. Gschneidner Jr., O. D. Mcmasters and J. E. Ostenson. Influence of alloying on the superconducting transition temperature of La_3In. *J. Less-Comm. Metals* 62, (1978) 167-177 .

[151] D. Billington, T. M. Llewellyn-Jones, G. Maroso and S. B. Dugdale. Electronphonon superconductivity in YIn_3. *Supercond. Sci. Technol.* 26, (2013) 085007-085011.

[152] D. Vanderbilt. Soft self-consistent pseudopotentials in a generalized eigenvalue formalism. *Phys. Rev. B* 41, (1990) 7892-7895.

[153] S. Baroni, P. Giannozzi, and A. Testa. Greens-function approach to linear response in solids. *Phys. Rev. Lett.* 58, (1987) 1861-1864.

[154] G. M. Eliashberg. Interactions between electrons and lattice vibrations in a superconductor. *Sov. Phys. JETP* 11, (1960) 696-702.

[155] P. Morel and P. W. Anderson. Calculation of the superconducting state parameters with retarded electron-phonon interaction. *Phys. Rev.* 125, (1962) 1263-1271.

[156] Swetarekha Ram, V. Kanchana, A. Svane, S. B. Dugdale, and N. E. Christensen. Fermi surface properties of AB_3 (A = Y, La; B = Pb, In, Tl) intermetallic compounds under pressure. *J. Phys.: Condens. Matter* 25, (2013) 155501-155509.

[157] Swetarekha Ram, V. Kanchana, G. Vaitheeswaran, A. Svane, S. B. Dugdale, and N. E. Christensen. Electronic topological transition in $LaSn_3$ under pressure. *Phys. Rev. B* 85, (2012) 174531-1-174531-8.

[158] Swetarekha Ram, V. Kanchana, A. Svane, S. B. Dugdale, and N. E. Christensen. Calculated Electronic Structure and Fermi Surface Topology of La_3X (X = In, Tl, Sn): Effects of Compression (communicated).

[159] L. E. DeLong, M. B. Maple, and M. Tovar. Superconducting and normal state properties of dilute alloys of $LaSn_3$ containing Ce impurities. *Solid State Commun.* 26, (1978) 469-475.

[160] S. A. Ostanin, V. Yu. Trubitsin, S. Yu. Savrasov, M. Alouani, H. Dreysse. Calculated Nb superconducting transition temperature under hydrostatic pressure. *Comput. Mat. Sc.* 17, (2000) 202-205.

[161] Prabhakar P. Singh. From E_{2g} to Other Modes: Effects of pressure on electron-phonon interaction in MgB_2. *Phys. Rev. Lett.* 97, (2006) 247002-247005.

[162] R. Nagarajan, Chandan Mazumdar, Zakir Hossain, S. K. Dhar, K. V. Gopalakrishnan, L. C. Gupta, C. Godart, B. D. Padalia, and R. Vijayaraghavan. Bulk superconductivity at an elevated temperature (T_c=12 K) in a nickel containing alloy system Y-Ni-B-C. *Phys. Rev. Lett.* 72, (1994) 274-277.

[163] D. Jung. The role of oxygen for expressing superconductivity in La-Ca-Cu-O Compounds. *Bull. Korean Chem. Soc.* 20, (1999) 281-284.

[164] W. Mickelson, J. Cumings, W. Q. Han and A. Zettl. Effects of carbon doping on superconductivity in magnesium diboride. *Phys. Rev. B* 65, (2002) 052505-1-052505-3.

[165] Swetarekha Ram, V. Kanchana, A. Svane, S. B. Dugdale and N. E. Christensen. Superconducting properties of A_3X (A= La; X= In, Sn) and AX_3 (A= La, Y; X = In, Sn, Pb) under pressure: ab-initio study. (in preparation).

[166] R. A. Jishi and H. M. Alyahyaei. Electronic and lattice dynamical properties of the iron-based superconductors LiFeAs and NaFeAs. *Adv. in Condens. Matter Phys.* 2010, (2010) 804343-804348.

[167] C. H. Lin, T. Berlijn and W. Ku. Lifshitz transition and superconductivity enhancement in high pressure. $cI16$ Li. arXiv:1311.4005v1.

[168] M. Born, K. Huang. Dynamical theory of crystal lattices. Oxford University Press, 1954.

[169] Atsushi Miyake, Katsuya Shimizu, Chihiro Sekine, Kunihiro Kihou and Ichimin Shirotani. Electronic Structure, Electrical, Magnetic and Optical Properties-Pressure-Induced Superconductivity in Filled Skutterudite $PrRu_4P_{12}$ *J. Phys. Soc. Jpn.* 73 (2004) 2370-2372.

[170] K. Hachitani, H. Fukazawa and Y. Kohori. Evidence for magnetic ordering associated with metal-insulator transition in $SmRu_4P_{12}$ studied by muon spin relaxation. *Phys. Rev. B* 73, (2006) 052408-1-052408-4.

[171] H. Sato, H. Sugawara, D. Kikuchi, S. Sanada, K. Tanaka, H. Aoki, K. Kuwahara, Y. Aoki and M. Kohgi. Novelty and variety of the characteristics found in the filled skutterudites *Physica B* 378380 (2006) 4650.

[172] H. Sugawara, T. D. Matsuda, K. Abe, Y. Aoki, H. Sato, S. Nojiri, Y. Inada, R. Settai and Y. Onuki. Exotic heavy-fermion state in the filled skutterudite $PrFe_4P_{12}$ uncovered by the de Haas-van Alphen effect. *Phys. Rev. B* 66, (2002) 134411-1-134411-5.

[173] E. D. Bauer, N. A. Frederick, P.-C. Ho, V. S. Zapf, and M. B. Maple. Superconductivity and heavy fermion behavior in $PrOs_4Sb_{12}$ *Phys. Rev. B* 65 (2002) 100506-1-100506-4(R).

[174] Y. Aoki, A. Tsuchiya, T. Kanayama, S. R. Saha, H. Sugawara, H. Sato, W. Higemoto, A. Koda, K. Ohishi, K. Nishiyama, and R. Kadono. Time-Reversal Symmetry-Breaking Superconductivity in Heavy-Fermion $PrOs_4Sb_{12}$ Detected by Muon-Spin Relaxation *Phys. Rev. Lett.* 91 (2003) 067003.

[175] H. Harima, K. Takegahara. Conduction bands in the filled skutterudites. *J. Phys.: Condens. Matter* 15, (2003) S2081-S2086.

[176] B. C. Sales, D. Mandrus, and R. K. Williams. Filled Skutterudite Antimonides: A New Class of Thermoelectric Materials *Science* 272 (1996) 1325-1328.

[177] G. S. Nolas, D. T. Morelli and T. M. Tritt. SKUTTERUDITES: A Phonon-Glass-Electron Crystal Approach to Advanced Thermoelectric Energy Conversion Applications *Annu. Rev. Mater. Sci.* 29 (1999) 89-116.

[178] G. J. Snyder and E. S. Toberer. Complex thermoelectric materials *Nature Mater.* 7 (2008) 105-114.

[179] M. M. Koza, D. Adroja, N. Takeda, Z. Henkie and T. Cichorek. Vibrational dynamics of filled skutterudites LaT_4X_{12} (T = Fe, Ru, Os, X = As, Sb). *J. Phys. Soc. Jpn.* 82, (2013) 114607-114617.

[180] H. Harima, K. Takegahara. Fermi surface of the filled skutterudite $LaOs_4Sb_{12}$. *Physica C* 388-389, (2003) 555-556.

[181] H. Harima, K. Takegahara. Fermi surface of the filled skutterudite $LaOs_4P_{12}$. *Physica B* 403, (2008) 906-908.

[182] T. Namiki, Y. Aoki, H. Sato, C. Sekine, I. Shirotani, T. D. Matsuda, Y. Haga and T. Yagi. Superconducting Properties of Pr-Based Filled Skutterudite $PrRu_4As_{12}$. *J. Phys. Soc. Jpn.* 76, (2007) 093704-093707.

[183] R. W. Hill, Shiyan Li, M. B. Maple and L Taillefer. Multi-symmetry and multi-band superconductivity in filled-skutterudites $PrOs_4Sb_{12}$ and $PrRu_4Sb_{12}$. *arXiv:0709.4265* [cond-mat.supr-con](September 2007).

[184] K. Koga, K. Akai, K. Oshiro and M. Matsuura. Electronic structure and optical properties of binary skutterudite antimonides. *Phys. Rev. B* 71, (2005) 155119-1-155119-9.

[185] I. Shirotani, T. Uchiumi, K. Ohno, C. Sekine, Y. Nakazawa, K. Kanoda, S. Todo and T. Yagi. Superconductivity of filled skutterudites $LaRu_4As_{12}$ and $PrRu_4As_{12}$. *Phys. Rev. B* 56, (1997) 7866-7869.

[186] K. Takegahara, H. Harima. Electronic band structures in $LaRu_4P_{12}$ and $LaFe_4P_{12}$ with modulated skutterudite structures *J. of Magn. and Magn. Mat.* 310, (2007) 861-863.

[187] I. Shirotani, private communication.

[188] J. Yang, R. Liu, Z. Chen, L. Xi, J. Yang, W. Zhang and L. Chen. Power factor enhancement in light valence band p-type skutterudites. *Appl. Phys. lett.* 101, (2012) 022101-022104.

[189] J Hayashi, K Akahira, K Matsui, H Ando, Y Sugiuchi, K Takeda, C Sekine, I Shirotani and T Yagi. Bulk moduli of superconducting skutterudites YT_4P_{12} (T = Fe, Ru and Os) *Journal of Physics: Conference Series* 215, (2010) 012142-1012142-4.

List of Publications

Refereed journal papers

1. Swetarekha Ram and V. Kanchana, M. C. Valsakumar. Skutterudites under pressure: An Ab-initio study. *J. Appl. Phys.* 115, (2014) 093903-8.
2. Swetarekha Ram, V. Kanchana. Lattice dynamics and superconducting properties of antiperovskite La_3InZ (Z = N, O). *Solid state communication* 181, (2014) 54-59.
3. Swetarekha Ram, V. Kanchana, A. Svane, S. B. Dugdale, and N. E. Christensen. Fermi surface properties of AB_3 (A = Y, La; B = Pb, In, Tl) intermetallic compounds under pressure. *J. Phys.: Condens. Matter* 25, (2013) 155501-155509.
4. Ganesh Adhikary, Deepnarayan Biswas, Nishaina Sahadev, Swetarekha Ram, V. Kanchana, C. S. Yadav, P. L. Paulose, and Kalobaran Maiti. Importance of ligands in the electronic properties of $FeTe_{0.6}Se_{0.4}$. *J. Appl. Phys.* 114, (2013) 163906-5.
5. Swetarekha Ram, V. Kanchana, G. Vaitheeswaran, A. Svane, S. B. Dugdale, and N. E. Christensen. Electronic topological transition in $LaSn_3$ under pressure. *Phys. Rev. B* 85, (2012) 174531-174538.
6. V. Kanchana, Swetarekha Ram. Electronic structure and mechanical properties of Sc_3AC (A = Al, Ga, In, Tl) and Sc_3BN (B = Al, In): Ab-initio study. *Intermetallics* 23, (2012) 39-48.
7. Swetarekha Ram , Mudavath Rahul Chauhan , Kunal Agarwal and V. Kanchana. Ab-initio study of Heusler alloys Co_2XY (X = Cr, Mn, Fe; Y = Al, Ga) under high pressure. *Phil. Mag. Lett.* 91, (2011) 545-553.

Conference papers

1. Swetarekha Ram and V. Kanchana. Fermi Surface Studies Of Co-based Heusler Alloys: Ab-initio Study. AIP Conf. Proc. 1512 (2013) 1102.

Curriculum vitae

Name: *Swetarekha Ram*

Educational Qualifications

Year 2010-2014 : Doctor of Philosophy (Ph. D.) in Physics, (continuing).
Institution : Indian Institute of Technology Hyderabad,
Andhra Pradesh, India.
Dissertation Topic : Fermi surface properties of binary and ternary superconductors.
Supervisor : Dr. V. Kanchana.

Year 2007-2009 : Master of Science (M. Sc.), Physics.
Institution : North Orissa University, Baripada, Orissa, India.
Specialization : Solid state Physics.

Year 2004-2007 : Bachelor of Science (B. Sc.).
Institution : F. M. Autonomous college, Balasore, Orissa, India.
Subjects : Physics (Honors), Chemistry and Mathematics.

Honors and Awards

Year 2013 : Young scientist award as a winner (1^{st} prize) in physics from Dr. K.V. Rao scientific society, A. P., India.

Year 2012 : Best paper award on National Conference on Materials for Advanced Technologies (NCMAT), Gwalior, M. P., India.

Year 2011 : Awarded for outstanding academic performance at IIT-Hyderabad, Hyderabad. A.P., India.

Year 2009 : Joint Entrance Screening Test (JEST) qualified.

Year 2009 : University Gold medal in M. Sc.

Year 2009 : Akhil chandra Dash Memorial Gold medal in M.Sc.

Attended conferences, workshop and visit to outside

Year 2013 : Electronic structure Approaches to Atoms, Molecules, Clusters and Solids, at Advanced Centre of Research in High Energy Materials (ACRHEM), University of Hyderabad, A. P, India.

Year 2012 : National Conference on Materials for advance Technology (NCMAT-2012) at Gwalior, M.P, India.

Year 2012 : 57th DAE Solid State Physics symposium at IIT Bombay, Mumbai, India.

Year 2012 : International Conference on Material Science and Technology (ICMST), Kottayam, Kerala, India.

Year 2012 : Visit to JAPAN for Japan-East Asia Network of Exchange for Students and Youths (JENESYS) programme.

Year 2010 : Workshop on First principle simulation at Jawaharlal Nehru Centre for Advanced Scientific Research (JNCASR), Bangalore, India.

Personal Details

Mothers Name : Kiran Devi Ram.
Fathers Name : Pramod Kumar Ram.
Date of Birth : 20th September, 1984.
Nationality : Indian.
Sex : Female.
Marital status : Married.
Religion : Hindu.
Nationality : Indian.
Language known : English, Hindi, Odia (Read, Write and Speak).
E-mail : swetarekharam@gmail.com

Reference

Dr. V. Kanchana,
Assistant Professor,
Department of Physics,
Indian Institute of Technology Hyderabad,
Ordnance Factory, Yeddumailaram-502205,
Andhra Pradesh, India.

Tel. No. : +91-040-2301-6019
E-mail : kanchana@iith.ac.in